EMULSION INKS: A NEW CLASS OF MATERIALS FOR 3D PRINTING POROUS

TISSUE ENGINEERED GRAFTS

A Dissertation

by

NICHOLAS ALLEN SEARS

Submitted to the Office of Graduate and Professional Studies of
Texas A&M University
in partial fulfillment of the requirements for the degree of

DOCTOR OF PHILOSOPHY

Chair of Committee,	Elizabeth Cosgriff-Hernández
Committee Members,	Duncan Maitland
	Akhilesh Gaharwar
	Arum Han
Head of Department,	Anthony Guiseppi-Elie

May 2017

Major Subject: Biomedical Engineering

ABSTRACT

Tissue grafts are often crucial in restoring function and promoting healing after traumatic injury. Many synthetic materials have been developed, but these often suffer from inadequate tissue integration, limited biodegradability, and mechanical mismatch with the target tissue. Recent advances in 3D printing technologies have enabled the fabrication of custom-fit scaffolds that resemble native tissue. Although these scaffolds can more closely mimic defect shape, new inks are needed to provide tunable control over multiple levels of scaffold structure and function.

To address these limitations, we have developed an extensible system for printing complex tissue engineered scaffolds by creating emulsion templated inks. These emulsion inks exhibit tunable pore sizes, modulus, and strength. Formulation of inks with viscous, reactive macromers results in extruded material that holds its shape after extrusion and polymerizes rapidly upon exposure to UV light. New methodology was developed to permit the rational design of emulsion inks based on rheological and cure properties, and these inks were able to successfully create high fidelity scaffolds with customizable, hierarchical porosity. Emulsion inks are compatible with nearly any hydrophobic macromer allowing development of inks with limitless chemical and material properties.

Next, a hybrid printing system was developed for extrusion of thermoplastic PCL and PLA along with emulsion inks to provide mechanical reinforcement. Scaffolds without reinforcement exhibited an increase in permeability with a decrease in infill density, with detriment to their modulus and strength. Mechanical reinforcement with

PLA, however, resulted in a significant increase in modulus and strength in all cases. The creation of novel emulsion inks from existing biomaterial systems opens the door to the creation of scaffolds with a wide range of physical and chemical properties.

Finally, this system was extended to oil-in-water emulsions, termed hydrocolloid inks, to facilitate printing of hydrogels. Due to their low viscosity, high fidelity printing of hydrogels has typically been limited to SLA methods. SFF printing of hydrogel scaffolds frequently relies on thickeners and additives, but we have refined the rheological properties without modification of the hydrogel makeup by emulsifying with innocuous mineral oil. These 3D printed hydrogel scaffolds represent some of the highest fidelity reproductions of complex anatomical geometries in the literature to date. Additionally, this system provides a methodology for creating hydrocolloid inks from nearly any hydrogel biomaterial.

In summary, we have developed a library of porous materials that can be used to improve tissue regeneration. Furthermore, the emulsion structure-property relationships explored here can be used in designing future emulsion inks. A combinatorial approach of tuning the ink and fabrication system allows for creation of complex scaffolds with improved biomimicry, allowing for a new generation of hierarchically porous tissue engineered constructs.

DEDICATION

To my wife and family, who indulge my need to turn everything into an experiment.

ACKNOWLEDGEMENTS

While my path to obtain a PhD may seem to some a never-ending process, I could not be more grateful for the learning experience during these last years. I've had an amazing time in Aggieland, longer than most, and much longer than I could have hoped for. I would like to thank my advisor, Dr. Elizabeth Cosgriff-Hernandez, for helping develop my skills as a researcher and engineer, and working with me to reign in my uncharacteristic style of reasoning. I am extremely grateful for all of the time and effort she put forth to help me build my skills scientifically, professionally, and personally. I would also like to thank my committee for their guidance and resources towards completing my studies. Specifically, Dr. Akhilesh Gaharwar for his collaboration in printing hydrogels that initiated my experience in printing biological materials, Dr. Duncan Maitland for his flow perfusion apparatus, and Dr. Arum Han for his expertise with alternative printing technologies.

I learned that research can be both incredibly rewarding and incredibly frustrating at the same time. On the bad days, it helped to be surrounded by an entire laboratory of friends like Mary Beth Browning, Jenny Robinson, Dave Dempsey, Bobby Moglia, Roya Nezarati, Mike Whitely, Alysha Kishan, Allison Post, Stacy Cereceres, Prachi Dhavalikar, Karli Gold, and TJ Falohun. They have always been there to listen about my latest contraption or design, be an extra pair of hands, or act as a sounding board for new ideas.

Graduate school also let me experience the joys of mentorship. I was fortunate enough to work alongside fantastic undergraduate researchers who have all gone on to

bigger and better things. My first mentee, Stacy Cereceres, who is now a graduate student in our lab, taught me to always make light of stressful situations. She, Geraldine Pena-Galea, Dhruv Seshadri, and graduate students Mike Whitely, Prachi Dhavalikar and Karli Gold were incredibly helpful and the only reason I ever finished studies in a reasonable time.

I would like to thank my amazing wife, Candice, with whom I have shared this journey through graduate school. Triumphs, failed experiments, and late nights at the lab; it's been a blessing to share it with my best friend and soul mate. I'm not ashamed to admit we talk science over dinner. All the time. She keeps us balanced, reminding us to live a little to keep our sanity. Finally, I'd like to thank my parents for shaping me into the person I am today. Always encouraging and pushing; they have been the perfect role models I can only hope to emulate.

NOMENCLATURE

ABS	Acrylonitrile Butadiene Styrene
BAPO	2,4,6-Trimethylbenzoyl)-Phosphine Oxide
BDMA	1,4 Butane Diol Dimethacrylate
BMP	Bone Morphogenetic Protein
BPO	Benzoyl Peroxide
CAD	Computer-Aided Design
CT	Computed Tomography
DLP	Digital Light Processing
DUDMA	Diurethane Dimethacrylate
ECM	Extracellular Matrix
EGDMA	Ethylene Glycol Dimethacrylate
FBS	Fetal Bovine Serum
HA	Hydroxyapatite
hMSC	Human Mesenchymal Stem Cells
HIPE	High Internal Phase Emulsion
hMSC	Human Mesenchymal Stem Cell
LAB	Laser-assisted bioprinting
LAP	Lithium Acylphosphinate
LDW	Laser-based Direct Writing
LIFT	Laser-Induced Forward Transfer
MAPLE DW	Matrix-Assisted Pulsed Laser Evaporation Direct Writing

PCL	Poly(ϵ-caprolactone)
PDGF	Platelet Derived Growth Factor
PDMS	Polydimethylsiloxane
PEG	Poly(ethylene glycol)
PFDMA	Propylene Fumarate Dimethacrylate
PFP	Powder-Fusion Printer
PGPR	Polyglycerol Polyricinoleate
PLA	Poly(lactic acid)
PLGA	Poly(lactic-co-glycolic acid)
PMMA	Poly(methyl methacrylate)
PNIPAAm	Poly(N-isopropylacrylamide)
PolyHIPE	Polymerized High Internal Phase Emulsion
PPF	Poly(propylene fumarate)
PPGDMA	Poly(propylene glycol) Dimethacrylate
RGD	Arginine-Glycine-Aspartic Acid
SFF	Solid-Freeform Fabrication
SLA	Stereolithography
SLM	Selective Laser Melting
SLS	Selective Laser Sintering
SMP	Shape Memory Polymer
TMA	4,N,N-Trimethylaniline
VEGF	Vascular Endothelial Growth Factor

TABLE OF CONTENTS

LIST OF FIGURES

LIST OF TABLES

1. INTRODUCTION AND LITERATURE REVIEW*

1.1   Biomaterials, Tissue Engineering, and Scaffold Fabrication

Tissue engineers attempt to harness the body's ability to regenerate damaged tissue by combining cells and bioactive factors in a biomaterial scaffold.(1, 2) This strategy typically involves the combination of cells and bioactive factors with a biomaterial scaffold to form an implantable construct that can replace or restore physiological function.(2-4) Ideally, the scaffold will be resorbed as the neotissue is formed, resulting in a functional tissue replacement after remodeling is complete.(5) Biomaterial scaffolds are chosen to mimic important aspects of the target tissue in order to restore function and provide an environment conducive to cell differentiation and proliferation. There is a continued emphasis on enhancing the function of tissue-engineered constructs through the development of improved fabrication methods.(6-9) Traditional techniques for fabricating tissue engineering scaffolds such as gas foaming, solvent-casting, fiber bonding, phase separation, particulate leaching, and freeze drying provide macroscale scaffold features but often lack the complexity of native tissue.(5) Many tissues, such as the lobules of the

liver or nephrons of the kidney, have complex structural units that coordinate multiple types of specialized cells and are critical for tissue function. Fabrication methods that can produce complex geometries have a distinct advantage in their ability to fit an irregular defect site but are also capable of mimicking tissue complexity through the precise positioning of multiple materials and cell types.(10)

Scaffolds that recreate macroscale properties as well as microscale features necessary for cellular function require sophisticated control over fabrication. Recently, 3D fabrication or rapid-prototyping technologies have become more popular and accessible, allowing for exploration of new fabrication techniques capable of geometric accuracy at the macro and micro scale. Precision at this level opens the door for innumerable approaches for tissue engineering scaffolds. Recently, 3D printing has been used to treat a potentially life-threatening condition in which the trachea is prone to collapse, known as tracheomalacia. Researchers developed a 3D printed tracheal splint made from biodegradable poly(ε-caprolactone) for a 2 month old child that required endotracheal intubation to sustain ventilation. The splint was tested in piglets and subsequently given approval for implantation via an emergency-use exemption. An immediate improvement was seen after surgery, and patency was retained after one year with no complications.(11) In another example, high definition imaging and 3D printing technology known as laser sintering were used to create a functional jawbone replacement for an 83-year-old woman suffering from a lower jaw infection.(12) Rapid manufacturing of the jaw implant allowed for creation of "articulated joints, cavities that foster muscle attachment, and grooves to guide nerve and vein regrowth" as well as reduced surgical preparation and recovery. This

2

control over microarchitecture allows for production of functional tissue engineered scaffolds that recapitulate the natural form and function of the tissue. Additionally, designed vasculature may enable the creation of larger, cellularized constructs by providing the requisite nutrient transport for tissue growth.(13-16) Functional tissue constructs could also be used as a diagnostic tool for cell-based assays for drug testing or other therapies. For example, Organovo's exVive3D™ Liver is a fully functional bioprinted human tissue that has been used to provide toxicity assessment that is supplementing *in vitro* and preclinical animal testing.(17)

There has been a tremendous increase in the publication output in 3D printing research over the past two decades, in part due to the expiration of a number of patents, **Figure 1.1**. A timeline of printing technology from its inception to the current state of the art is provided to give a historical perspective of the development of this field, **Table 1.1**. In this review, we will discuss the current state of the art of 3D biofabrication methods and provide a comparative analysis of the common printing methodologies. The printing methods have been divided into acellular techniques (stereolithography, powder-fusion printing, solid freeform fabrication) and bioprinting of cellularized constructs (inkjet-based, extrusion-based, laser-assisted). A description of each of these techniques is provided with a discussion of the advantages and limitations of each. Finally, a discussion of the current challenges and future directions of the field is provided.
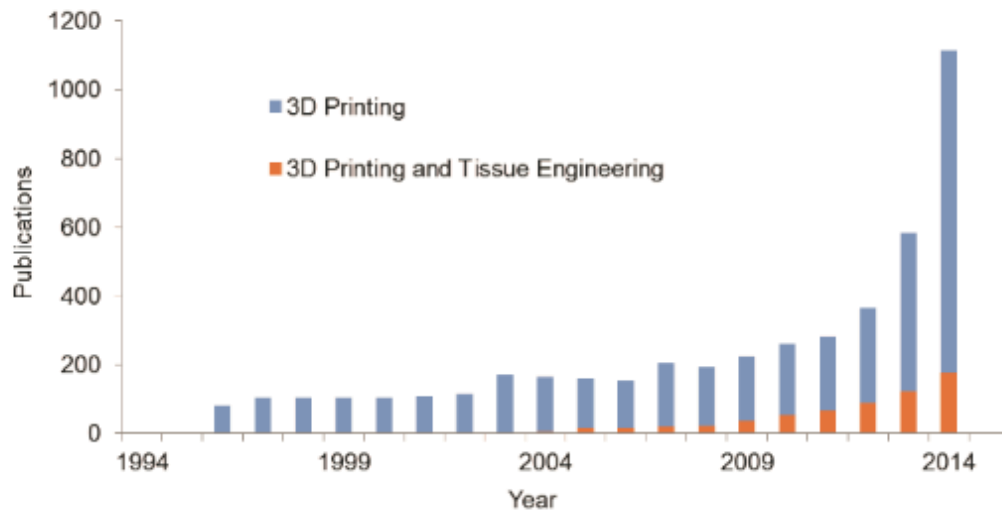
Figure 1.1. Number of publications related to "3D Printing" or "3D Printing" and "Tissue Engineering" according to ISI Web of Science (Data obtained July 2015)

Table 1.1. A timeline for the evolution of 3D printing from its invention to current state of the art in tissue engineering. (18, 19).

Year	Key Developments
1984	Charles Hull invents "Apparatus for making three-dimensional objects by stereolithography" (19)
1986	Carl Deckard invents "Method and apparatus for producing parts by selective sintering" (19)
1989	Scott Crump, co-founder of Stratsys, patents Fused Deposition Modeling (20)
1993	MIT patents "3 Dimensional Printing techniques" and licenses to 6 companies including Z-Corp (21)
1996	Clinical application of biomaterials for tissue regeneration (18)
1999	Luke Massella receives one of the first 3D-printed bladders thanks to the Wake Forest Institute for Regenerative Medicine. It's a combination of 3D printed biomaterials and his own cells (22)
2002	Early stage kidney prototype manufactured using microextrusion bioprinting at Wake Forest Institute for Regenerative Medicine (23)
2005	Dr. Adrian Bowyer (University of Bath) founds RepRap, an open source initiative to build a 3D printer that can print most of its own components (19)
2007	Selective laser sintering machine becomes available, creates 3D printed parts from fused metal/plastic. Opens door to mass customization and on-demand manufacturing of industrial parts
2007	RepRap releases Darwin, the first self-replicating printer, able to print majority of its own components, allowing for self-improvement (19)
2009	Fused deposition modeling patent expires, igniting innovation in the 3D printing industry
2009	MakerBot starts selling DIY kits to make a 3D printer. The first kit to build a printer sells for $750
2010	Organovo, Inc., announced the release of data on the first fully bioprinted blood vessels
2012	Extrusion based (syringe) bioprinting for an artificial liver (23)
2014	Implementation of a multi-arm bioprinter to integrate tissue fabrication with printed vasculature (23)

1.2   Acellular Scaffold Fabrication

Rapid prototyping techniques utilize multi-axis positioning systems and one of many additive methods to generate a 3D construct through sequential layer fabrication.

Depending on the type of technique, the layer can be generated through extrusion deposition, solidification, polymerization, sintering, or binding with many more methods and variants in development. A model is first created in a computer-aided design (CAD) program and then exported into a file format that describes the volume or surface mesh in 3D space such as *.stl, (stereolithography), *.obj, (object), or *.amf (additive manufacturing file). Another program, generally known as a "slicer", is then used to translate the 3D data into slices to be patterned by the printer. The user can configure the algorithm that determines the pattern used to fill the layers and the program calculates necessary parameters such as extrusion speed, cure time, or laser speed to accurately fill the pattern. Early use of these techniques was adapted for mold casting, product development, and functional prototypes. Rapid development of these technologies has increased versatility and precision. Current techniques have the ability to create scaffolds that recapitulate the macroscale geometry of organs, and a print layer thickness as small as 20 μm allows for reproduction of the microarchitectures of bone and other tissues. Techniques with even higher precision are currently being investigated to enable reproduction of smaller tissue features such as hepatic lobules and kidney nephrons. Despite the expanding number of rapid prototyping techniques and variants that have emerged, categories can be used to group these techniques based on the material type and method used to combine each layer. Herein, we will compare and contrast three commonly used techniques: stereolithography (SLA), powder-fusion printing (PFP), and solid freeform fabrication (SFF). A summary of key comparisons of these three methods is provided in **Table 1.2**.

Table 1.2. Comparison of commonly utilized techniques for creating acellular scaffolds.

Attributes	Powder-Fusion Printing (PFP) (24-36)	Solid Freeform Fabrication (SFF) (24-26, 37-42)	Stereolithography (SLA) (24, 25, 43-46)
Layer height	(20-100) μm	(50-500) μm	(25-200) μm
Minimum feature	(125-200) μm	(125-1000) μm	(75-250) μm
Materials	Metals, ceramic powders, thermoplastic polymers	Thermoplastic polymers, ceramic pastes, dense gels	Photopolymers
Solidification Method	Optical, thermal, chemical	Optical, thermal, chemical	Optical
Support Material	Self-supporting	Soluble, detachable	Detachable
Post-processing requirements	Powder cleanup/removal	Support material removal/dissolution	Support material removal/finishing
Machine Cost	$30K-500K	$500-100K	$3K-200K
Print Speed*	5-30 mm/hour (height, Projet)	10-100 mm/s (linear, Makerbot)	10-50 mm/hour (height, Form1)

1.2.1 Stereolithography. Stereolithography (SLA) methods utilize a deflected laser beam or a projected light source to cure and harden exposed areas of photopolymer at the surface of a reservoir of material. Multilayer scaffolds are typically fabricated by lowering a stage and curing successive layers of the construct, **Figure 1.2**. Any photopolymer with a suitable viscosity and ability to harden can theoretically be used to create a construct with SLA. SLA has commonly been utilized to create functional models and positive mold objects. Cooke et al. utilized stereolithography to fabricate 3D scaffolds for bone tissue engineering using biodegradable polymers including diethyl fumarate and poly(propylene fumarate).(47-49) Similarly, a photocurable ceramic acrylate suspension

was used to form a cancellous bone construct,(50) and bone scaffolds with dimensions appropriate for healing critical-sized were created using hydroxyapatite.(51) Stereolithographic techniques are limited in resolution by the diameter of the laser beam to approximately 250 μm, although other methods such as small-spot laser systems and Digital Light Processing (DLP) projection have produced features as small as 70 μm.(52)
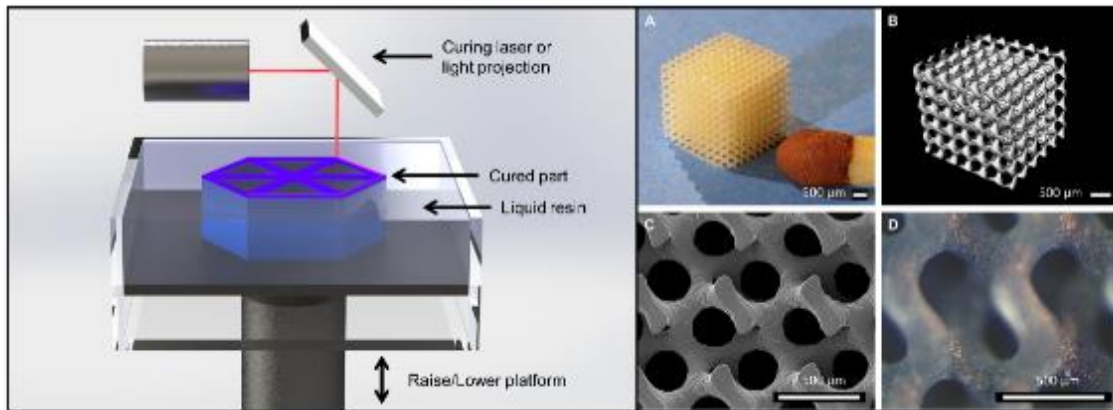
Figure 1.2. (Left) Schematic of stereolithographic printing technique (SLA), and (A-D) exemplary tissue engineering scaffold composed of poly(D-L lactic acid) (PDLLA) that showcases the resolution and detail of SLA. (A) photograph, (B) μCT, (C) SEM, and (D). Scale bar is 500 μm. (Reprinted,(120) Copyright 2009, with permission from Elsevier)

Stereolithography techniques can also be used to create hydrogel scaffolds from natural and synthetic polymers that swell in water and are substantially less rigid than traditional SLA constructs. Hydrogels have become increasing popular as tissue engineering biomaterials due to their high water content and mechanics similar to soft tissue. Yu, et al. created 2-hydroxyethyl methacrylate scaffolds using photolithography to create patterns from non-swollen prepolymer, which were then hydrated and seeded with cells.(53) However, one significant limitation with this technique is that the geometric fidelity of the construct may be compromised by rehydration. Matsuda et al. was able to

8

mitigate the swelling effects by using formulations of vinyl-modified polysaccharides and acrylated-modified polyethylene glycol.(54) Due to the natural biocompatibility of polyethylene glycol solutions, researchers have been able to photopattern scaffolds using hydrogels solutions that incorporate living cells, as discussed in a later section. Stereolithographic techniques have also been used to create molds that are used to cast negative replicas of the printed molds. Orton et al. reported a printed mold of a mandible that was generated using a CAD program and data from computed tomography (CT) imaging. The mold was filled with a hydroxyapatite/acrylate mixture and heated to cure the scaffold, while incinerating the mold. The result was a hydroxyapatite scaffold containing internal channels of designed geometries.(55) The scaffolds were then implanted in minipigs and shown to induce bone ingrowth over a nine-week study.(56) Overall, stererolithography is a versatile technique that is attractive for creating tissue engineering scaffolds because of its precision and the increasing availability of biologically relevant photopolymers. The high resolution of this technique, layers as small as 20 µm, is unmatched by other 3D printing techniques. The high vertical resolution and small feature size capabilities provide exceptional control over the microarchitecture; however, the macromers available typically have limited biocompatibility and constructs are limited to one material without sophisticated apparatuses.(57, 58)

1.2.2 Powder-Fusion Printing. Another set of techniques, generically known as powder-fusion printing, utilizes granular material such as plastic, resin, or metal that are selectively bound together. In selective laser sintering/melting (SLS/SLM) plastic or metal granules are sintered together with a laser beam. The beam is directed across a powder

bed to increase the local temperature and cause particle fusion in the heated area along the directed laser path.(59) Three-dimensional scaffolds are generated by recoating the bed with a new layer of powder and repeating the process through successive layers. A schematic illustrating the mechanics of this process is provided in **Figure 1.3**. After fabrication, unfused powder is removed and the resulting part is a mechanically strong construct with designed geometry and porosity. Similar to SLA, the resolution of SLS printing techniques is dependent on the spot size of the laser or heat source and the size of the powder particles. Typical laser-based systems have minimum features of about 400 μm and minimum void size of about 50 μm.(59) Recently, Shuia, et al. reported that a 30/70 combination of tricalcium phosphate and hydroxyapatite was a promising powder source for the fabrication of SLS bone scaffolds.(60) SLS techniques have also been developed that are able to fabricate constructs with other biopolymers that can be used in a wide variety of medical implants.(61)

Figure 1.3. (Left) Schematic of powder-fusion printing technique (PFP), and (C-D) exemplary tissue engineering scaffolds composed of calcium phosphate–poly(hydroxybutyrate-cohydroxyvalerate) (Ca–P/PHBV) that showcase the resolution and detail of PFP. Models are 250% reproductions of CT scans of a human proximal femoral condyle reconstructed from CT images and then processed into porous scaffold using cubic cells. Scale bar is 10 mm. (Reprinted,(37) Copyright 2010, with permission from The Royal Society)

Scaffolds can also be fabricated in a similar manner from granular material by binding the particles with solvents or adhesives. This is where binder is jetted onto a bed of powder or plaster, fusing the particles of each layer. Scaffolds are built up layer by layer with a minimum layer thickness of approximately the size of the polymer particle size (~50 μm).(31) Scaffolds have also been fabricated which utilize natural biopolymers and polysaccharide such as gelatin, dextran, and starch that are fused together using aqueous solvents. Furthermore, the addition of porogens and particulate leaching have shown promise in creating microporous structures. Simpson at al. developed a porous poly(lactic-co-glycolic) acid (PLGA) scaffold with PFP and demonstrated the ability to precisely reproduce the shape of an entire human fourth middle phalanx. (62) The effects of particulate and pore size have also been explored to examine the effect on cell attachment, growth, and matrix deposition.(63) Although powder-fusion printing is limited to powdered materials, this technique is capable fabricating scaffolds from several materials such as titanium and magnesium that are not readily printable with other techniques. PFP is well suited for bone and other rigid tissues because bound or fused material typically creates constructs of superior mechanical properties. Additionally, some materials naturally found in bone such as tricalcium phosphate are commonly printed using PFP techniques.(64, 65) PFP printing also does not require support material because the unfused powder supports each successive layer and allows for complex shapes including designed, interconnected porosity. However, resolution and minimum pore size is limited by the powder characteristics, and additional sintering is typically required to solidify the

11

part which can lead to cracking and damage. Current research efforts are focused on developing new materials for SLS and refining print parameters to improve surface finish.

1.2.3 Solid Freeform Fabrication. Solid freeform fabrication (SFF) techniques provide a powerful platform for creating tissue engineered scaffolds by utilizing a precise xyz positioning system to direct the position of a nozzle that deposits strands of material. The deposited material solidifies into a predefined shape to build a construct layer-by-layer, **Figure 1.4**. Traditional SFF printers are commonly used for rapid prototyping and characteristically utilize a small diameter polymer feedstock such as acrylonitrile butadiene styrene (ABS) that is forced through a nozzle heated to temperatures over 200°C. Biodegradable polymers relevant to tissue engineering typically melt at lower temperatures and can be printed at more moderate temperatures. For example, Zein et al. used 80 kDa PCL, which has a melting temperature of 60 °C, as feedstock to print microfilamentary lattice scaffolds.(40) Filament was extruded at 125 °C to achieve a sufficiently low melt viscosity, and x-y speed was kept at 6.35 mm/s to allow for sufficient cooling after extrusion before moving to a subsequent layer. While this method produced a precise lattice structure, it required creation of a custom feedstock with precisely controlled temperature and speed parameters to generate filament with the required accuracy.
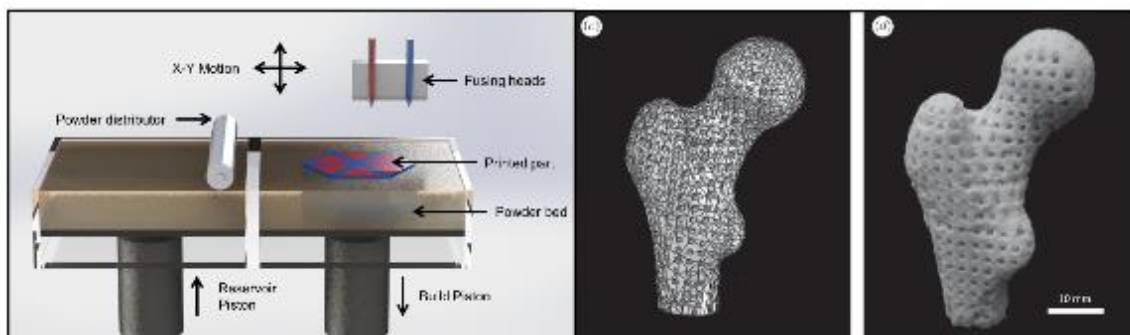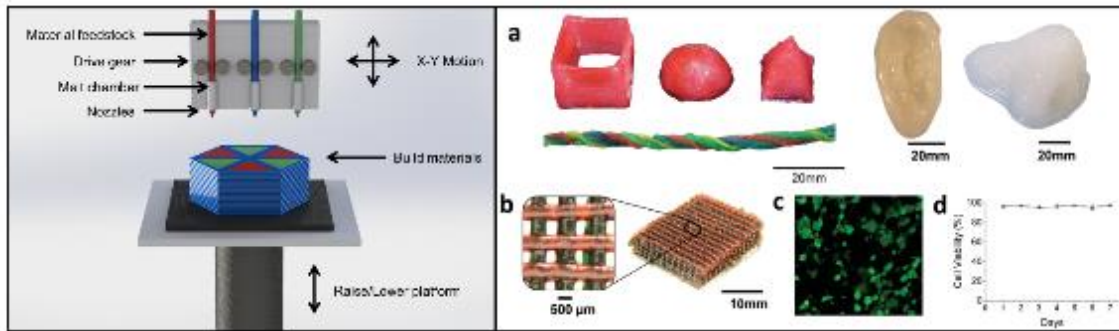
Figure 1.4. (Left) Schematic of SFF printing technique, and (a–d) exemplary tissue engineering scaffold composed of PEGDA, nanosilicates, and alginate that showcases the resolution and detail of SFF. (a) Photograph of various shapes, (b) cross-section and view of the self-supporting lattice, (c) fluorescence microscopy of printed material containing cells, and (d) cell survival after 1 week. PEG-DA, poly(ethylene glycol) diacrylate; SFF, solid freeform fabrication. (Reprinted,40 Copyright 2015, with permission from Wiley.) Color images available online at www.liebertpub.com/teb

In contrast, newer generations of SFF systems employ a heated reservoir to extrude polymer pellets rather than a length of feedstock. Kundu et al. used this method to produce complex biodegradable scaffolds of PCL and alginate.(66) Scaffolds were created by depositing rectilinear patterns of PCL and co-depositing alginate in the spaces created in the PCL pattern. Scaffolds were then implanted in mice and shown to enhance cartilage and collagen formation over a 4 week study. Decreasing nozzle size and layer height increases x-y and z resolution, respectively, but also leads to substantially slower feedstock extrusion rates. Theoretical resolution is limited by the precision of the linear motions system (motors, gears, timing belts, and leadscrews) and the properties of the extruded material that affect shape retention after extrusion. Although SFF techniques are able to achieve a high degree of positional accuracy in the xy-plane, they have a substantial limitation in the ability to print overhanging or unsupported parts because, unlike SLA or

PFP, there is no innate support material from previous layers. Therefore, hardening due to cooling or crosslinking after extrusion is key to provide support for subsequent layers.

Recent improvements in hydrogel rheological properties have also allowed for printing of these materials with SFF. Hong et al. created a printable hydrogel using a semi-interpenetrating network of PEG and alginate with silicate nanoplatelets.(67) These gels had zero-shear viscosity above 10 kPa•s that permitted shape retention after printing and a shear-thinning character that facilitated extrusion.(37) The overall size and accuracy of the printed hydrogel construct is dependent on the volume contained in the syringe and the rheological properties of the hydrogel. Viscosity is known to play a key role in construct fidelity as high viscosity materials provide structural rigidity and support for successive layers as they are extruded.(23, 68) In addition, a secondary crosslinking step is typically used to lock in the printed shape and improve mechanical properties of these gels. For example, Hong et al. soaked the printed construct in calcium chloride solution to crosslink the alginate portion of the gel and prevent swelling and loss of shape. The Lewis group from the Wyss institute have expanded upon these techniques to create scaffolds using sacrificial inks in order to create vasculatures on the order of hundreds of microns in size with the potential to create scaffolds with many materials and cell types.(69, 70)

Extrusion-based printers typically use either pneumatic pressure or a motor actuated plunger to deposit material.(71) Pneumatic systems provide simplified control over the application of force to the extruded material. The system is calibrated for each material with adjustments made to nozzle size, nozzle geometry (tapered tip, cylindrical needle, length), and gas pressure.(72-74) Precise control over the air pressure permits fine

tuning of the material deposition with increased pressures needed for more viscous materials.(75, 76) However, materials with different viscosities will extrude at differing rates when using the same pressure. Therefore, components of multi-material scaffolds need to be printed at differing speeds or using different pressures according to the viscosity of the material. Motor driven extrusion systems utilize a plunger to control the deposition of material, which allows for more sophisticated control over the deposition of material. Unlike pneumatic systems, a motor driven plunger permits variable extrusion speed and retraction to prevent unwanted extrusion as a result of built up pressure. These methods have been capable of printing materials with a wide range of viscosities.(16, 23, 26, 77, 78) Recently, Kesti et al. has shown a combinatorial approach for printing poly(N-isopropylacrylamide) (PNIPAAm) modified hyaluronic acid that involves dispensing hydrogel solution into a warm chamber at 37 °C cause gelation of the PNIPAAm, followed by UV photopolymerization for 10 seconds after each layer to lock in the scaffold geometry.

Overall, SFF is one of the most versatile printing techniques to generate biomimetic scaffolds because of its ability to make multi-material constructs and print soft biomaterials such as hydrated gels. Adaptation of SFF techniques for tissue engineering has led to an increased range of available materials that have the requisite rheological properties to enable both extrusion and shape retention after extrusion. In comparison to the other techniques, SFF scaffolds are somewhat limited in their geometry without the use of a secondary support material. Additionally, due to the filamentous nature of SFF, printed scaffolds may exhibit anisotropic mechanical properties. This may be detrimental

due to potential delamination of the layers, but may be advantageous in creating scaffolds with intended alignment such as ligament or tendon. Although layer height and feature size is typically limited based on nozzle size, improvements in microdeposition resolution is currently being pursued for the recreation of more complex, multimaterial scaffolds.(69)

1.3   Bioprinting of Cellularized Constructs

Bioprinting is generally considered to be the application of additive manufacturing techniques to create cell-based scaffolds. Many of these techniques can be adapted to print with cells as long as the material, deposition method, and processing minimally impact cell viability and function. Biological materials used for printing need to match the native environment of the host environment in order to support the function of those cells. In addition, the cells must be able to overcome the shear stress during the printing process and survive the non-physiological conditions of the printing regime.(73, 77, 79-81) A wide variety of available bioprinting techniques have shown promise in creating complex architectures by using a "bioink" which is printed onto a substrate in a layer-by-layer process to create 3D constructs that mimic native tissue and organs.(68, 82-84)

There are three broad categories of bioprinting, namely microextrusion, laser-assisted, and inkjet-based bioprinting, **Figure 1.5**.(68, 85) In inkjet-based bioprinting, bioink droplets are deposited onto a substrate that gels to form polymeric structures. Microextrusion bioprinting on the other hand uses a mechanical extruder to deposit the bioink as the extruder is moved. Extrusion based bioprinting allows for the use of high cell density with easier processing but occurs at a slower speed compared to drop-based bioprinting.(18, 82) Laser-assisted bioprinting (LAB) has a picoliter (pl) resolution

16

through which cells and liquid materials can be printed. This method of printing is rapidly growing and shows promise to fabricate tissue-like constructs that mimic the physiogical behavior of their host counterpart.(86) Each of these bioprinting methods will be discussed coupled with a focus on their respective print mechanics, applications, and drawbacks. Key attributes of these printing techniques with comparisons of material selection, modes of processing, and cell viability are presented in **Table 1.3**. (18, 23, 68, 85)
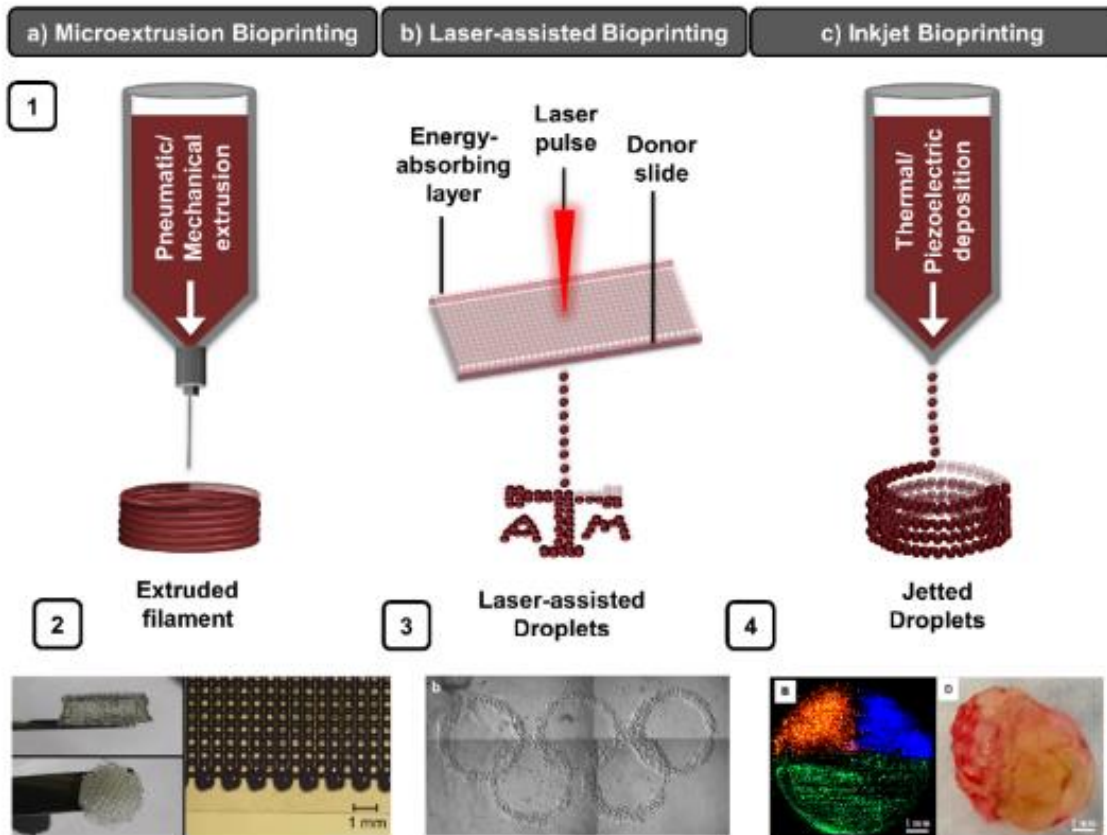
Figure 1.5. (1) Schematics comparison of commonly utilized 3D bioprinting techniques (a) microextrusion bioprinting, (b) laser-assisted bioprinting, and (c) inkjet bioprinting. (2) Exemplary scaffolds composed of 10% w/v gelatin methacrylamide illustrating the resolution and detail of microextrusion bioprinting.(Reprinted,(49) Copyright 2014, with permission from Elsevier). (3) Exemplary patterns consisting of a high density of cells in culture medium illustrating the resolution and detail possible with laser-assisted bioprinting. (Reprinted,(69) Copyright 2010, with permission from Elsevier) (4) Exemplary scaffolds composed of alginate and multiple cell types illustrating the resolution and detail possible with inkjet based bioprinting. (Reprinted,(80) Copyright 2013, with permission from Elsevier)

Table 1.3. Comparison of commonly utilized bioprinting techniques.

Attributes	Laser-Based (16, 18, 23, 68, 69, 79, 80, 86-102)	Inkjet Based (18, 23, 68, 69, 79-82, 84, 86, 87, 98, 103-110)	Extrusion-based (15, 16, 18, 23, 37, 38, 40, 48, 49, 61, 68-70, 98, 104, 111-121)
Resolution	100-600 μm	50 μm wide	5 μm to mm wide
Droplet Size	>20 μm	50-300 μm	100 μm – 1 mm
Materials	Cells in media	Liquids, gels	Liquids, gels, pastes
Fabrication Time	Long	Medium	Short
Cell Viability	95%	85%	40-80%
Processing Modes	Optical	Mechanical, thermal	Mechanical, thermal, chemical
Hydrogel Viscosity	1-300 mPa•s	30 mPa•s - 60 kPa•s	3.5-12 mPa•s
Print Speed	200-1,600 mm/s	1-10k droplets/s	10-50 mm/s
Gelation Methods	Chemical, photo crosslinking	Chemical, photo crosslinking	Chemical, photo, physical crosslinking

1.3.1 Extrusion Bioprinting. Due to the popularity of open source projects such as RepRap and Fab@home, extrusion-based printing methods have become one of the most economical techniques for rapid prototyping. Extrusion bioprinting is a type of SFF that typically involves pressure or screw/plunger actuated dispensing of a fluid containing cells and/or biomaterials. An ideal bioink for extrusion-based bioprinting should be shear thinning to allow for minimal resistance under flow but must also chemically or physically crosslink relatively quickly after extrusion in order support successive layers. Furthermore, possible detrimental effects of polymerization and shear forces on cell viability and function must be considered. The ability of extrusion-based bioprinters to accurately deposit material allows for the fabrication of complex patterned structures,

including the use of multiple cell types.(23) Compared to the other methods discussed, extrusion-based bioprinting is capable of depositing materials with a high concentration of cells in order to accelerate growth and neotissue formation. For instance Yan et al. was able to print gelatin and chitosan hydrogel scaffolds containing hepatocytes utilizing extrusion-based bioprinting.(18) Increasing print resolution and print speed are challenges in extrusion-based bioprinting. Using biocompatible materials that have improved mechanical properties during the printing process will improve cell viability. Furthermore, modification of print mechanics might decrease print times and permit co-extrusion of multiple materials. Although fabrication time is relatively long to achieve high-resolution, complex structures, extrusion-based bioprinting has successfully demonstrated the fabrication of clinically relevant scaffolds for tissue engineering. Similar to other SFF techniques, extrusion bioprinting is ideally suited for biological materials because of its ability to deposit multiple materials with wide-ranging properties. Extrusion bioprinted scaffolds are typically soft, due to their high water content, and deposited material must undergo some form of gelation to support each layer. Therefore, without some kind of mechanical reinforcement, these scaffolds are typically limited to soft tissue applications.

1.3.2 Laser-Assisted Bioprinting (LAB). Laser-assisted bioprinting (LAB), also known as Biological Laser Printing, is a group of techniques that utilize laser energy to facilitate transfer or coordination of scaffold materials. One type of LAB is laser-based direct writing (LDW) uses a laser pulse to locally heat a slide consisting of an energy absorbing layer and solution of cells. Laser patterning of biological scaffolds was first demonstrated by Odde et al. in 1999.(90) The laser pulse causes sublimation or

evaporation of material, expelling the solution of cells on the opposite side and which have been used to deposit fibroblasts, keratinocytes, and hMSCs (91), various cancer cell lines (122), and a range of biopolymers.(123)

Laser-based direct writing is nozzle free thereby permitting the use of high-viscosity bioink unlike that of drop-based bioprinting or extrusion-based bioprinting.(23, 86, 88, 89) Additionally, lasers allow for high precision thus making this method ideal for bioprinting the smallest details of native tissues and organs.(23, 86, 88) Successful application of LDW printing can be traced to the work by Barron et al. where the team printed mammalian cells on a hydrogel.(23, 88, 89) Gaebel et al. utilized LAB printing to pattern human umbilical vein endothelial cells and hMSCs onto a polyester urethane cardiac patch that showed improved cardiac function up to eight weeks after myocardial infarction.(92) Although this technique allows for direct printing of cells, there remain several limitations that should be considered. The heat and damaging forces resulting from the laser pulse can have a detrimental effect on cell survival and long-term behavior.(23, 88, 89) Additional challenges to LAB printing include increased build time, difficulty building scaffold height, and need for new biomaterials that can be cross-linked after deposition.(115, 124) Gudapati et al. reported that cell encapsulation in crosslinked hydrogels was critical for cell survival in laser-based bioprinting techniques.(97, 115, 124) Laser-assisted bioprinting methods offer the most precise positioning of cells and cellular material, but are the most limited in their ability to build constructs vertically. Laser based methods are most applicable in conjunction with other techniques or methods to create 3D scaffolds.

1.3.3 Inkjet Bioprinting. Inkjet bioprinting is a powerful method of precisely depositing cells and biomaterials that leverages sophisticated advances in 2D inkjet printing to create 3D scaffolds. In inkjet bioprinting a fixed volume of fluid is jetted into a precise pattern specified by the software.(23, 107) Inkjet bioprinting has become a popular method in fabricating cell-laden constructs that can mimic the complexity of native tissue or organs. One key advantage of this technique is the speed at which it can construct scaffolds while maintaining a complex 3D architecture.(115, 124) This speed also poses challenges as it severely limits the number of polymeric materials that can be used to bioprint as it requires the gelation time to be greater than or equal to the drop deposition time.(69) Inkjet bioprinters can be adjusted and specifically tailored to allow for printing materials at increasing resolutions and speeds.(18, 23, 68) Inkjet bioprinting utilizes thermal or piezoelectric energy to deposit droplets of solution into a predefined pattern.(18, 23) Inkjet bioprinters typically consist of one or many ink chambers with multiple nozzles corresponding piezoelectric or heating components (125) To eject a droplet of ink, a short pulse of current is applied to actuate the component. In thermal bioprinters, the sudden increase in local temperature causes vapor bubbles to form and collapse, ejecting ink droplets on to the substrate.(125) (18) In piezoelectric inkjet printing, piezocrystals actuate the chamber itself causing an increase in pressure, resulting in droplet ejection.(125) Deposition from the nozzle onto the print bed results when an electric charge induces vibration in the crystals.(18, 125) Heat and mechanical stresses generated during thermal inkjet bioprinting have been shown to adversely affect cell viability.(125) The largest detrimental effect occurs in the nozzle orifice where the

22

temperature there is greatest.(125) There is a need to mitigate and alleviate this issue. Lorber et al. were able to successfully print retinal ganglion and glia cells harvested from the adult central nervous system without causing an adverse effect on cell viability.(109) From this study, researchers were able to show that piezoelectric printing did not compromise the phenotype or activity of these cells.(109) In an effort to increase throughput and accessibility to this technology, Boland et al. reported the printing of thermosensitive gels by using a modified cartridge from a commercially available inkjet printer to create multilayer scaffolds.(82) Additionally, researchers have successfully demonstrated a multihead inkjet-based approach for bioprinting multiple cell lines into heterogenous scaffolds for tissue engineering.(126-128)

A key disadvantage of inkjet printing is that the biological agents need to be in a liquid state to permit deposition. The deposited droplets must then solidify into the required geometry. To address this requirement, commonly used materials are crosslinked using physical, chemical, pH, or ultraviolet methods.(98) However, chemical crosslinking of many natural materials, such as those derived from extracellular matrix (ECM), modifies both the chemical and material properties and the use of some crosslinking mechanisms are known to pose a detriment to cells, thus decreasing cell viability and functionality.(129) While inkjet bioprinting allows for encapsulation of live cells, relatively low concentrations are required in order to form cohesive droplets and prevent clogging of the nozzle.(116, 117) Despite the addressed disadvantages, inkjet-based bioprinters continue to have great potential due to their low cost, high resolution, and high compatibility with many biomaterials. Because commercially available 2D printers

harness this technology, researchers can easily adapt components for research applications. The versatility of inkjet-based technology has refined the capabilities of these printers in order to accurately deposit fine droplets with precise volume to create high resolution scaffolds with cells intact. Droplet size can be modulated from 1-300 picoliters with deposition rates from 1–10,000 droplets per second.(23) Future work will continue to grow this technology to print more biologically relevant materials, and further retain functionality and bioactivity of cells and biomaterials. Multimaterial-printing utilizing inkjet technology is a developing adaptation that needs to be further developed to print multiple cell types in complex constructs. Inkjet bioprinting is capable of creating scaffolds with accuracy within 100 μm, which makes it very useful for creating complex tissue engineered scaffolds. While it is limited in its ability to produce tall structures because of the typical mechanical properties of the gel inks, the ability to print multiple materials and cell types makes it a useful method to create complex tissue with great accuracy.

1.4   Summary, Key Challenges, and Future Directions

The rapid growth in the 3D printing field has opened up new avenues and directions of research. Adaptation of current 3D printing techniques for biological applications has enabled the fabrication of tissue grafts and artificial organs. Although the field is still at a relatively early stage, pioneering research in tissue engineering of organs with 3D printing has shown great promise. Tissue engineering strategies have been used to replace portions of intestine (130), improve repair following myocardial infarction, (131) and even completely replace a bladder, (22, 132) and augmentation of scaffold

fabrication with 3D printing technologies stands to make enormous improvements in the sophistication of these strategies. In addition to tissue engineering, 3D printing has also been utilized in the field of drug delivery,(133) analysis of chemical and biological agents,(134) and organ-on-a-chip devices.(135) As highlighted in this review, the 3D printing process is continuing to evolve with different process mechanics that are being optimized to achieve specific outcomes in regenerative medicine.

Despite the strong potential of 3D printing to improve regenerative strategies, there remain many challenges that relate to both the printing process and the materials available for printing. Processing challenges include the need for improved resolution, increased speed,(23, 72, 136), and printing processes that are compatible with cells.(74, 106, 136) Current efforts to improve printing resolution of lithographic techniques include the development of methods such as electron beam lithography and multiphoton absorption polymerization.(137-140) These methods are capable of creating extremely precise scaffolds with feature sizes on the order of tens of nanometers. As we depart from the modification of current technology and begin designing 3D printers to fabricate custom biomaterials and tissues, an expanding library of biomaterials compatible with the printing process is needed. Materials used for 3D bioprinting must adhere to three key criteria: scaffold materials must 1) be biocompatible, 2) support cell growth and differentiation, and 3) sufficiently retain its shape in order to preserve scaffold integrity until solidification locks in the scaffold geometry.(16, 18, 25, 64, 80, 83) As a result, currently published work use a limited range of materials such as collagen, gelatin, hyaluronic acid, alginate, modified copolymers, and photopolymerizable macromers. Additionally, the design of

25

complex scaffolds that mimic tissue is driven by our understanding of the composition and cellular distribution of those tissues. Therefore, additional fundamental research is needed to be able to accurately image and map complex tissues in order to reproduce scaffolds with the requisite structure and biological cues.

Although there are many challenges specific to printing of materials with cells, development of printable biomaterials remains one of the most important and predominant areas of research. Many biomaterials are inherently printable because of their design or modification for creating tissue engineered scaffolds. Hydrogel biomaterials are typically used with SLA due to their low viscosity, but current research focuses on improving rheological properties to allow for larger and higher fidelity scaffolds with SFF techniques. Other biomaterial systems such as high internal phase emulsions (HIPEs) have been adapted for use with SLA, but because of their tunable rheology, can be modified for use with SFF methods. Current research areas ranges from rheology and porosity to chemistry and mechanical properties. With the wide range of adjustable parameters, emulsions provide a highly tunable system to achieve a wide range of physical and chemical properties.

2. EMULSION INKS FOR 3D PRINTING OF RIGID SCAFFOLDS*

2.1 Introduction

Photocurable emulsion inks for use with solid freeform fabrication (SFF) to generate constructs with hierarchical porosity are presented. A high internal phase emulsion (HIPE) templating technique was utilized to prepare water-in-oil emulsions from a hydrophobic photopolymer, surfactant, and water. These HIPEs displayed strong shear thinning behavior that permitted layer-by-layer deposition into complex shapes and adequately high viscosity at low shear for shape retention after extrusion. Each layer was actively polymerized with an ultraviolet Cure-on-Dispense (CoD) technique and compositions with sufficient viscosity were able to produce tall, complex scaffolds with an internal lattice structure and microscale porosity. Evaluation of the rheological and cure properties indicated that the viscosity and cure rate both played an important role in print fidelity. These 3D printed polyHIPE constructs benefit from the tunable pore structure of emulsion templated material and the designed architecture of 3D printing. As such, these emulsion inks can be used to create ultra-high porosity constructs with complex geometries and internal lattice structures not possible with traditional manufacturing techniques.

_____

Emulsion templating has emerged as a popular technique for the creation of porous polymers because it offers excellent control over pore size and interconnectivity.(141) In this method, a reactive macromer is emulsified with an immiscible liquid and the internal volume fraction increased above 74% to generate a high internal phase emulsion (HIPE). Polymerization of the continuous macromer phase to lock in the emulsion geometry results in a porous material, termed a polyHIPE, with high surface area and permeability.(142, 143) Porous monoliths,(144-146) microspheres,(147, 148) and films(149, 150) have been fabricated using this technique and investigated for diverse applications from nucleophilic catalyst supports(151, 152) to drug delivery vehicles(148) and injectable bone grafts.(48, 153)

Although polyHIPEs are highly tunable, porous materials, a mold or sacrificial material is needed to impart secondary structure to the flowable emulsion precursor. Additionally, creation of polyHIPEs with interconnected porosity becomes difficult with pore sizes greater than 50 μm.(144, 154) Many strategies have been employed to alter the pore architecture, such as the addition of porogens (145, 155) or alternate emulsion stabilizers;(144) however, these methods typically lead to closed pore structures or decreased mechanical properties. In contrast, recent advances in additive manufacturing methods have demonstrated the ability to optimize mechanical function as well as mass transport through designed, porous architectures.(156, 157) To this end, researchers have recently explored methods based on stereolithographic apparatus (SLA) to fabricate constructs with precise architectures from emulsion-templated materials.(154, 158, 159)

The combination of the highly porous polyHIPE material and an additive manufacturing design process would enable a vast array of complex geometries and hierarchical porosity.

The rheological properties of HIPEs can be tuned to permit the low viscosity necessary for fabrication with SLA.(143, 153, 160) However, the shear-thinning nature of HIPEs and ability to achieve high viscosity pastes that do not slump or spread also enables the use of extrusion methods such as solid freeform fabrications (SFF). SFF may provide a more adaptable system that is uniquely poised to reduce material cost and volume requirements. SLA requires a relatively large reservoir volume, as tall as the printed construct, whereas SFF only requires the volume of the printed construct with very little waste material. In addition, the ability for SLA to create multimaterial constructs is extremely limited,(58) which restricts future development of more complex constructs.

Here we describe a new SFF technology capable of printing curable emulsion inks to form porous polyHIPE foams with hierarchical porosity. Briefly, HIPE material is deposited layer-by-layer using an open source 3D printer equipped with a syringe and motor-actuated plunger. Emulsions inks are rapidly cured after deposition by constant UV irradiation to form high porosity constructs in a method we term Cure-on-Dispense (CoD) printing, **Figure 2.1**. These 3D printed polyHIPE constructs benefit from the tunable pore structure of emulsion templated materials and the fine control over complex geometries of 3D printing that is not possible with traditional manufacturing techniques.(141, 161)
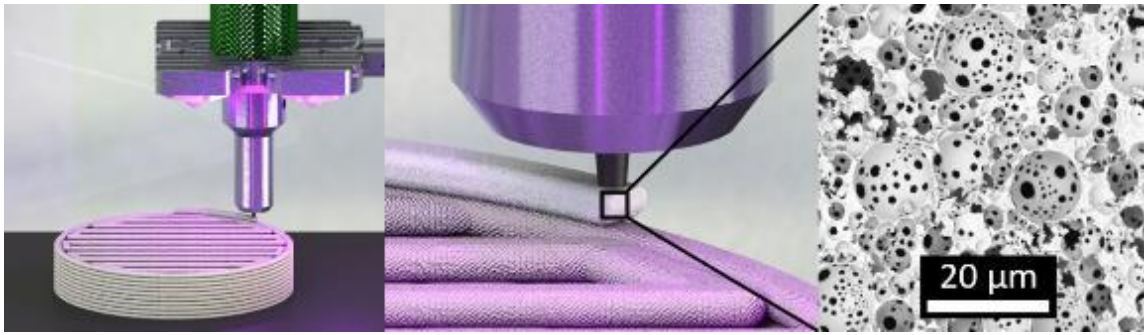
Figure 2.1. Schematic of emulsion ink printing setup with UV Cure-on-Dispense (CoD).

3D printing of viscous materials has recently been investigated for a variety of applications.(37, 67, 125, 162) These studies have identified key characteristics for successful construct fabrication, including shear-thinning behavior to permit extrusion at typical printing shear rates, a sufficiently high shear elastic modulus and shear yield strength to prevent slump after exiting the nozzle, and a rapid post-extrusion solidification method. To develop a printable emulsion ink, the effects of HIPE viscosity and cure rate on print fidelity were investigated. Three series of HIPEs were formulated containing a low viscosity component, poly(propylene glycol) dimethacrylate (PPGDMA), and 0, 20, or 40 mol% of a high viscosity component, diurethane dimethacrylate (DUDMA). Given that these macromers have similar molecular weights and functionality, the increased viscosity of the DUDMA was attributed to the hydrogen bonding of urethane groups. UV intensity was modulated to alter the cure rate during print without impact on other compositional variables. Line slump was quantified using scanning electron microscopy and correlated to print fidelity. The versatility of the printable emulsion inks was then demonstrated with a range of printed construct geometries.

2.2   Materials and Methods

2.2.1 Emulsion Inks. Polyglycerol polyricinoleate (PGPR 4125) was donated by Paalsgard. Poly(propylene glycol) dimethacrylate (PPG-DMA, MW = 560 Da, CAS-No 25852-49-7), diurethane dimethacrylate (DUDMA, MW = 471 Da, CAS-No 72869-86-4), phenylbis (2,4,6-trimethylbenzoyl)-phosphine oxide (BAPO). All chemicals were purchased from Sigma Aldrich and were used as received. HIPEs were prepared using the FlackTek Speedmixer DAC 150 FVZ-K.

Briefly, DUDMA, PPG-DMA, BAPO photoinitiator, and PGPR surfactant (10% of the macromer phase) were mixed in the speedmixer cup at 2500 rpm for 2.5 minutes. Once thoroughly mixed, an aqueous solution of deionized water and calcium chloride (5% w/w) was added in stages for a total internal volume fraction of 75%. The emulsion was mixed after each addition at 2500 rpm for 2.5 minutes. Calcium chloride was used to prevent Ostwald ripening and improve homogeneity. Successful HIPEs were typically characterized by an opaque white appearance with an increase in viscosity, similar to mayonnaise or Elmer's Glue®.

2.2.2 Ink Rheology. The rheological properties of HIPE formulations were measured using a controlled stress rheometer (Anton Paar Physica MCR 301) fitted with parallel plate geometry (Anton Paar Measuring Cone CP50-1/Q1, 50 mm diameter). A small volume (2.5 mL) of each HIPE formulation was poured into the specimen holder at 25°C and allowed to acclimate for 60 seconds. Oscillatory-shear measurements were carried out at 1 Hz with a stress amplitude range of 0.1 to 1000 Pa. Viscometry measurements were performed at a shear rate of 0.01 to 100 s^{-1}.

31

2.2.3 3D Printing. 3D-printed polyHIPE constructs were fabricated utilizing SFF. Emulsions were loaded into a custom RepRap-style 3D printer equipped with an EMO-25 emulsifiable extruder (HYREL 3D) and a 22 gauge (413 μm) blunted stainless steel needle (Sigma Aldrich). To provide accurate results for single and dual layer prints, placing the nozzle at a consistent distance from the build platform was achieved by enabling automatic bed leveling in the printer's firmware. Using the nozzle and build plate as a circuit, electrical continuity was used as a measure of contact. Using this method, the height of the surface of the build plate was determined at a precision of ~ 2 μm. Gcode was created with slic3r version 1.2.9 by slicing a cylinder with a diameter of 20 mm and height of 0.2 mm, 0.4 mm, 2 mm, or 4 mm to create one layer, two layer, small, and large constructs, respectively. The following settings were used for printing: printing speeds of 10 mm/s, nonprinting speeds of 25 mm/s, layer thickness of 200 μm, infill of 50 or 70% (rectilinear grid), extrusion width of 0.6 mm, one perimeter, and no top or bottom solid layers. Constructs were subjected to UV light while each layer was printing, and for 10 seconds following each print. Due to their geometric similarity, each layer was subjected to UV for approximately the same length of time, approximately 90 seconds, and the final layer was given additional time to cure since it had no following layers. No other post-print curing was necessary. The UV source consisted of four UV LEDs (365 nm, 700 mW radiant flux) positioned at a 5 cm vertical distance and 2 cm radial distance from the printing nozzle. Radiant flux was measured using a radiometer (Solar Light, PMA2200) equipped with a UV-A detector (PMA2110) positioned at the tip of the nozzle. A maximum value of 100 mW/cm^2 was measured at 100% output and proportional values

were achieved with pulse width modulation of the output. A UV shield, 20 mm in diameter was positioned 1.5 mm from the nozzle tip in order to prevent HIPE from curing on or within the nozzle. A schematic of this printing setup is included in supplemental information.

2.2.4 Characterization. All specimens were cured under using the 365 nm UV cure-on dispense source and dried under vacuum for 24 hours to remove water. Gel fraction was obtained by soaking printed constructs in dichloromethane for 24 hours, followed by vacuum drying to obtain the final weight. It was assumed that surfactant was removed by this process and the weight of the surfactant was subtracted from the initial weight for gel fraction calculations. Samples were qualitatively examined by optical microscopy. A printable ink possessed clean breaks in filaments without tailing during stops/starts, channel size scalability with applied pressure, and shape retention throughout the entire process. An acceptable construct supported the filaments without introducing filament breakup due to viscous drag induced by nozzle translation during the printing process. The effect of infill (50% vs 70%) and print layers (5 vs 20) on print fidelity was evaluated for each composition.

2.2.5 SEM Analysis. The effect of composition and cure rate on line slump of dual layer prints was evaluated using SEM (JOEL 6500) equipped with a rotating/tilting stage. The construct was first cut with a razor blade vertically, perpendicular to the lines, to reveal the cross sections of interest. Specimens were then coated with gold, imaged, and the line width and height measured using ImageJ. A minimum of 3 lines were analyzed per print for 3 separate prints (n = 9).

2.3   Results and Discussion

2.3.1 Rheological Characterization. The rheological behavior of the emulsion inks is shown in **Figure 2.2**. All inks exhibited shear thinning behavior with sufficiently low viscosity at typical printing shear rates (<10 Pa•s at a shear rate of 50 s^{-1}) to permit extrusion. Increasing DUDMA content resulted in an increase in low-shear viscosity (at 0.01 s^{-1}) with values of 770 ± 40, 1310 ± 210, and 3320 ± 430 Pa•s for HIPEs with 0, 20, and 40% DUDMA, respectively (Figure 2a). The shear storage moduli (G') of the emulsion inks are higher than the shear loss modulus (G"), which highlights the viscoelastic character of the inks and ability to maintain their printed filamentary shape. In particular, the plateau value for G' of the formulation with 40% DUDMA exceeded G" by an order of magnitude at low stress. This suggests that an increase in DUDMA content should increase shape retention after extrusion while maintaining the ability to be extruded under modest applied pressures due to its strong shear-thinning behavior. At the crossover point between the two moduli curves, the shear yield stress (τ_y) was 9.3 ± 0.9, 33.3 ± 1.1, and 53.4 ± 1.2 Pa for HIPEs with 0, 20, and 40% DUDMA, respectively (Figure 2b). Although the addition of the viscous DUDMA component enhances the yield stress, these values are likely insufficient to support subsequent layers and build construct height.
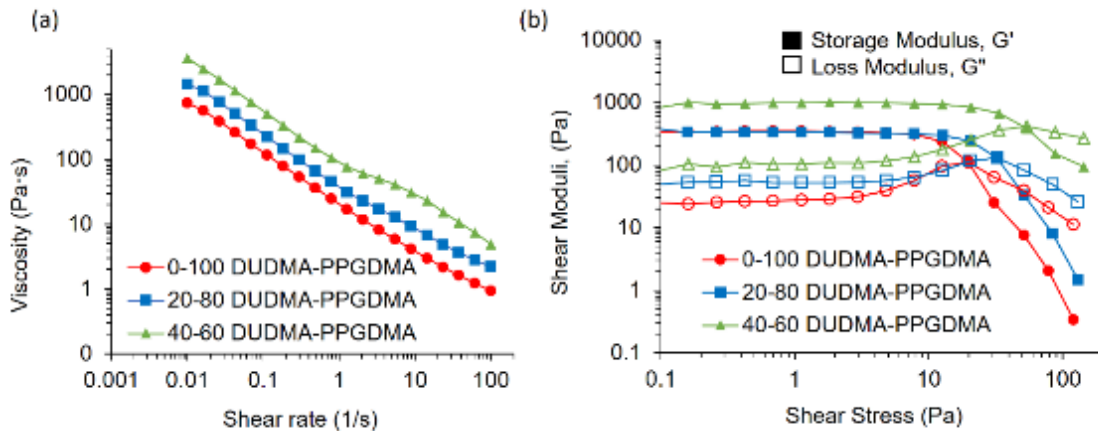
Figure 2.2. Log-log plots of (a) viscosity as a function of shear rate and (b) shear storage and loss moduli as a function of shear stress for HIPEs of varying composition.

2.3.2 Effect of Cure Rate. In order to achieve emulsion inks with sufficient strength to build large, multilayer constructs, cure-on-dispense (CoD) technology was utilized to initiate radical crosslinking of the ink upon extrusion and harden the extruded filament prior to the addition of subsequent layers. To elucidate the effect of rapid polymerization and ink rheological properties, simple constructs with one or two layers were printed, sectioned, and examined under scanning electron microscopy. Viewing the filament cross-sections at a 45° angle permitted quantification of line spreading and any corollary reduction in line height. To this end, simple constructs were printed with a layer height of 0.2mm, an extrusion width of 0.6 mm and a photoinitiator concentration of 1% while varying both the UV intensity and DUDMA content. The "slicing" software, which converts the model into instructions for the printer, calculates extrusion volume needed fill the length of a given line with the theoretical cross-sectional geometry. This geometry is defined as a rectangular prism with two semicircular ends, with height equal to the layer

thickness, and width (including the semicircular ends) equal to the extrusion width. As expected, an increase in UV intensity and DUDMA content displayed a decrease in line width and increase in line height, **Figure 2.3**. Measurements of line width and height were expressed as the mean ± standard deviation. Single factor ANOVA with Tukey's post hoc test was applied to determine statistical significance. All compositions with 40% DUDMA were found to have significantly decreased line width relative to all compositions with 0% DUDMA, Figure 3b. This was attributed to the increased low-shear viscosity and increased yield stress of this ink composition; however, these materials did not demonstrate bridging in dual layer prints (supplemental information). Compositions with 40% DUDMA that were subjected to 100 mW/cm^2 were found to have significantly increased height (p=0.005) relative to all compositions without UV curing, which highlights the utility of CoD to enhance shape retention of the filament after extrusion. The combination of increased low-shear viscosity and rapid hardening with CoD resulted in observed line bridging in multi-line constructs, Figure 3c. Line bridging is critical for print fidelity due to the loss of height and subsequent print failure that occurs with filament layer fusion.
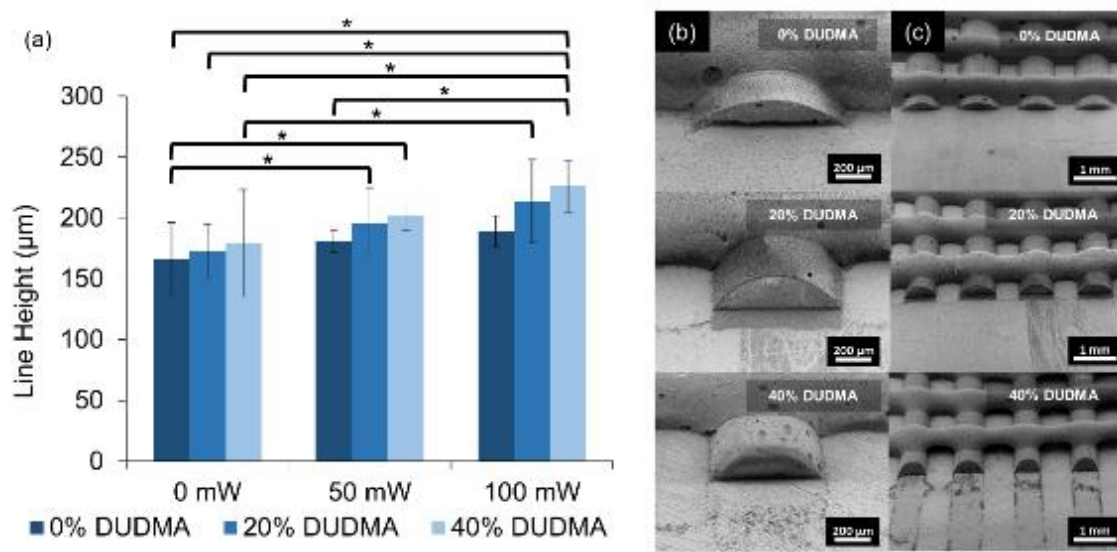
Figure 2.3. Measured cross sectional heights (a) of the first deposited layer for different PolyHIPE compositions and UV intensities. Example cross sections for each composition (b) and resulting dual layer constructs (c) show the effect of increased DUDMA on line spreading, height reduction, and ability to span gaps between extruded strands for prints subjected to 100 mW/cm2. Statistical significance (*) was accepted for p<0.005. Prints with 0 mW were subjected to no UV during printing, followed by 10 mW of UV for 10 seconds after completion of each layer.

2.3.3 Combined Effect on Print Fidelity. In order to correlate the observed filament behavior with construct print fidelity, cylinders with a diameter of 20 mm and varied height were printed with each composition using 1% photoinitiator and a UV intensity of 100 mW/cm^2, **Figure 2.4**. The effect of HIPE composition and rheology on print fidelity was then evaluated. First, successful prints were identified that could build height without failure caused by disruption of the deposited lines. Print fidelity was then determined by dimensional analysis as compared to the programmed dimensions. Constructs with a height within a single layer thickness, 0.2mm, and diameter within a single extrusion width, 0.6 mm, were considered high fidelity. The low-shear viscosity of the emulsion inks had the greatest impact on print fidelity. As expected, HIPEs with 0%

DUDMA were unable to build height, failing after 1 mm. HIPEs with 20% DUDMA were able to build height but failed to print 4 mm constructs without defects. All of the prints with the HIPEs with 40% DUDMA displayed good dimensional fidelity with few blobs, smears, or unwanted spreading. At lower viscosity, print failure was attributed to the increased line spreading observed in the previous study. With decreased line height, the distance between the nozzle and printing layer becomes too large to accurately deposit extruded material and forms a droplet on the nozzle tip. This droplet is either deposited on the construct as a defect or polymerizes to the tip of the nozzle. This can result in a brushing effect prior to full cure that results in the line fusion seen in 4 mm constructs with 0% and 20% DUDMA, eventually failing due to a cumulative reduction in line height. Infill density, the volume of filled internal space within the perimeter lines, was modulated to evaluate the effect of increased mechanical reinforcement on construct fidelity. It was found that increasing infill from 50 to 70% markedly increased print quality in most cases. Although no acute failures or gaps were noted for HIPEs with 40% DUDMA, increased infill density resulted in a cleaner print with fewer defects. The higher infill density enabled HIPEs with 20% DUDMA to successfully print shorter constructs and delayed failure of taller constructs until after layer 15. The increased fidelity at higher infill was attributed to the increased density of support strands for the subsequent filament deposition that minimized line slump between support strands (supplemental information). Gel fraction of printed constructs was in the range of 90-95% after accounting for surfactant content, indicating high conversion.
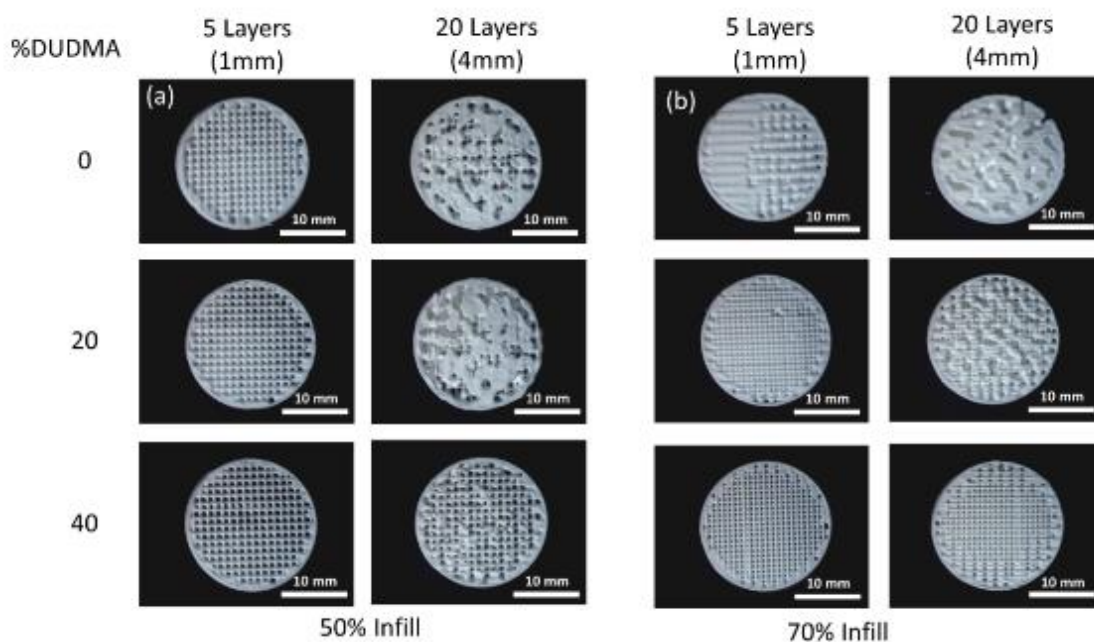
Figure 2.4. Optical images of 5 and 20 layer constructs (1 mm and 4 mm, respectively). One set was done with 50% infill (a) and one with 70% infill (b) to show the effect of filament density on print fidelity.

2.3.4 Evaluation of Large Printed Constructs. Finally, several geometries were selected to demonstrate the ability to print large, complex constructs with these emulsion inks using CoD. A skull defect, approximately 40 mm x 60 mm x 2 mm, was modeled in Solidworks based on CT data, **Figure 2.5.** The model was then printed using the 40% DUDMA composition, resulting in a construct with high dimensional fidelity. Other complex geometric shapes were printed to evaluate the ability to create vertical and horizontal holes, as well as solid and sloping faces.
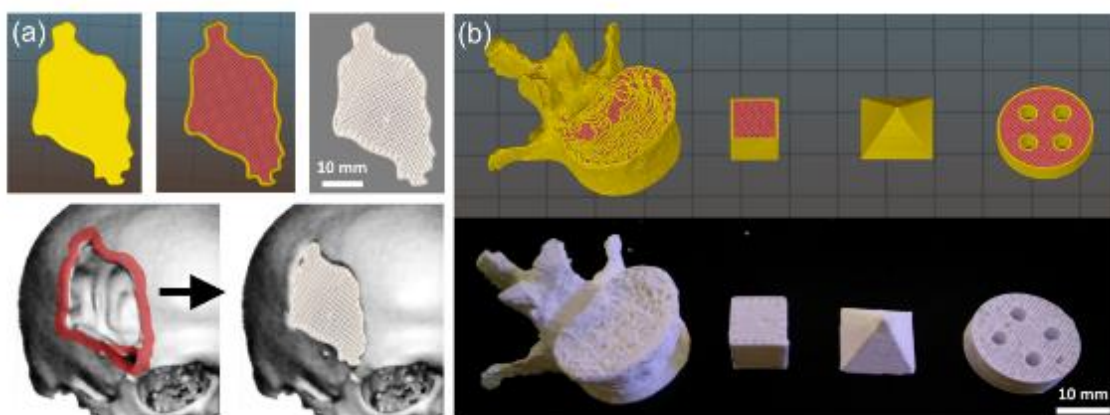
Figure 2.5. Full construct prints of emulsion inks that demonstrate versatility of cure-on-dispense technology. (a) CT data used to determine precise geometry of skull defect, gcode representation of the print, and resulting printed construct. (b) Example models and prints with custom geometry that could be used to make constructs with complex geometry.

2.4   Conclusions

In summary, we have developed a system for tuning and optimizing rheological and cure properties for 3D printing with SFF. We utilized this system to adapt emulsion templated materials into emulsion inks, and have successfully fabricated scaffolds with hierarchical porosity. Emulsion inks are compatible with nearly any hydrophobic macromer allowing development of inks with limitless chemical and material properties. Modulation of rheological properties resulted in inks with increased viscosity at low shear rates, necessary for shape retention after extrusion, while retaining necessary shear-thinning characteristics. The addition of cure-on-dispense to the SFF setup enables the printing of a broader range of inks that rapidly cure after extrusion to support subsequent layers and printing of large constructs.

Formation of the emulsion with water as the droplet phase allows for printing interconnected, porous materials with little or no need for porogen removal. As such, they can be used to create ultra-high porosity constructs with complex geometries and internal structure that is not possible with traditional manufacturing techniques. While these materials have proven mechanically strong enough for handling, processing parameters like infill density, infill geometry, and perimeter thickness have a direct impact on scaffold properties. In order to overcome these limitations, it may be necessary to hybridize this method with other SFF methods like thermoplastic extrusion to print multimaterial scaffolds with synergistic properties. For example, a porous material from the emulsion inks can be printed in parallel with a thermoplastic polymer such as PLA of PCL to generate composites with increased strength and permeability.

3. MULTIMATERIAL PRINTING EMULSION INKS TO ENHANCE BIOMIMICRY

3.1   Introduction

3D printing technologies has led to an expanding number of printable biomaterials and tissue engineered scaffold designs (18, 64, 163-165). Various methods for printing biomaterials have been adapted from existing methodologies such as stereolithography (166), powder-fusion (167), and extrusion deposition (168). Each of these methods provides advantages and limitations in terms of resolution, speed, accuracy, and material selection. For example, stereolithographic methods provide exceptional resolution but are typically limited in biomaterial selection to a relatively few number of low viscosity, photocurable resins. Extrusion-based methods offer more modest resolution but are capable of printing a broader range of materials including hydrogels (98), ceramics (34), and, more recently, curable emulsion inks (169). In addition, it is more readily adapted to printing multi-material constructs with the potential to more closely mimic native tissue complexity(170).

Curable emulsions such as those based on high internal phase emulsions (HIPEs) are good candidates for bioinks because of their high porosity and tunable rheology. HIPEs exhibit low viscosity at typical printing shear rates, allowing for extrusion, and high viscosity at low shear, allowing them to retain their shape after extrusion until cured. We recently demonstrated the feasibility of using emulsion inks based on HIPEs to print complex anatomical models (169). The resulting constructs were rigid foams with

interconnected porosity that are well suited for use as bone graft; however, this study utilized hydrophobic, photopolymerizable macromers that were non-degradable and not established as biocompatible. The objective of this study was to identify an emulsion ink with the requisite properties for use as a biomaterial scaffold for bone regeneration. Fumarate-based biomaterials have demonstrated strong promise as bone grafting biomaterials and have a demonstrated *in vivo* degradation profile, biocompatibility, and osteoconductivity (171-173). Propylene fumarate dimethacrylate (PFDMA) is a low viscosity, hydrophobic macromer that has the requisite properties for HIPE formation. Studies investigating PFDMA polyHIPE as an injectable bone graft reported that the resulting scaffold was biodegradable, cytocompatibility, and displayed excellent compressive properties (48, 174, 175). Based on this established potential as a bone graft material, we investigated PFDMA HIPEs as an emulsion ink for 3D printing bone grafts and characterized the print fidelity, permeability, mechanical properties, and cytocompatibility of the resulting scaffolds.

It remains challenging to achieve the compressive mechanical properties of bone while maintaining the requisite porosity that supports both cellular infiltration and the necessary permeability to support nutrient and waste transport for cell survival. In contrast to current bone grafts with homogenous structures, native bone anatomy is more complex with dense cortical bone surrounding the more porous trabecular bone and vascular supply provided through Volkmann and haversian canals. In order to mimic this structure, a HYREL printer was adapted to achieve multi-modal printing combining emulsion ink paste extrusion with Cure-on-Dispense (CoD) and high temperature thermoplastic

43

extrusion. Herein, we present an open source method for printing multi-material bone grafts based on PFDMA polyHIPEs with hierarchical porosity and reinforced with a dense shell of poly(ϵ-caprolactone) (PCL) or poly(lactic acid) (PLA), **Figure 1.** The print fidelity of dual material deposition was evaluated and the effect of the polyester shell on compressive mechanical properties was characterized. Overall, these studies were used to determine the potential advantages of combining emulsion inks with traditional thermoplastic extrusion printing to generate biomimetic bone grafts with enhanced mechanical properties and increased permeability to support cell viability.
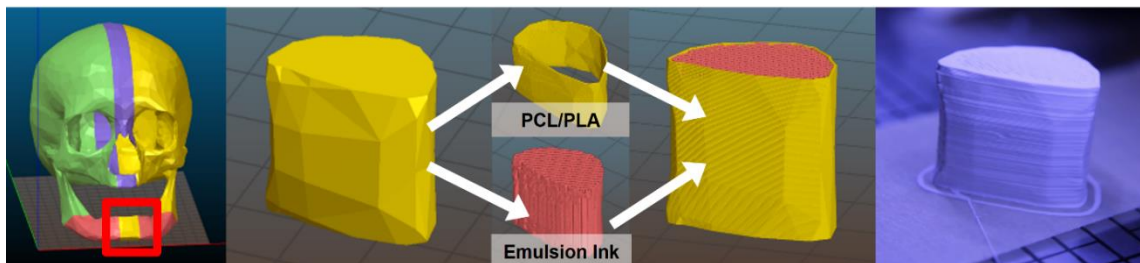
Figure 3.1. Example workflow for developing a custom biomimetic bone grafts from a jaw segment (thingiverse thing:887), developed g-code, and resulting constructs printed with emulsion ink and thermoplastic extrusion.

3.2   Materials and Methods

3.2.1 Emulsion Inks. Polyglycerol polyricinoleate surfactant (PGPR 4125) was donated by Paalsgard (Juelsminde, DK). Calcium chloride and phenylbis (2,4,6-trimethylbenzoyl)-phosphine oxide (BAPO) were purchased from Sigma-Aldrich and used as received. PFMDA was synthesized in a two-step process and purified as detailed previously(175). Briefly, the diester, bis (1,2 hydroxypropyl) fumarate, was synthesized by adding propylene oxide dropwise to a solution of fumaric acid and pyridine in 2-butanone and refluxing at 75°C for 18 hours. Following purification, the diester product

was then endcapped with methacrylate groups using methacryloyl chloride in the presence of trimethylamine and purified prior to use. Emulsion inks were prepared using a FlackTek Speedmixer DAC 150 FVZ-K as previously described(176). Briefly, PFDMA was combined with 10 wt% surfactant and 1 wt% of the BAPO photoinitiator and mixed for 2.5 minutes at 2500 rpm prior to emulsification. Once thoroughly mixed, an aqueous solution of calcium chloride (5 wt%) was then added to the organic phase (w:o 75:25) in three additions and mixed at 500 rpm for 2.5 minutes after each addition. A final mixing period of 2.5 minutes at 2500 rpm was used to improve homogeneity and increase viscosity for printing. The calcium chloride was used to prevent Ostwald ripening and improve homogeneity. Successful emulsion inks were typically characterized by an opaque white appearance and paste-like consistency.

The rheological properties of the PFDMA HIPE were measured using a controlled stress rheometer (Anton Paar Physica MCR 301) fitted with parallel plate geometry (Anton Paar Measuring Cone CP50-1/Q1, 50 mm diameter). A small volume (2.5 mL) of the HIPE was poured into the specimen holder at 25°C and allowed to acclimate for 60 seconds. Oscillatory-shear measurements were carried out at 1 Hz with a stress amplitude range of 0.1 to 1000 Pa. Viscometry measurements were performed at a shear rate of 0.01 to 100 s^{-1}.

3.2.2 Thermoplastic Feedstock. PCL (MW = 43K, CAS# 24980-41-4) was purchased from PolySciences, Inc, Warrington, PA. PCL feedstock was prepared by loading PCL pellets into the extruder syringe and placing upright in a vacuum oven at

100°C under full vacuum (<1 mbar) for one hour. The PCL extruder was then removed and allowed to cool to room temperature for one hour. The process was repeated five times in order to condition the feedstock and allow for greater crystallization and a higher melting temperature. Chroma-Line brand PLA (NatureWorks 4042D resin, CAS# 26100-51-6) filament, selected for its high purity and absence of pigments or additives, was purchased from justpla.com and used as received.

3.2.3 Multi-Modal Printer Modifications. A HYREL EMO-25 paste extruder was modified to create the cure-on-dispense (CoD) extruder for emulsion inks as previously described (177), **Figure 3.2A**. Briefly, 4 3-watt UV LEDs (365 nm, Mouser Electronics, Mansfield, TX) were mounted to a heat sink and affixed to the extruder syringe, approximately 50 mm above the nozzle tip. A luer lock adapter and a 22 AWG blunted stainless steel needle, 6.35 mm in length, was used as the nozzle.

The PCL extruder was created by modifying a HYREL EMO-25 extruder by adding a heater, heat sink, and nozzle, **Figure 3.2B**. The heater consists of approximately 45 cm of 24 AWG nichrome resistance wire (nichrome 60, 5.48 ohms/m, Jacobs Online) resulting in an approximate 60-watt load at 12 V. The heater wire was wrapped in kapton tape and coiled around the extruder syringe cap to isolate heating to the tip of the extruder. A custom heat sink was created to dissipate heat above the heater and further isolate the melt zone and improve extrusion responsiveness. The nozzle adapter thread was modified from a #10-32 to 6x1 mm to allow for compatibility with a standard brass 3D printer nozzle (0.4 mm nozzle, e3d-online).

A HYREL MK1 thermoplastic extruder was modified with an E3Dv6 hot end to allow for printing of PLA filament, **Figure 3.2C**. The 3D model for adapting the MK1 extruder body to the E3D hot end can be found at http://3dprint.nih.gov/discover/3dpx-003665.
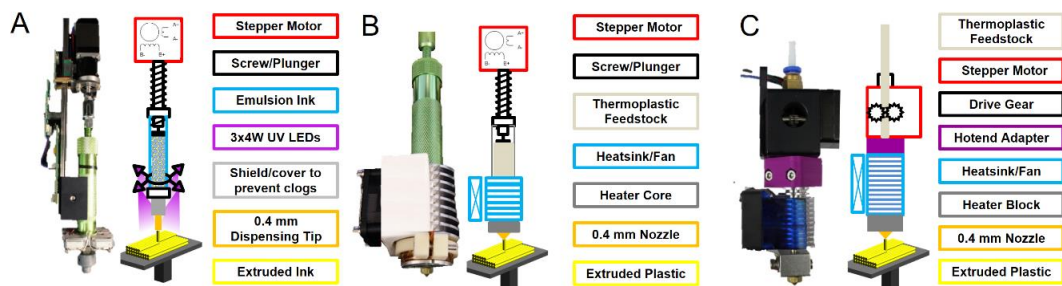
Figure 3.2 Custom setup with modified paste extruder based on HYREL EMO-25 with UV LED and heat sink for printing photocurable emulsion inks with Cure-on-Dispense (CoD) (A), modified thermoplastic extruder based on HYREL EMO-25 with heater wire, heat sink, and nozzle for printing PCL (B), modified HYREL MK1 thermoplastic filament extruder with an E3Dv6 hot end for printing of PLA (C).

The 3D printer was based on a HYREL Engine E5 modified with an open-source RAMPS v1.4 electronics set and external MOSFETs for controlling two extruders, three heaters, and four fan/LED outputs. The external MOSFETs were externally powered and accepted up to 24 V, allowing precise tuning of the voltage driving the UV LED cure source. A customized version of the open source Marlin firmware (v1.1.0 RC4) was used to allow for precise probing of the build plate with the "Auto Bed Leveling" feature and calibration of the position of the second extruder in three-dimensional space. This was particularly important to precisely dispense each material, prevent unintended overlap, and prevent collision of the heads with extruded material. Using this method, the surface

plane of the build plate was determined at a precision of ~2 µm. After the ABL procedure was performed, the height of the second extruder nozzle was then determined with a second manual probing method. The relative distance between the extruder in X and Y was calibrated using a camera mounted to the build platform. Increased-precision DRV8825 stepper drivers (Pololu Robotics and Electronics, 1/32 micro-stepping) were used for the X and Y axes to position the extruders with a microstep resolution of ~1.875 µm.

    3.2.4 Scaffold Fabrication. Simple models were created in OpenSCAD by creating a cylinder (h = 4 mm, r = 4 mm). Models with channels were generated by subtracting a spiraling pattern of rectangular channels (0.9 mm wide, 0.6 mm tall). The pattern was selected in order to allow for one layer (0.2 mm) between each channel and a rotation of 45° from one channel to the next. Complex prints of anatomical models were obtained from http://3dprint.nih.gov or http://www.thingiverse.com. G-code was created with slic3r version 1.2.9 using the following key settings: printing speeds of 10 mm/s, nonprinting speed of 25 mm/s, layer thickness of 200 µm, infill of 70 or 100% (rectilinear grid), extrusion width of 0.6 mm, one perimeter, and no top or bottom solid layers. G-code for constructs with thermoplastic shells was created by selecting the thermoplastic extruder for perimeters. To increase adhesion, masking tape was applied after probing and the print was offset by the thickness of the tape. To reduce print defects, a single skirt of thermoplastic material was used around the construct for the entire height of the print.

Repetier-Host was used to send the g-code to the printer. Custom post-processing scripts were used to position the second extruder prior to each print in order to calibrate its relative position. Additional scripts were used to move the extruders to a wipe position during every fifth retraction to keep the nozzles clean and to turn off the UV for the emulsion ink extruder when not in use. Emulsion inks were subjected to UV light with an intensity of 100 mW/cm^2 while the emulsion ink extruder was in use, and the final layer was given additional time to cure since it had no subsequent layers. No other post-print curing was performed.

3.2.5 Compressive Testing. The effect of emulsion ink infill printing and thermoplastic shell reinforcement on the compressive modulus and yield strength of the construct was investigated following guidelines from ASTM D1621-04a. Cylindrical specimens (8 mm diameter, 4mm tall) were tested using an Instron 3300 at a strain rate of 50 mm/s. The compressive modulus was calculated from the slope of the linear region and the compressive yield strength was identified, after correcting for zero strain, as the stress at the yield point or 10% strain, whichever point occurred first. Reported compressive moduli and yield strength data were averages of four printed specimens.

3.2.6 Scanning Electron Microscopy (SEM). All specimens were dried under vacuum for 24 hours to remove water prior to imaging microscale porosity and multi-material boundaries. Specimens were coated with gold and examined under SEM (JEOL 6500). A minimum of 3 printed specimens were analyzed in 4 orthogonal positions (n = 12) at the boundary between materials to evaluate the interfacial cohesion.

3.2.7 Permeability Testing. Scaffold interconnectivity was characterized by measuring Darcy permeability using the Forchheimer-Hazen-Dupuit-Darcy equation:

$$-\frac{\partial P}{\partial x} = \frac{\mu}{K}v_0 + \rho C v_0{}^2 \quad (1)$$

where -dP/dx is the pressure gradient along the sample in the direction of flow (Pa/m), μ is the dynamic viscosity of the fluid (Pa·s), K is the intrinsic permeability of the (scaffold, sample) (m^2), v_0 is the Darcy velocity (flow rate divided by cross-sectional area of the (scaffold, sample) (m/s), ρ is the density of the fluid (kg/m^3), and C is the form factor of the (scaffold, sample) (m^{-1}). Muschenborn et al. previously described the experimental details for measuring the permeability and form factor of porous polymers (178). Briefly, scaffolds were printed and inserted into a 3D printed sample holders (inner diameter = 9 mm), **Figure 3.3A**. The sample holder consisted of two mirrored pieces, bolted together, and sealed with an o-ring. Each specimen was measured with two pressure transducers (PX429-2.5G5V, Omegadyne Inc) connected at the upstream and downstream pressure port locations, **Figure 3.3B**. Water flow at room temperature was enabled via a gear pump (Chemsteel R106, Oberdorfer), a servo motor (750 W M-series, Applied Motion Products), and a motor controller (BLuAC5-Q, Applied Motion Products). The output voltage of the pressure transducers was recorded at 1 Hz through a data acquisition system (USB6251, National Instruments) for 120 seconds. The flow rate was measured manually using a stop watch and graduated cylinder. A second-order least squares of pressure gradient versus Darcy velocity was implemented for nine values to calculate permeability (K).
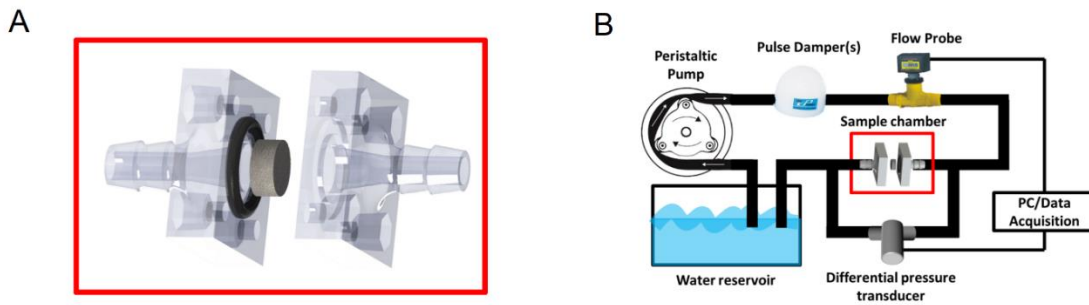
Figure 3.3 Custom permeability sample chamber (A); custom permeability testing setup schematic (B).

3.2.8 Cell Culture. Human bone marrow-derived mesenchymal stem cells (hMSCs) were obtained from the Center for the Preparation and Distribution of Adult Stem Cells at Texas A&M Health Science Center College of Medicine, Institute for Regenerative Medicine at Scott & White through NIH Grant # P40RR017447. Cells were cultured to 80% confluency in standard media containing Minimum Essential Media α (MEM α, Life Technologies) supplemented with 16.5% fetal bovine serum (FBS, Atlanta Biologicals) and 1% L-glutamine (Life Technologies) prior to passaging. All experiments were performed with cells at passage 4.

Investigation of hMSC viability and proliferation was performed to assess cell behavior on 3D printed polyHIPEs. Thin cylinders (8 mm diameter, 1mm, 100% infill) were fabricated from PFDMA polyHIPE emulsion ink. A drop of light mineral was wiped on and subsequently wiped off of the aluminum build platform to facilitate nondestructive removal of printed specimens. Prints were rinsed briefly with dichloromethane to clean the printed specimens and vacuum dried for 12 hours. Specimens were sterilized for 3 hours in 70% ethanol, subjected to a progressive wetting ladder, and incubated overnight

in MEM α supplemented with 40 w/v% FBS at 5% CO_2, 37°C. To facilitate capillary driven loading of hMSCs into the porous construct, media was removed and scaffolds allowed to dry for one hour prior to seeding at a density of 40,000 cells/cm^2. Viability at 24 and 72 hours was assessed utilizing the LIVE/DEAD assay kit (Molecular Probes). Cells were stained with 2 μM calcein-AM (live) and 2 μM ethidium homodimer-1 (dead) for 30 minutes at 37°C, washed with PBS, and imaged using a fluorescence microscope (Nikon Eclipse TE2000-S) (n = 12).

A Quant-iT™ PicoGreen® dsDNA Assay Kit (Molecular Probes) was utilized to quantify dsDNA and determine cell density at 24 and 72 hours. Briefly, specimens were placed into a new culture well, lysed, and assayed using a plate reader (Tecan Infinite M200Pro) with excitation/emission wavelengths of 480/520 nm, respectively. Average cell number (n=3) for 24 and 72 hours was determined by converting dsDNA values to individual cell number using 6.9 pg DNA/cell (179). Representative images of hMSC attachment and spreading were obtained at 72 hours. hMSCs were washed with PBS, fixed in 3.7% glutaraldehyde, stained for F-actin and nuclei with ActinGreen 488 and NucBlue ReadyProbes Reagents (Molecular Probes), and imaged using a fluorescence microscope.

3.2.9 Statistical Analysis. The values reported for the dimensional deviation, swelling ratio, mechanical properties and cell viability are presented as the mean values ± the standard deviation. One-way analysis of variance (ANOVA) with post-hoc Tukey's test ($p < 0.05$) was used for statistical analysis of data.

3.3   Results and Discussion

3.3.1 3D Printing of PFDMA Emulsion Inks. Our previous study on the development of HIPE emulsion inks identified target rheological properties for high fidelity printing (169). Specifically, we determined that a low-shear viscosity (at 0.01 s^{-1}) greater than 1000 Pa•s was needed to limit spreading after extrusion and shear thinning behavior with sufficiently low viscosity at typical printing shear rates (<50 Pa•s at a shear rate of 50 s^{-1}) allowed for facile extrusion. PFDMA emulsion inks displayed the characteristic HIPE shear thinning behavior with a low-shear viscosity of 5370 ± 580 Pa•s and a printing shear viscosity of 60 ± 10 Pa•s. A paste extruder was adapted with UV LED sources to initiate radical crosslinking of the PFDMA HIPE ink upon extrusion and harden the extruded HIPE layer prior to the addition of subsequent layers. Constructs displayed good print fidelity with hierarchical porosity from the printed architecture (~250 µm) and the emulsion-templated porosity of the polyHIPE (5-30 µm), **Figure 3.4.**
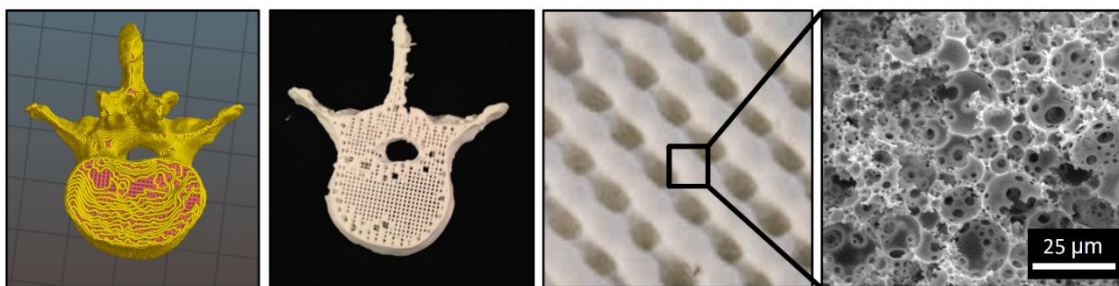
Figure 3.4. 3D printed constructs with hierarchical porosity fabricated from PFDMA emulsion ink.

3.3.2 hMSC Cytocompatibility of Printed PFDMA Emulsion Inks. A critical evaluation of candidate bone grafts is the ability of the scaffolds to support cell viability,

proliferation, and bone regeneration. Previous studies reported that fumarate-based biomaterial scaffolds with similar chemistries demonstrated in *vitro* cytocompatibility and in *vivo* biocompatibility and osteoconductivity (180-182). Furthermore, our lab previously demonstrated PFDMA polyHIPEs supported hMSC viability for up to 2 weeks and enhanced osteogenic differentiation (183). The aim of this study was to assess initial cytocompatibility of 3D printed PFDMA polyHIPEs and confirm the ability of these scaffolds to support adequate cell attachment and retention over 72 hours. A modified wicking protocol was implemented to allow for increased cell ingress into the multi-layered architecture of the print and provide increased hMSC attachment throughout the construct. Capillary forces have been demonstrated as a suitable self-seeding technique in other dual porosity systems (184). Representative images of cell-seeded constructs display cell adhesion and spreading on multiple layers of the printed PFDMA polyHIPE, **Figure 3.5A**. Viability of hMSCs seeded directly onto printed scaffolds was characterized at 24 and 72 hours and compared to standard tissue culture polystyrene (TCPS) controls, **Figure 3.5B**. Printed polyHIPEs supported hMSC viability of greater than 95% at both 24 and 72-hour time points with no statistical difference observed between the print and TCPS controls. Furthermore, printed polyHIPE scaffolds supported an approximately two-fold increase in cell density over the same time points as confirmed by dsDNA quantification, **Figure 3.5C**. These early markers of cell activity provide strong evidence for the potential of 3D printed polyHIPEs as tissue engineered scaffolds. Current work is investigating the ability of these printed polyHIPEs to support osteogenic differentiation of hMSCs.
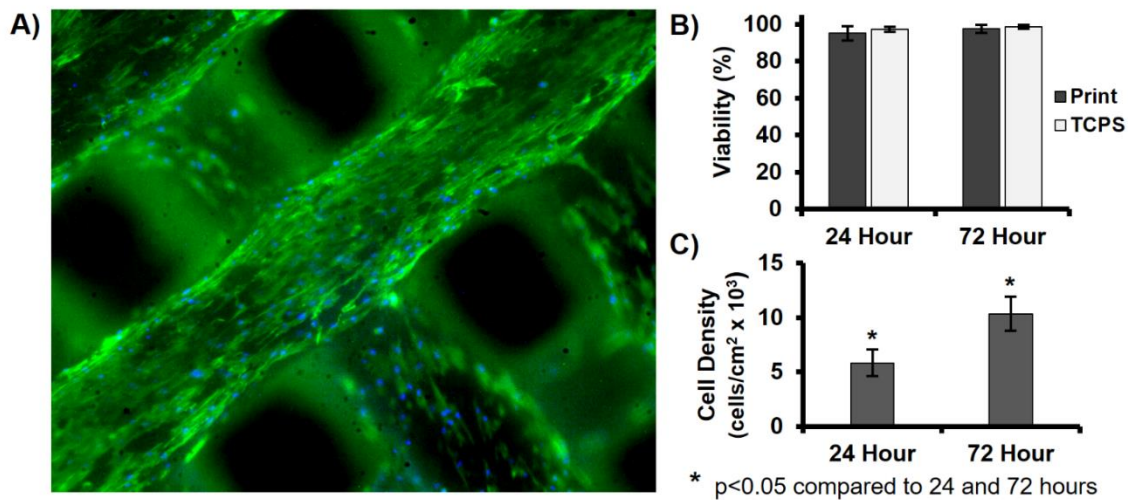
Figure 3.5. hMSC activity after 24 and 72 hours directly seeded on 3D printed polyHIPEs. A) Micrograph illustrating cell attachment and alignment on 3D printed polyHIPEs at 72 hours (blue = nuclei; green = F-actin). B) Viability of cells at each time point. C) Cell density at each time point. Color images available online at www.liebertpub.com/tea

3.3.3 Effect of Hierarchical Porosity on Scaffold Permeability. In addition to cytocompability, scaffold architecture should be designed to promote cellular infiltration and the requisite nutrient and waste transport needed to maintain cell viability prior to vascularization. (56, 185-196) Pore size alone is insufficient for predicting solute transport in porous scaffolds. Solute diffusion rates are dependent on the Darcy's permeability constant, *K,* of the porous graft. Given that permeability is dependent on a combination of the scaffold porosity, pores size, tortuosity and interconnectivity, experimental permeability measurements were used to evaluate candidate scaffolds (197). Native bone has a broad range of *K* values as expected given the structural differences between cancellous (4.45 x 10^{-8} m^2) and cortical bone (1.1 x 10^{-13} m^2) (198, 199). Common bone grafting materials range in *K* values from 9 x 10^{-9} m^2 to 2 x 10^{-11} m^2 (200), and the reported

permeability of polyHIPE constructs is on the order of $2 \times 10^{-12}\,m^2$ (201, 202). Although a requisite value for bone grafts has not been defined, it may be assumed that increased permeability allows for improved mass transport and larger graft size. We hypothesized that the high porosity of the emulsion inks would enhance permeability and that the hierarchical porosity of scaffolds with printed macropores would further increase permeability of the scaffolds. To test this hypothesis, PFDMA constructs were printed with 100% and 70% infill density, the volume of filled internal space within the perimeter lines, and then tested in a custom permeability testing setup. An exemplary plot of differential pressure vs. velocity, used to determine permeability, is shown in **Figure 3.6A**. Results of permeability testing indicated values in the range of $2\text{-}15 \times 10^{-10}\,m^2$ for 3D printed PFDMA polyHIPEs, **Figure 3.6B**. Permeability increased nearly six-fold with a decrease in infill density from 100% to 70%. These results verify that the permeability of the printed scaffolds are in the range of current bone grafting materials (200) and the ability to increase permeability with decreased infill printing. It is expected that this increased permeability will support the ability to create larger scaffolds with sufficient solute diffusion to support cell viability proliferation.
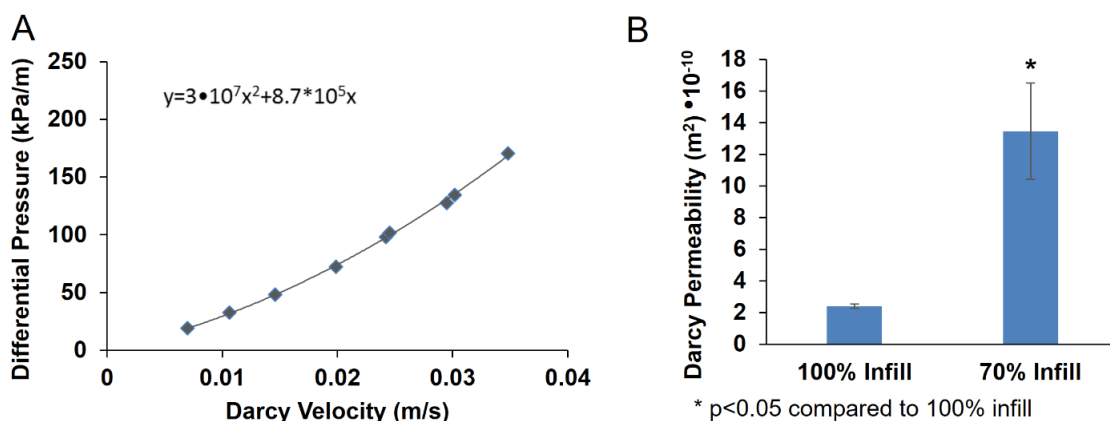
Figure 3.6. An exemplary plot of differential pressure vs. velocity used to determine permeability (A); effect of infill density on the permeability of printed constructs (B).

3.3.4 Multi-Material Printing. Although printing PFDMA polyHIPEs with decreased infill enhanced permeability, compressive testing of the scaffolds indicated that the decreased infill also resulted in a loss of compressive modulus (29.8 ± 6.7 MPa to 15.0 ± 3.9 MPa) and compressive yield strength (1.8 ± 0.3 MPa to 1.1 ± 0.2 MPa). To address this limitation, we incorporated a polyester shell to reinforce the graft and mimic the dense cortical shell that surrounds trabecular bone. This biomimetic design has the potential to enhance compressive properties while maintaining high porosity and permeability. This design required the development of a multi-modal printing setup that combined paste extrusion and high temperature thermoplastic extrusion with high positional accuracy in dual deposition, **Figure 3.7**.
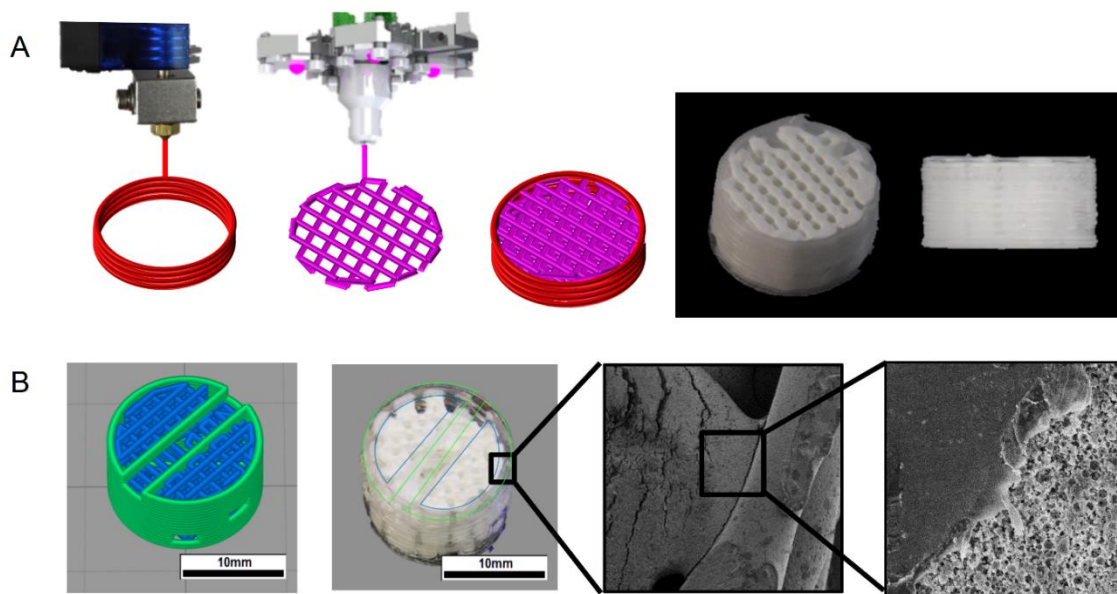
Figure 3.7. Combinatorial printing process with layer by layer deposition of the thermoplastic polyester outer shells and HIPE emulsion ink inner material (A); integration between the emulsion ink and thermoplastic (PCL) shell (B).

In order to characterize the quality of the dual printed constructs, dimensional analysis was performed on printed scaffolds and deviation from the programmed dimensions were quantified to evaluate print fidelity. Printed constructs with a height within a single layer thickness (0.2 mm) and diameter within a single extrusion width (0.6 mm) were considered high fidelity. Additional high fidelity constraints included no compounding errors and print heights >4 mm. Based on these fidelity characterizations, co-deposition was found to not detrimentally affect the quality of printed constructs. In most cases, this mechanical reinforcement also made a visible, although not quantifiable, improvement in surface finish. Printing of these complex models demonstrates the ability to create much larger constructs than typical paste extrusion methods (4 mm) including large constructs (25 mm) as illustrated in the anatomical model in **Figure 1**. Although the

rheology of these PFDMA emulsion inks was refined to print with high fidelity, there are limitations on the geometry of printable constructs. Particularly, constructs typically need an infill density of at least 70% and must have a minimal overhang angle. In contrast, traditional thermoplastic printing materials such as PLA and acrylonitrile-butadiene-styrene can consistently print with much lower infill densities and overhangs angles. By combining these two modalities, the thermoplastic material reinforces the emulsion inks, which are more likely to spread, but may also be used as a break-away support materials allowing for even greater construct complexity.

Another aspect identified critical to the success of the multi-material printing was the positional accuracy of the materials relative to each other. Syringes and needles are changed often in paste printing setups, making calibration difficult. Determination of the height offset can be readily found with a probe or shimming method, but precise X-Y positioning of the needles is more difficult. Skewing or bending of needles by even a fraction of a millimeter can cause complete overlap with previously extruded material. Therefore, enhanced precision stepper drivers (DRV8825) and a camera mounted to the build plate was used to determine X-Y position within 10 μm. The SEM images of cross sections of the hybrid scaffolds indicated good integration between the two materials, **Figure 6B.** No gaps or overlaps were found, indicating accurate positioning of the second extruder in the X-Y plane. As shown, the printed emulsion ink deposited precisely and no significant shrinkage occurred during the drying process. We hypothesized that the nearly indistinguishable gap between the materials is a result of the default 15% overlap between the perimeter and infill extrusions. This is the default overlap in the processing software

(Slic3r) to account for natural gear/belt backlash and allow for improved infill/perimeter bonding. To visualize packing of extruded lines, the cross-sectional view of a theoretical extruded line can be assumed to be a stadium (rectangle with two semicircular ends) with an overall width described by:

$$W_{extruded\ line} = 2r + w_{rectangle}\ (2)$$

where the 2r is also the layer height. Therefore, some level of overlap is necessary for one extruded line to adhere to the next, **Figure 3.8.**
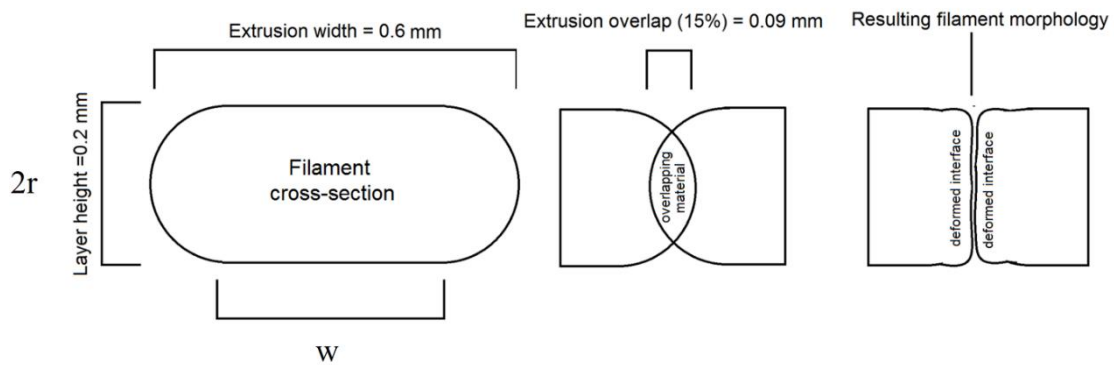
Figure 3.8. Depiction of filament overlap, explaining the nearly nonexistent gap between extruded lines.

3.3.5 Mechanical Reinforcement with Polyester Shell. Following confirmation of the high fidelity of the multi-material printing setup, the effect of the polyester shell on the mechanical properties was investigated. PCL and PLA were selected for the cortical shell based on their established compressive properties, biocompability, and biodegradation profile. One concern with reinforcing emulsion inks with a concentric is the reduction in radial diffusion and potential delay in vascularization. Kolambkar, et al.

reported the efficacy of radial improving neovascularization and tissue ingrowth of bone grafts (203). A similar approach was utilized in the printed constructs that also mimics the Volkmann canals of native bone. Constructs were printed with a spiraling pattern of rectangular channels with one layer between each channel and a rotation of 45° from one channel to the next, **Figure 3.9**. The individual and combined effects of infill density, polyester shell, and channels on the compressive properties of printed constructs was then examined.
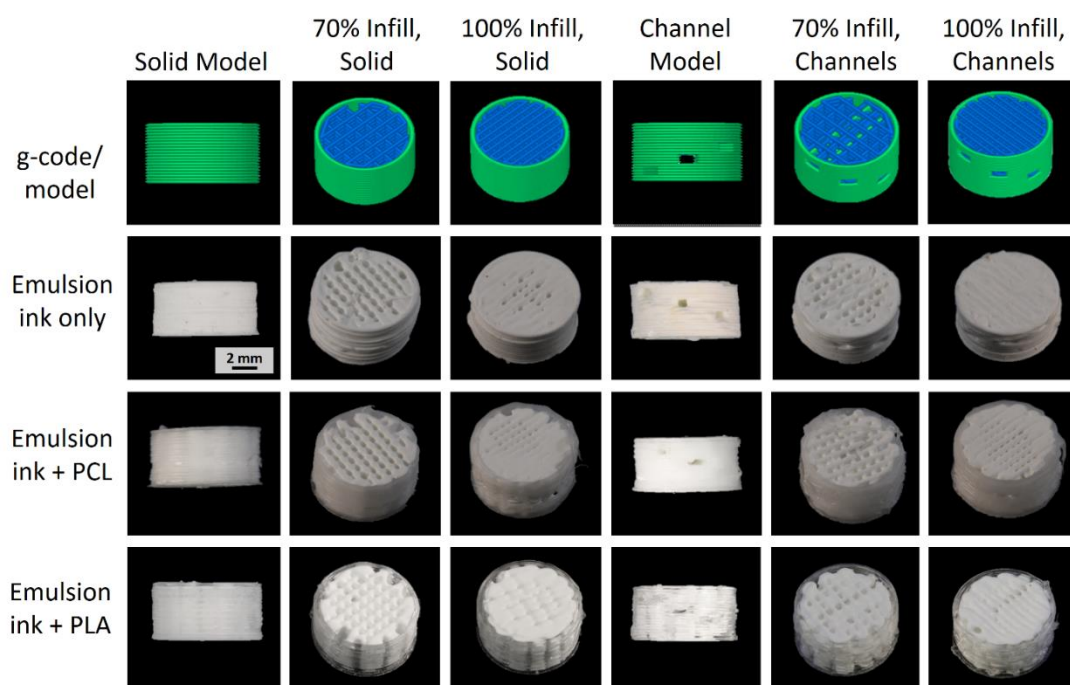
Figure 3.9. Scaffolds printed with emulsion ink only, emulsion ink with a PCL shell, or emulsion ink with a PLA shell. Models were 8 mm in diameter and 4 mm tall, and were designed with and without channels. The model, g-code renderings, and representative images are shown.

Compressive testing indicated that increase infill density and the addition of a polyester shell increased construct compressive modulus and yield strength, **Figure 3.10**. An increase in infill resulted in a statistically significant increase in modulus and compressive strength for samples with no shell and samples with a PCL shell. There was no statistically significant difference in compressive properties of grafts with PLA shells at different infill densities. It was hypothesized that a high infill level may have caused overlap with thermoplastic perimeter which cooled the deposited PLA, reducing interlayer bonding. PLA constructs with low and high infill displayed a significant increase modulus and strength compared to all other samples. PLA constructs exhibited an approximate two-fold increase in modulus compared to constructs with a PCL shell and 100% infill, and 4-6 fold increase compared to all other solid constructs. PLA constructs exhibited a 2-3 fold increase in strength compared to constructs with a PCL shell and 100% infill, and an approximate 6 fold increase compared to all other constructs. The ability to significantly increase compressive strength even at low infill density demonstrates the ability to increase permeability while maintaining mechanical properties.
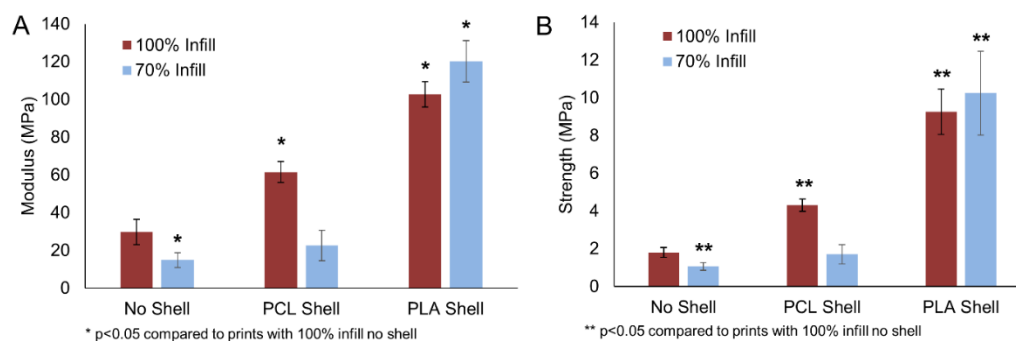
Figure 3.10. Compressive modulus (A) and yield strength (B) of multi-material scaffolds printed with 100% or 70% infill.

Comparisons of scaffolds with 70% infill density and with and without channels indicated a similar trend, **Figure 3.11**. The addition of horizontal channels resulted in a decrease in compressive modulus and yield strength of printed scaffolds, but these differences were not statistically significant. We hypothesize that the small decrease is due to the defects provided by the designed channels themselves, acting as stress concentrators. The addition of channels is hypothesized to enhanced neovascularization of the grafts post-implantation.
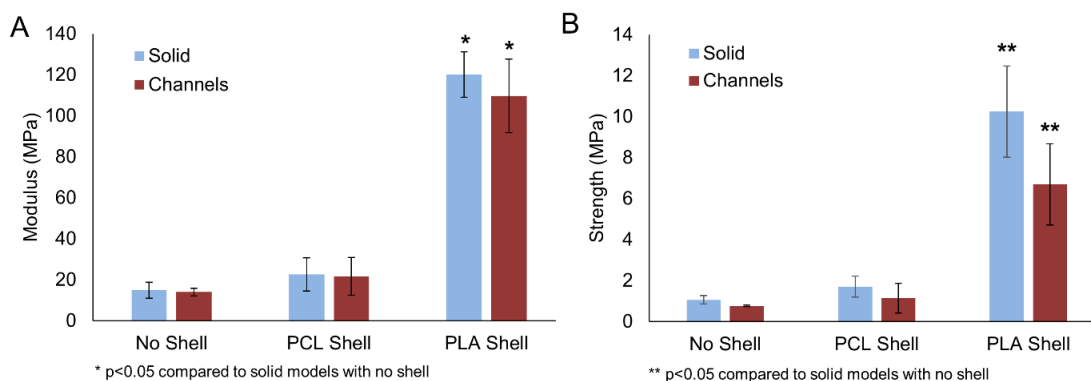
Figure 3.11. Compressive modulus (A) and yield strength (B) of multi-material scaffolds printed with and without channels at 70% infill density.

3.4 Conclusions

The variety of 3D printing technologies for tissue engineering has rapidly expanded in recent years with the availability of open source technologies and development of new inks. Traditional thermoplastic extrusion provides strong, robust constructs but is limited in the type of materials and compatibility with cells. New materials such as emulsion inks provide a biomaterial platform with high porosity and the ability to create complex tissue scaffolds with enhanced permeability. Herein, we report

the development of a biodegradable, fumarate-based emulsion ink to print robust bone grafts with designed, hierarchical porosity. A combinatory approach that utilized thermoplastic polyester printing to reinforce the emulsion ink prints was then developed to enhance compressive properties and illustrate the potential of this technique to improve scaffold biomimicry (204). The addition of either a PCL or PLA shell resulted in a significant increase in compressive modulus and yield strength with the PLA shell resulting in constructs with compressive properties in the range of trabecular bone. PLA reinforced constructs displayed significant strength, even at low infill and with the addition of horizontal channels, which highlights the ability to simultaneously increase strength and permeability. Overall, these studies demonstrate that dual modality printing can be used to improve scaffold properties and has broad potential application in the fabrication of complex tissue grafts.

4. HYDROCOLLOID EMULSION INKS FOR PRINTING SOFT TISSUE GRAFTS

4.1 Introduction

3D printing techniques such as stereolithography, powder-fusion, and extrusion-based methods have been used for biomedical applications due to their control over macro-scale and micro-scale geometry. This architectural precision allows for control of hierarchical structures ideal for tissue engineered constructs.(46) Macro-scale geometry encompasses the external appearance and structure of the final scaffold and control over this geometry allows for personalized scaffold designs that meet patient needs. For example, biomaterial can be generated based on images acquired from computed tomography (CT) scans. Micro-scale geometry allows for control over pore and channel size, orientation, and surface chemistry; which effect cell-material interactions such as cell adhesion, migration, and proliferation. Stereolithography (SLA) is able to create incredibly sophisticated models by utilizing a photopolymerizable liquid resin, but is limited to a narrow set of reactive macromers. (58) Powder-fusion based techniques are commonly printed with powders ranging in particle size from $10 - 150$ um, but are limited to one base material and must use materials that can be sintered or bound together. (167) Unlike SLA and powder-fusion based techniques, extrusion-based methods are commonly used due to its three-dimensional control over deposited material and various solidification mechanisms (curing, hardening, and gelling). The versatility of this technique permits for a wide range of printable inks such as thermoplastics(205), ceramics(27), and hydrogels(67, 100, 206).

Hydrogels are hydrophilic polymer networks capable of absorbing up to a thousand times their dry weight in water. The prepolymer composition can be tuned to modulate the mechanical, degradation, water-uptake, and cell-signaling properties of the material, allowing it to mimic soft tissue. (207, 208) SLA is the most commonly used technique for 3D printing hydrogels due to the material's low viscosity and ability to be easily photo-polymerized, though challenges still persist when developing constructs with this technique. SLA requires a large reservoir volume and post-processing to prevent construct shrinkage. In addition, this method cannot produce constructs of several cubic centimeters due to scattering of the applied laser beam, leading to constructs that are weak upon removal. (176, 209) In order to overcome such limitations, we have developed hydrogel inks for extrusion-based methods, having very little waste material, no post-processing, and allowing for fabrication of constructs with sizes and dimensions relevant to biomedical applications in short processing times. Extrusion-based methods require processing of high-viscosity materials to maintain structural integrity during extrusion.(210, 211) This method has been adapted to print hydrogels, allowing for extrusion without clogging the nozzle; however, typical precursor solutions do not have a high enough viscosity to prevent lateral spreading post-printing. (37, 69, 125, 169)

Strategies to develop hydrogel inks have focused on increasing the low shear viscosity of the precursor solutions through the incorporation of rheological additives, **Figure 4.1**. For example, Schütz et al. demonstrated that incorporation of 9% methylcellulose to a 3% alginate solution increased the viscosity at low shear rates with a corollary increase in print fidelity**.** Similarly, Chimene et al. reported that the addition of

2% nano-silicates to 5% gelatin methacrylate (GelMA) solutions also resulted in improved print fidelity due to increased viscosity at low shear.

As an alternative to these thickening agents, we recently developed hydrocolloid inks that dramatically increase the viscosity of the hydrogel solution viscosity and permit high fidelity prints. In this method a hydrophobic organic phase is dispersed within a hydrophilic aqueous phase, forming a viscous emulsion referred to as a hydrocolloid. Once extruded, the continuous phase, consisting of the hydrogel solution, is polymerized using UV irradiation to lock in the emulsion geometry. This solidification method, termed Cure-on-Dispense (CoD), allows for rapid polymerization after extrusion and provides support for successive layers. (177) Through emulsification, polymerization, and removal of the dispersed phase, hydrocolloid inks demonstrate microporosity, which is tuned by composition and processing variables. (48) Additionally, macroporosity is controlled by altering 3D printing variables such as geometry of the model, infill density, and infill configuration (rectilinear, hexagonal, and honeycomb). It is hypothesized that this micro-scale and macro-scale porosity will permit enhanced nutrient and waste transport, cell migration, and cell proliferation. (177, 212)
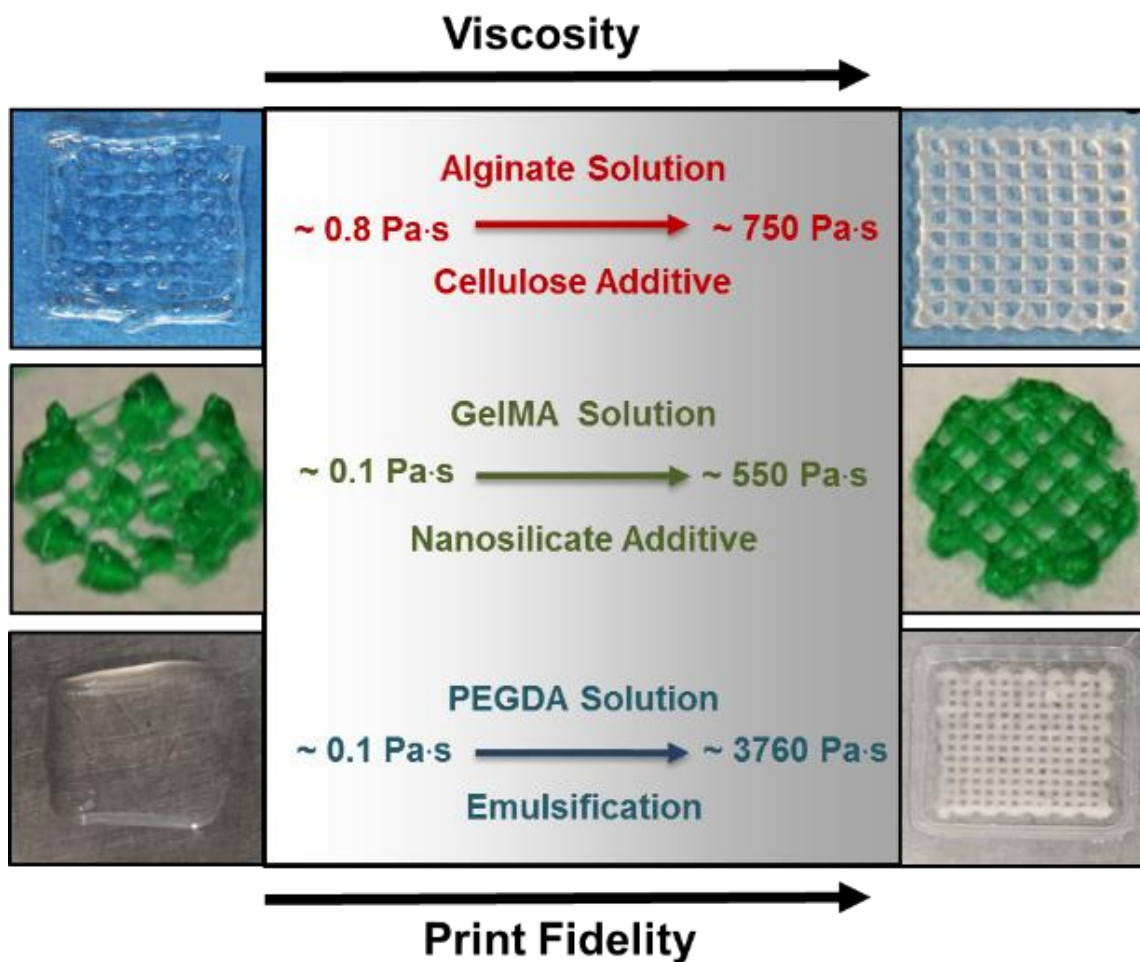
Figure 4.1. Illustration of the correlation between low shear viscosity and print fidelity for various hydrogel inks. The addition of 9% methylcellulose to 3 wt% alginate inks, tested at a shear rate of 1 s^{-1}, increased viscosity resulting in a more printable ink and higher fidelity scaffold. The addition of 2% nanosilicate additives to 5 wt% gelatin methacrylate (GelMA), tested at a shear rate of 1 s^{-1} at 37°C to prevent gelation, increased viscosity and therefore print fidelity. Emulsifying poly(ethylene glycol) diacrylate (PEGDA) with mineral oil, tested at a shear rate of 0.01 s^{-1} resulted in an increased print fidelity due to an increased viscosity. (213, 214) Adapted and Reproduced by permission from Chimene, D., Lennox, K.K., Kaunas, R.R. et al. Ann Biomed Eng (2016) 44: 2090. doi:10.1007/s10439-016-1638-y. Copyright 2015 American Chemical Society.

In the present study, we have developed hydrocolloid inks to 3D print hydrogels

using an extrusion based technique, CoD. Rheological properties of the hydrocolloid inks

were characterized in order to assess if the hydrogel inks were suitable for extrusion-based printing. Simple PEGDA hydrocolloid constructs were fabricated to analyze the effect of cross-linker addition on print fidelity, swelling, curing, and pore-architecture retention after mineral oil extraction. Complex anatomical models acquired from CT scans were printed to demonstrate the micro-scale and macro-scale precision achieved through extrusion-based printing of hydrocolloids. Finally, inks were developed out of a variety of bioactive hydrogel solutions, including cellulose, alginate, gelatin, and hyaluronic acid. Overall, these studies highlight the potential to use hydrocolloid inks for high fidelity extrusion printed constructs to be applied to biomedical applications.

4.2   Materials and Methods

4.2.1 Chemicals. All chemicals were purchased from Sigma Aldrich (Milwaukee, WI) and used as received unless otherwise noted. Trimethylolpropane ethoxylate triacrylate (TMPE-TA, Mn = 912 Da) was used in PEGDA hydrocolloids where indicated. Lithium phenyl-2,4,6-trimethylbenzoylphosphinates (LAP) photoinitiator was synthesized as previously demonstrated.(215) Light mineral oil and Kolliphor P188 surfactant were used in all ink formulations. Gelatin (type B, bovine, 225 bloom), Hyaluronic acid (bacterial glycosaminoglycan polysaccharide), and modified hydroxyethylcellulose (Natrosol™ PLUS 30 CS, Ashland, Inc, Covington, KY) were used in their respective hydrocolloid ink formulations.

4.2.2 Poly(Ethylene Glycol) Diacrylate Synthesis. PEGDA was synthesized according to a method adapted from Hahn, et al.(216) In summary, four molar equivalents

of acryloyl chloride was added dropwise to a solution containing one molar equivalent of PEG diol (6 kDa) and two molar equivalents of triethylamine in anhydrous dichloromethane (DCM) under nitrogen. After stirring for 24-hours, the resulting solution was washed with eight molar equivalents of potassium bicarbonate (2M). Once the solution was dried with anhydrous sodium sulfate, the product was precipitated in cold diethyl ether, filtered, and dried under vacuum. Proton nuclear magnetic resonance (^{1}H NMR) spectroscopy was used to confirm functionalization of PEGDA. This was recorded on Mercury 300 MHZ spectrometer using a TMS/solvent signal as an internal reference.

4.2.3. Hydrocolloid Ink Preparation. Hydrocolloid inks were prepared using the FlackTek SpeedMixer DAC 150 FVZ-K. Prior to emulsification, a PEGDA and water solution (25 w%) was mixed with Kolliphor P188 surfactant (10 w%) and LAP photoinitiator (1 w%) in the SpeedMixer cup. Some PEGDA hydrocolloids contained TMPE-TA crosslinker (5 w%) which was mixed into the aqueous phase in the previous step. Once combined, light mineral oil was added to the aqueous, hydrogel solution in four additions and mixed at 2500 rpm for 2.5 minutes each, until an 80% weight fraction is achieved. Once emulsified into an opaque, homogenous, paste-like consistency, a stir-bead (10 mm diameter and height) was added and mixed at 3500 rpm for 2.5 minutes in the speed mixer. The hydrocolloid ink fabrication process is illustrated in **Figure 4.2**. Alginate, cellulose, hyaluronic acid, and gelatin emulsions were fabricated at different concentrations due to hydrogel precursor solution viscosities (alginate, cellulose, and hyaluronic acid at 2 w% and gelatin at 10 w%). These hydrocolloids were utilized to

demonstrate an ideal printing viscosity can be obtained through emulsification of various

bioactive materials, producing constructs with high print fidelity.
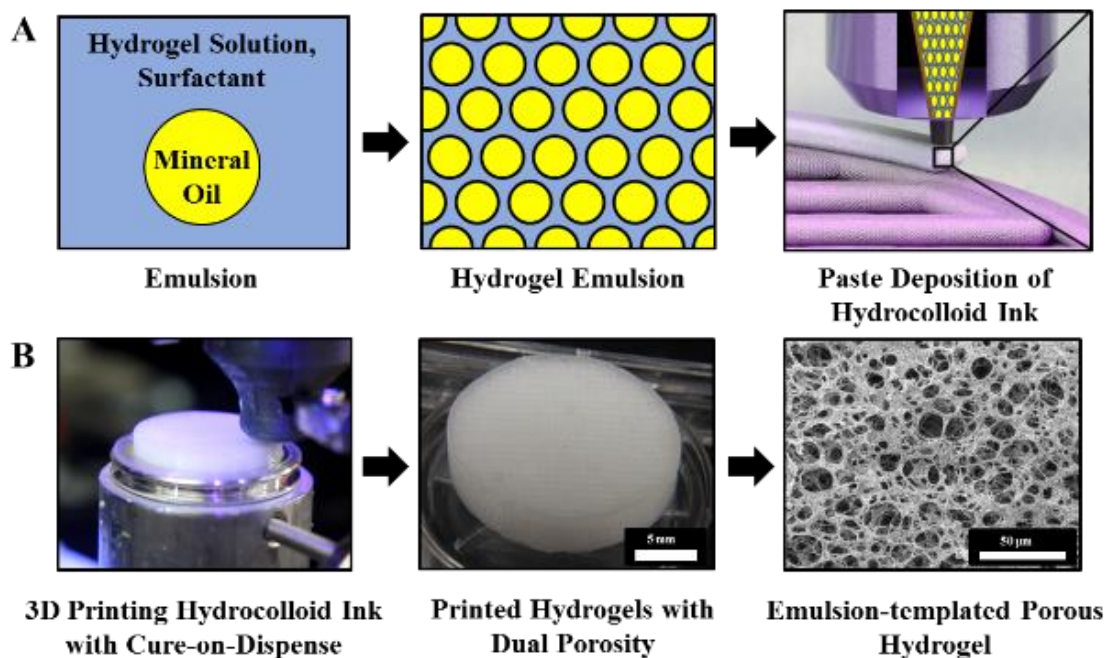
Figure 4.2. Schematic showing the fabrication of hydrocolloid inks and creation of a hierarchically porous scaffold via extrusion deposition printing with cure-on-dispense.

4.2.4 Ink Rheology. The rheological properties of hydrogel precursor solutions

and corresponding hydrocolloid inks were characterized using a controlled stress

rheometer (Anton Paar Physica MCR 301) fitted with parallel plate geometry (Anton Paar

Measuring Cone CP50-1/Q1, 50 mm diameter). The parallel plate temperatures were kept

constant at 25^0C for all samples tested except for gelatin solution, which was held at 35^0C

to prevent gelation. A small volume was loaded between parallel plates and allowed to

acclimate for 60 seconds before testing. Viscometry measurements were performed at a

shear rate between 0.01 and 100 s^{-1}.

71

4.2.5 Cure-on Dispense Hardware Customizations. 3D-printed hydrocolloids were fabricated utilizing a RepRap Prusa i3 Engine E5 modified with an open-source RAMPS v1.4 electronics set and external MOSFETs. Hydrocolloids were loaded into a customized a HYREL EMO-25 extruder equipped with a luer lock adapter and a 22 gauge blunted stainless steel needle (413 µm, 6.35 mm in length, Sigma Aldrich). The HYREL EMO-25 extruder was modified to print emulsion inks using CoD. Briefly, four 3-watt ultraviolet (UV) LEDs (365 nm, Mouser Electronics, Mansfield, TX) were mounted to a heat sink and affixed to the extruder syringe, approximately 50 mm above the nozzle tip. Open source Marlin firmware (v1.1.0 RC4) was used to allow for precise probing of the build plate with the "Auto Bed Leveling" feature. This feature placed the extruder nozzle at a consistent distance from the build plate, with a precision of ~2 µm.

4.2.6 Printing Parameters. Constructs were developed in OpenSCAD program by creating a cylinder (h=4 mm, r=20 mm) which was then imported into the "slicing" software, Slic3r version 1.2.9. This software converts the model into instructions for the printer by generating a G-code with the following printing parameters: printing speed of 10 mm/s, nonprinting speed of 25 mm/s, layer thickness of 200 µm, rectilinear grid infill of 70%, extrusion width of 0.6 mm, one perimeter, and no top or bottom solid layers. The G-code is sent to the printer through Repetier-Host which contains post-processing scripts to move the extruder to a wipe position during every fifth retraction in order to prevent the nozzle from clogging.

Constructs were subjected to UV light after printing the final layer to initialize radical crosslinking and harden the extruded hydrocolloid ink. The MOSFETs are externally powered to accept up to 24 V which allows for precise tuning of the voltage driving the UV LED cure source. Hydrocolloid inks were subjected to UV with an intensity of 0, 10, or 100 mW/cm^2 after printing the final layer with 100 mW/cm^2 for 5 seconds.

Several geometries were selected to demonstrate the ability to print large, complex constructs with these hydrocolloid inks using CoD technology. These complex geometries are modeled in Solidworks based on CT data and then imported into the "slicing" software to be printed using the same parameters as the simple constructs mentioned above.

4.2.7 Mineral Oil Extraction. The removal of the organic phase from printed constructs was required for accurate characterization. Post-printing, specimens was submerged in a series of solutions consisting of DCM for oil removal and ethanol for water removal. Various concentrations of DCM and ethanol were used to ensure maintenance of architecture without pore collapse. The constructs were first soaked in a 50/50 v/v mixture of DCM and ethanol for 1 hour. After this mixture, the specimen was soaked in pure DCM to remove any excess oil and then placed into another DCM and ethanol mixture (50/50 v/v), both lasting an hour. Constructs were soaked in ethanol for one hour before being soaked in water overnight. After extraction and swelling in water overnight, constructs were frozen at -80°C and lyophilized for 24 hours.

4.2.8 Dimensional Analysis and Swelling Ratio. Print fidelity was assessed through dimensional analysis of the constructs. This was completed by comparing the sample's dimensions to the programmed dimensions. High fidelity was considered to be constructs containing a height within a single layer thickness (0.2mm) and diameter within a single extrusion width (0.6mm).

The swelling ratio of the constructs was then compared to the original dimensions after printing. After mineral oil extraction and lyophilizing, samples were weighed to determine the samples dry mass (m_d). The hydrocolloid constructs were swollen for 24 hours in reverse osmosis water and weighed to determine the equilibrium swollen mass (m_s). The equilibrium volumetric swelling ratio, Q was calculated from the equilibrium mass swelling ratio:

$$Q = \frac{m_s - m_d}{m_d} \ (18)$$

4.2.9 Scanning Electron Microscopy (SEM). SEM (JOEL 6500) was utilized to image all specimens and determine the average pore of hydrocolloids ink with and without TMPE-TA cross-linker. Samples were dried for 24 hours *in vacuo* in order to remove residual water prior to characterizing construct's pore architecture. Six printed constructs, three with cross-linker and three without, were fractured in at the center, sectioned into quarters, and sputtercoated with gold. Each specimen was then imaged in a rastor pattern, yielding 5 images per construct making a total of 30 images. Images at 1000x magnification were utilized to determine the average pore size on the first 10 pores that cross the median of each micrograph to minimize user bias. A statistical correction was

calculated to account for non-perfect spherical pores, $h_2 = R_2 - r_2$, where R is the void diameter's equatorial value, r is the diameters value measured from the micrograph, and h is the distance from the center. (19) The average diameter values were multiplied by this correction factor to yield a more accurate representation of the pore diameter.

4.2.10 Statistical Analysis. All values reported are presented as the mean values ± the standard deviation. A Student's t-test was performed on the dimensional analysis to determine any statistical significant differences between compositions. This test was conducted at a 95% confidence interval, having statistical significance at p values less than 0.05.

4.3   Results and Discussion

PEGDA hydrogels are resistant to protein adsorption and cell adhesion, providing a bioinert material ideal for biomedical applications. (217, 218) Additionally, these hydrogels produce adaptable biomaterial systems due to their varied tunability and biocompatibility.(207, 219-222) This material is well characterized in literature due to the range of mechanical and physical properties that can be achieved through changes in molecular weight, concentration, and functionality. (223-227) With this in mind, PEGDA hydrogels were analyzed to create hydrocolloid ink constructs with high print fidelity.

4.3.1 Ink Rheology. In order to evaluate the potential for printability, rheological properties of PEGDA hydrocolloid formulations and constituent solutions were tested. PEGDA solution exhibited a relatively constant viscosity of 1 Pa·s for shear rates between 0.01 and 100 s^{-1}, while PEGDA hydrocolloids exhibited a sufficiently low viscosity (<10

Pa·s) at typical printing shear rates (50 s^{-1}) and an adequately high viscosity (>1000 Pa·s) at low shear rates (0.01 s^{-1}), **Figure 4.3A**. The rheological profile of the PEGDA hydrocolloid allows for extrusion through a needle without clogging at high shears, and allows for shape retention once extruded onto the build platform.

In order to correlate rheology with printed construct fidelity, tall, simple constructs (cylinder, r=10 mm, h=4 mm) of PEGDA Hydrocolloids and PEGDA solution were printed. Print fidelity was then determined by dimensional analysis as compared to the programmed dimensions. Deviation from the designed construct dimensions were quantified. Hydrocolloid with a height within a single layer thickness (0.2 mm) and diameter within a single extrusion width (0.6 mm) were considered high fidelity. A chart of measurements for diameter, height, and the extruded strand width is provided, **Figure 4.3B.** The PEGDA hydrocolloid is capable of creating tall, high fidelity constructs with no catastrophic failures, however PEGDA solution completely fails to hold its shape after extrusion, **Figure 4.3C**.
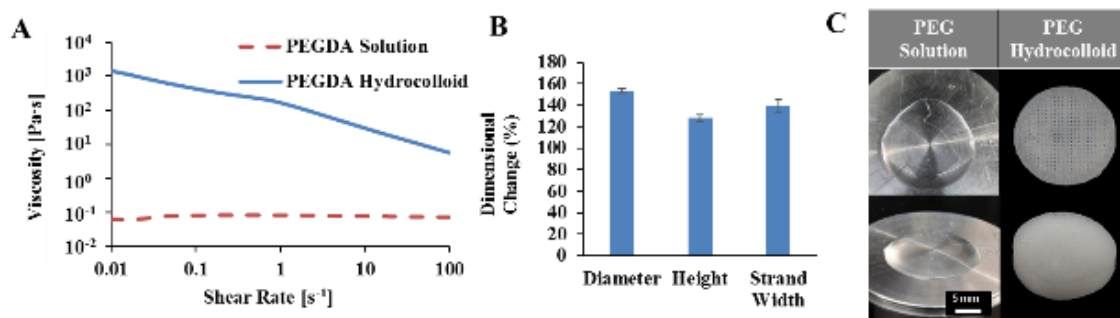
Figure 4.3. Log-log plots of PEGDA precursor solution and PEGDA hydrocolloid viscosity as a function of shear rate (A). Scaffold Fidelity measurements for diameter, height, and strand width of PEGDA hydrocolloids (B). Examples of printed constructs shown from top and orthogonal view (C).

4.3.2. Effect of Cure Rate on Print Fidelity. Although construct shape could be maintained without active curing throughout the print, some method of curing was necessary to solidify and manipulation the construct. Attempts to remove uncured hydrocolloids from the printing bed resulted in severe damage to construct geometry and completely disperses when soaked in water, **Figure 4.5**. Scaffolds cured with high intensity UV light throughout the print (100 mW/cm^2) were robust and easy to manipulate, but delaminated when swelled in water. We hypothesize that this is the result of initiator depletion by the UV source, causing a reduced availability of free radicals when the following layer is deposited and prevents bonding between layers. An optimal level of 10 mW/cm^2 was experimentally determined to be the optimal curing mechanism. This method allowed for a cohesive, manipulatable construct that did not delaminate in water. The reduced intensity allows for adequate curing without substantial depleting the initiator, allowing for improved inter-layer bonding
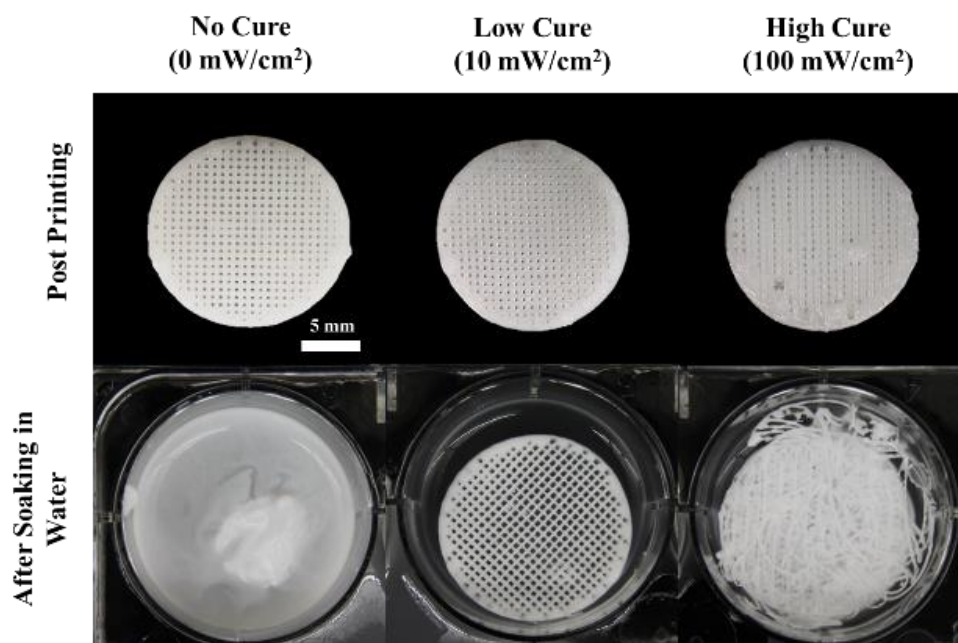
Figure 4.4. The effect of cure rate (0-100mW/cm^2) on fidelity and integrity of printed PEGDA hydrocolloid inks. Constructs are shown immediately after printing (top) and after soaking in water (bottom).

4.3.3 Dimensional Analysis and Swelling Ratio. Hydrogels have the ability to swell in aqueous systems because it is able to retain the solvents forming a swollen gel phase.(228) These swelling properties affect the constructs overall geometry, therefore when applied to 3D printing a final, expanded shape that matches the native model is desired.(208)

Hydrocolloid inks containing TMPE cross-linker maintained dimensions closer to the original printed size. These constructs did not swell as much compared to samples without TMPE cross-linker during mineral oil extraction. The also produced significantly smaller lyophilized and equilibrium swollen constructs compared to constructs without TMPE, **Figure 4.5A.** A chart comparing feature retention including height, diameter, and

strand width between constructs with and without TMPE is provided, **Figure 4.5B**, as well as a comparison between the equilibrium swelling ratios, **Figure 4.5C**. Scaffold diameters and swelling ratios were found to be statistically significantly different between PEG hydrocolloids without TMPE and those with TMPE. This suggests that the constructs expanded outward rather than inward due to the surface tension on the inner walls. Alternatively, there was no significant difference between construct heights and strand width. It is hypothesized that this occurs due to the constructs geometry causes the surrounding perimeter to be firmly joined together due to direct stacking on top of one another. Alternatively, the height and strand width is dependent on the infill, which is alternating to make a 3D mesh, causing the constructs to swell in this direction. Overall, this shows the ability to reduce swelling and dimensional changes in hydrocolloids through the addition of TMPE cross-linker, permitting printing of geometrically accurate constructs without requiring substantial compensation for predicted swelling.
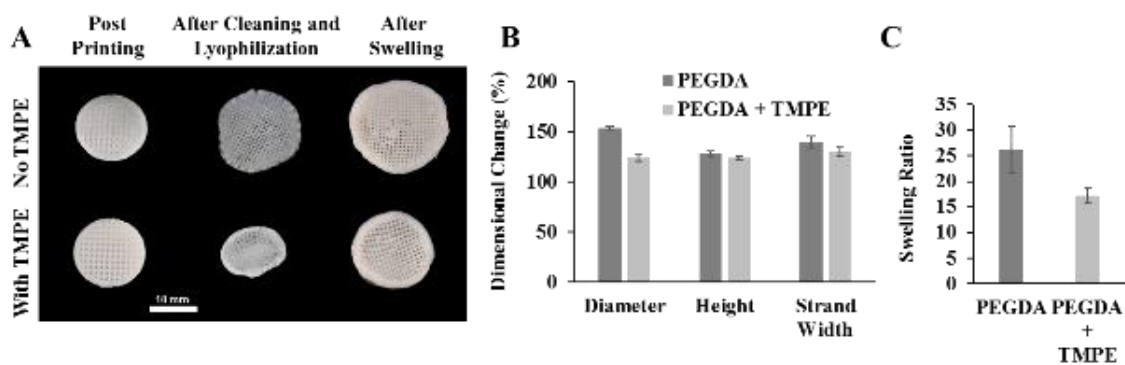
Figure 4.5. The effect of adding TMPE cross-linker post printing, after cleaning and lyophilizing, and after swelling (A). Comparison of PEGDA and PEGDA + TMPE cross-linker on scaffold fidelity (B) and swelling (C).

4.3.4 Mineral Oil Extraction. Hydrogel viscosity is increased though emulsification with mineral oil. The dispersed mineral oil makes up the immiscible, hydrophobic phase of the oil in water emulsion, forming tiny droplets within the polymerized hydrogel solution. Once the hydrogel is cured, the droplet size is extracted from the hydrocolloid construct, exposing the pore architecture and permitting nutrient and waste transport, cell migration, and cell proliferation. (177, 212)

Extraction was first attempted with the single solvents water, DCM, and ethanol. Soaking in water caused the gels to swell, but no significant mineral oil extraction was observed. Soaking in DCM allowed for some extraction of mineral oil, but this process was slow and incomplete, likely due to the hydrophobicity of the solvent and hydrophilicity of the hydrogel phase. Ethanol provided modest results in extracting mineral oil due to its increased hydrophobicity compared to water, however, it's miscibility with water enabled it to displace some of the water in the hydrogel. A 50/50 mixture of DCM/ethanol was most successful as a first soak to displace both mineral oil and water from the printed hydrocolloid scaffolds. This enabled the most thorough removal of mineral oil in timely manner. Scaffolds were subsequently washed with pure DCM, ramped back through ethanol, and concluded with water to yield fully hydrated scaffolds. Scaffolds were noticeably larger both before and after lyophilization, indicating mineral oil extraction had an effect on morphology.

4.3.5 Construct Porosity. Biomaterial constructs are designed to restore function and provide environments that support cell differentiation and proliferation and therefore

are produced to mimic important aspects of the target tissue. Porous, interconnected structures is a desirable trait for biomaterial structures, enabling cellular ingrowth and proliferation, vascularization, and nutrient and metabolic waste transport. (177, 212) Mineral oil droplet size within the hydrocolloid ink is directly related to the construct pore size and architecture. Interconnected, porous constructs are produced by extracting mineral oil from the polymerized hydrogel. Incorporating porosity into the 3D model, hierarchical porosity and complex features can be achieved. Lyophilized scaffolds were cryo-fractured and examined under SEM to elucidate the morphology of the printed hydrocolloid material after mineral oil extraction, **Figure 4.6**. While pores are visible under SEM, reproducibility due to shrinkage during lyophilization has so far prevented quantification.

Hydrogel Emulsion Porosity
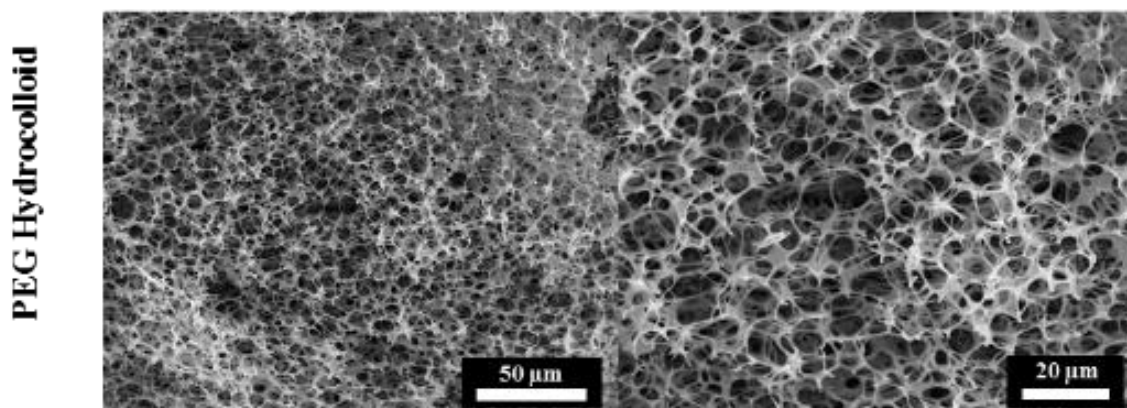
Figure 4.6. SEM of cured hydrocolloid inks displaying interconnect, porous nature after mineral oil extraction low magnification (500x, left), high magnification (1000x, right).

81

4.3.6 Complex Anatomical Prints. In order to demonstrate the capabilities of this system, various anatomical models were printed with the standard PEGDA hydrocolloid ink. A nose model (http://x3dm.com/3D-Model/Human_nose_3351.htm), simple bifurcating vessel (designed in Solidworks), semilunar valve (http://3dprint.nih.gov/discover/3dpx-000452), and a portion of a double aortic arch (http://3dprint.nih.gov/discover/3dpx-001204) are shown, **Figure 4.7.** Each model shows an increasing degree of complexity and showcases the inks ability to develop porous, complex anatomical models without any dimensional compensation.

Figure 4.7. Complex anatomical models printed to demonstrate the clinical applications and versatility of these hydrocolloid inks and the extrusion CoD technology. Models printed (from left to right) include a nose, bifurcating vessel, semilunar valve, and congenital deformity of an aortic arch. Resulting printed constructs are shown below each model to demonstrate the quality and detail afforded by the hydrocolloid inks.

4.3.7 Bio-Hydrocolloid Inks. Natural polymers, such as gelatin, alginate, cellulose, and hyaluronic acid are used to create a supportive microenvironment for cells, therefore considered bioinks. (229) Gelatin is hydrolyzed collagen that are commonly used

in tissue engineering due to its cell binding RGD domains. (221) Similarly, alginate is also used in tissue engineering, but does not contain any cell binding sites. Instead, this anionic polysaccharide obtained from seaweed and algae can blended or modified with molecules to have cell binding domains. (229)(Cellulose is also a polysaccharide that derived from plants as well as is a bioactive and biocompatible material. (230) Hyaluronic acid is also biocompatible as well as nonimmunogenic and nonadhesive. This material is considered a glycosaminoglycan that is a natural component of the extracellular matrix. (231) However, these natural bioinks lack the viscosity at low concentrations or mechanical properties to achieve good print fidelity. (229) By emulsifying these materials, a rheological profile ideal for printing can be obtained at relatively low concentrations.

All bio-hydrocolloid inks showed similar rheological behaviors, having a high viscosity at low shear (0.01 s^{-1}) and low viscosity at typical printing shear (100 s^{-1}), **Figure 4.3A.** A comparison of low shear viscosities between hydrogel precursor solutions and hydrocolloid inks were made to present the importance of emulsification on ink rheology and therefore print fidelity, **Figure 4.3B.** Low shear viscosities of precursor solutions ranged from 0.1 Pa•s (PEGDA) to 200 Pa•s (hyaluronic acid). Hydrocolloid inks, however, displayed low-shear viscosities ranging from 2,810 Pa•s (alginate) to 13,400 Pa•s (gelatin).   The rheological profile for bioactive hydrocolloid inks allows for constructs to be printed with high fidelity, **Figure 4.3C**.
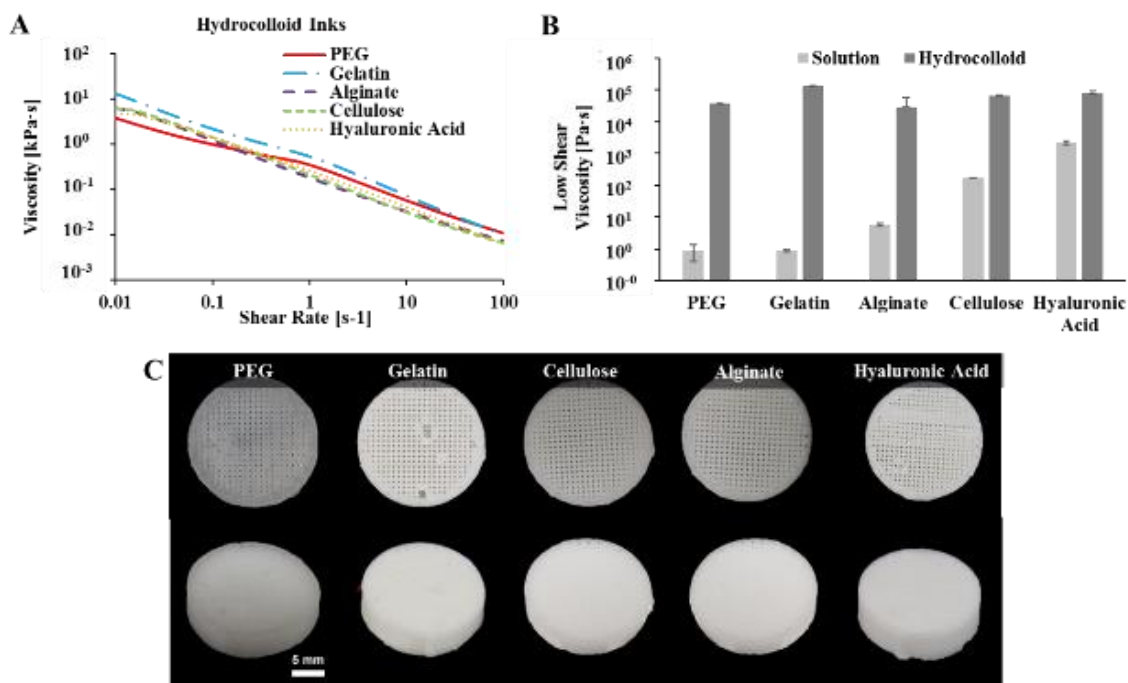
Figure 4.8. Log-log plot of viscosity as a function of shear rate for hydrocolloid inks made from various hydrogel solutions (PEG, hyaluronic acid, gelatin, cellulose, alginate) (A). Comparison of low-shear (0.01 s^{-1}) viscosities of hydrogel precursor solutions and their hydrocolloid inks (B). Scaffold printed with corresponding inks to illustrate successful hydrocolloid ink formation of various hydrocolloids (C).

4.4 Conclusions

3D printing is an exciting new area of innovation for tissue engineering that promises to revolutionize the way we fabricate engineered tissue scaffolds. Due to their low viscosity, high fidelity printing of hydrogels has typically been limited to SLA methods. Many of these materials have been adapted for use with extrusion based methods, but are limited by poor shape retention after extrusion and the need for thickener additives, support mediums, and harsh curing conditions. In order to allow wider compatibility with SFF, a more extensible system is necessary to allow modification of rheological properties without major modification to the hydrogel composition.

In this study, we demonstrate the ability to create printable hydrogel foams by adapting our emulsion ink method. This allows the creation of oil-in-water emulsions, termed hydrocolloid inks, to facilitate printing of hydrogels. These inks capable of fabricating scaffolds with hierarchical porosity using common materials, inexpensive equipment, and minimal processing. In addition to common PEG-based hydrogels, we've shown this method can be used to print a large variety of hydrogel solutions and very low concentrations and achieve high fidelity. Finally, we've demonstrated the ability to print complex anatomical models, rarely possible with this type of extrusion method. These 3D printed hydrogel scaffolds represent some of the highest fidelity reproductions of complex anatomical geometries in the literature to date. Overall, this new class of inks allows for fabrication of custom tissue engineered grafts for soft tissue regeneration with countless new materials and substantial increases in fidelity.

5. CONCLUSIONS AND FUTURE DIRECTIONS

5.1 Summary

This body of work presents a new strategy for creating porous tissue engineered scaffolds utilizing hybrid 3D printing techniques. Critical components in the development of this emulsion ink platform were: recent advances additive manufacturing, progress in HIPE formulations, and, in particular, recent work by our group on the development of biodegradable, osteoinductive, fumarate-based HIPEs. These highly customizable scaffolds address many of the current limitations of autologous and allogenic grafts by providing an engineered graft with tunable material properties and functionality.

Emulsion inks were demonstrated in various forms, and were capable of recreating complex anatomical geometries. Water-in-oil based HIPE inks displayed good reproduction fidelity, augmented by the new cure-on-dispense hybrid printing method. These rigid scaffolds were enhanced by hybridizing the print method with traditional thermoplastic extrusion to create robust, strong scaffolds. These scaffolds displayed multiscale porosity and biomimetic design unlike what is possible with any other current technique. This platform was further expanded by developing oil-in-water hydrocolloid inks to allow for extrusion printing of hydrogels with great detail and fidelity. Hydrocolloid inks were prepared from a variety of materials and displayed similar printability and promising fidelity.

In all steps, rheological characterization was crucial. Initial discovery of minimum viscosity at low shear rates was central to the tuning of printable emulsion inks. While

rheological properties for water-in-oil emulsions satisfied the minimum requirements, high cure was necessary for high fidelity printing. In contrast, hydrocolloid inks attained significantly higher rheology and required much lower cure intensity to prevent delamination.

Development of these ink, processing, and print methods has contributed to a modular low-cost, open-source platform for printing porous, curable biomaterials for hard and soft tissue engineering. This work highlights successes with our PFDMA polyHIPE system as well as cure-on-dispense paste extrusion printing. Beyond our specific applications, the structure property relationships and methodologies elucidated from this work can be utilized to create more functional tissue engineered scaffolds. Specifically, the use of extrusion based printing opens the door for other multimaterial printing with enhanced cell-material interactions and the potential for multiple cell types.

In summary, we have developed printable emulsion inks based on high internal phase emulsions that enable fabrication of complex, hierarchically porous tissue engineered scaffolds. Furthermore, we have demonstrated that this methodology for creating emulsion inks, allows for formulation of inks from a wide variety of materials, , including hydrogels which have often proven challenging to print.

5.2   Significance of Work

Chapter 2 described fabrication and development of printable emulsion inks. Initial feasibility of 3D printing emulsion inks was first demonstrated with commercially available macromers. With a large range of material properties it was possible to carefully tune the emulsion formulation and determine the optimal rheological profile. Varying cure

parameters revealed the need for a high intensity, cure-on-dispense polymerization mechanism. Adjustments to the geometric parameters of the slicing software allowed the development of an optimal recipe for printing of low viscosity pastes. These advances allowed the creation of large (~1 in) scaffolds of actual tissues recreated from CT scans and MRI imaging. In addition to the numerous tunable parameters, this UV polymerization mechanism provides a significantly increased polymerization efficiency compared to previously demonstrated thermal or redox polymerization mechanisms. Thorough control allowed for modulation of properties such as infill density to increase permeability, however mechanical properties of these polyHIPEs were limited.

In Chapter 3, a hybrid printing method was developed from emulsion inks and traditional thermoplastic extrusion of PLA in order to increase the strength of printed scaffolds. With a well-developed methodology for creating emulsion inks in place PFDMA polyHIPEs were developed into inks to serve as a biodegradable, biocompatible, osteoinductive material as the basis of our scaffold. By reinforcing the scaffolds with PLA, strength and permeability were simultaneously increased to provide a graft with mechanical and permeability properties within an order of magnitude of cancellous bone.

Finally, in Chapter 4, this same emulsion ink strategy was employed to create hydrocolloid inks capable of simulating soft tissues. Optimizing rheological and cure properties allowed for cure-on-dispense extrusion printing of large (~1 in) constructs. These formulations incorporate mineral oil as the porogen, which must be extracted, but constructs remain strong and cohesive throughout cleaning procedure. Current printed hydrogel inks rely on increased concentration to provide adequate rheological properties.

However, this leads to a dense, non-optimal polymer network, and is often still insufficient, yielding an inaccurate construct. Initial hydrocolloid inks were demonstration with PEGDA solution due to its prevalence and low viscosity. Typical PEGDA solutions are not printable with an extrusion method due to their viscosity, however PEGDA hydrocolloids had exemplary rheological and cure properties and created high fidelity scaffolds, suggesting that a hydrocolloid ink may be formed from nearly any emulsifiable hydrogel solution. Various common hydrogel biomaterials including cellulose, gelatin, alginate, and hyaluronic acid were successfully used to demonstrate this ability.

In summary, these studies have resulted in a method to improve fidelity and printablity of current bioinks, as well as the development of bioinks that were not previously possible. With these highly refined inks, scaffolds with more complex features such as low infill, and fine details such as internal voids and vascular channels are now possible.

5.3   Challenges and Future Directions

Development of these emulsion inks lays the foundation for a new class of printable biomaterials with innate porosity; a fundamental necessity for tissue engineered scaffolds. These inks are highly tunable and can be refined to allow fabrication of complex scaffolds. Although we have demonstrated feasibility to simulate various tissues, considerable work will be necessary to develop these into functional tissues.

PolyHIPEs provide a very tunable system due to their modular nature, and pore sizes have been shown from tens to hundreds of microns. However, due to the rheological constraints of the cure-on-dispense printing process high emulsification leads to very

small pores (~10 μm). It has been reported that pore sizes ranging from 50 – 400 μm are required to promote full bone healing.(232) Therefore, it would be advantageous to decouple these two features to allow for the development of inks with larger pores while retaining the requisite rheological properties. Furthermore, even with the current rheological profile, polyHIPE emulsion inks have the bare minimum viscosity at low shear rates. With improved rheology, cure rate could be decreased into the same range as hydrocolloid inks (~10 mW/cm^2).

Emulsion inks can be expanded to an endless variety of reactive macromers. Other chemistries such as thiol-ene(233) and vinyl(234) have been demonstrated, and alternate polymerization mechanisms such as redox(175) and thermal(235) also hold promise. The new array of usable biomaterials for hydrocolloid allows for other polymerization methods such as ionic(236), and the use of reactive agents such as genipin(237) and glutaraldehyde(238).

Hybrid multimaterial printing shows great promise to reproduce complex tissue architectures. Emulsion and hydrocolloid inks could be combined to create reinforced hydrogels with a permeable yet protective skin. Multiple emulsion or hydrocolloid inks could be used to create multimaterial scaffolds with different affinities for cell types or isolated elution of drug or growth factors. Alternative non-inverted HIPE emulsion inks could be formulated to create scaffolds with much lower permeability to act as a more effective division or boundary, and used in conjunction with other inks in order to recapitulate some of the complexity of native tissue.

Finally, these scaffolds have been fabricated and tested in the lab, and while evaluation of their *in vitro* properties appears promising, *in vivo* testing is essential to truly advance the knowledge of graft performance. The load-bearing nature of emulsion inks may require long term evaluation of mechanical properties throughout implantation. Cell proliferation and remodeling of biodegradable hydrocolloid inks will illustrate the regenerative capacity of these scaffolds.

Although there are many studies remaining before these devices can be used in the clinic, this methodology opens the door to endless inks for printing tissue engineered scaffolds. These new inks increase the potential complexity of biomaterial scaffolds while providing the most fundamental need for tissue grafts; porosity. The studies proposed would further improve the knowledge of emulsion inks, their capabilities, and *in vivo* scaffold performance.

REFERENCES

1. Langer, R., and Vacanti, J.P. Tissue Engineering: The Challenges Ahead. Scientific American1999. pp. 86.

2. Blitterswijk, C.A.v., Moroni, L., Rouwkema, J., Siddappa, R., and Sohier, J. Tissue Engineering – An Introduction. Tissue Engineering. Burlington: Academic Press; 2008. pp. xii.

3. Bhatia, S.N., and Chen, C.S. Tissue Engineering at the Micro-Scale. Biomedical Microdevices **2**, 131, 1999.

4. Sakiyama-Elbert, S., and Hubbell, J. Functional Biomaterials : Design of Novel Biomaterials. Annual Review of Materials Research **31**, 183, 2001.

5. Oberpenning, F., Meng, J., Yoo, J.J., and Atala, A. De novo reconstitution of a functional mammalian urinary bladder by tissue engineering. Nature Biotechnology **17**, 149, 1999.

6. Freed, L.E., and Vunjak-Novakovic, G. Chapter 13 - Tissue Engineering Bioreactors. In: Vacanti R.P., Lanza R., Langer J., eds. Principles of Tissue Engineering (Second Edition). San Diego: Academic Press; 2000. pp. 143.

7. König, F., Hollweck, T., Pfeifer, S., Reichart, B., Wintermantel, E., Hagl, C., and Akra, B. A Pulsatile Bioreactor for Conditioning of Tissue-Engineered Cardiovascular Constructs under Endoscopic Visualization. Journal of Functional Biomaterials **3**, 480, 2005.

8. Mol, A., Driessen, N.J.B., Rutten, M.C.M., Hoerstrup, S.P., Bouten, C.V.C., and Baaijens, F.P.T. Tissue Engineering of Human Heart Valve Leaflets: A Novel Bioreactor for a Strain-Based Conditioning Approach. Annals of Biomedical Engineering **33**, 1778, 2005.

9. Birla, R.K., Borschel, G.H., and Dennis, R.G. In Vivo Conditioning of Tissue-engineered Heart Muscle Improves Contractile Performance. Artificial Organs **29**, 866, 2005.

10. Temple, J.P., Hutton, D.L., Hung, B.P., Huri, P.Y., Cook, C.A., Kondragunta, R., Jia, X., and Grayson, W.L. Engineering anatomically shaped vascularized bone grafts with hASCs and 3D-printed PCL scaffolds. Journal of Biomedical Materials Research Part A **102**, 4317, 2014.

11. Zopf, D.A., Hollister, S.J., Nelson, M.E., Ohye, R.G., and Green, G.E. Bioresorbable Airway Splint Created with a Three-Dimensional Printer. New England Journal of Medicine **368**, 2043, 2013.

12. Nickels, L. World's first patient-specific jaw implant. Metal Powder Report **67**, 12, 2012.

13. Jeffries, E.M., Nakamura, S., Lee, K.-W., Clampffer, J., Ijima, H., and Wang, Y. Micropatterning Electrospun Scaffolds to Create Intrinsic Vascular Networks. Macromolecular Bioscience **14**, 1514, 2014.

14. Xu, W., Wang, X., Yan, Y., and Zhang, R. Rapid Prototyping of Polyurethane for the Creation of Vascular Systems. Journal of Bioactive and Compatible Polymers **23**, 103, 2008

15. Wang, M.O., Vorwald, C.E., Dreher, M.L., Mott, E.J., Cheng, M.-H., Cinar, A., Mehdizadeh, H., Somo, S., Dean, D., Brey, E.M., and Fisher, J.P. Evaluating 3D-Printed Biomaterials as Scaffolds for Vascularized Bone Tissue Engineering. Advanced Materials **27**, 138, 2015.

16. Nguyen, L.H., Annabi, N., Nikkhah, M., Bae, H., Binan, L., Park, S., Kang, Y., Yang, Y., and Khademhosseini, A. Vascularized bone tissue engineering: approaches for potential improvement. Tissue engineering Part B, Reviews **18**, 363, 2012.

17. Visk, D. Will Advances in Preclinical In Vitro Models Lower the Costs of Drug Development? Applied In Vitro Toxicology **1**, 79, 2015.

18. Dababneh, A.B., and Ozbolat, I.T. Bioprinting Technology: A Current State-of-the-Art Review. Journal of Manufacturing Science and Engineering **136**, 061016, 2014.

19. Pham, D.T., and Dimov, S.S. Rapid Manufacturing: The Technologies and Applications of Rapid Prototyping and Rapid Tooling: Springer; 2001.

20. Stratasys, I. Fused Deposition Modelling for Fast, Safe Plastic Models. 12th Annual Conference on Computer Graphics. Chicago1991. pp. 326.

21. Sachs, E.M., Haggerty, J.S., Cima, M.J., and Williams, P.A. Three-dimensional printing techniques. Google Patents; 1993.

22. Atala, A. Tissue engineering of human bladder. British Medical Bulletin **97**, 81, 2011.

23. Murphy, S.V., and Atala, A. 3D bioprinting of tissues and organs. Nature Biotechnology **32**, 773, 2014.

24. Marcus, H., Beaman, J.J., Barlow, J.W., Bourell, D.L., and Crawford, R.H. Solid Freeform Fabrication Proceedings. presented at the" Solid Freeform Fabrication Proceedings, Austin, TX, Year.

25. Aliakbari, M. Additive Manufacturing: State-of-the-Art, Capabilities, and Sample Applications with Cost Analysis [MAsters Production Engineering and Management, Department of Industrial Production,, KTH2012.

26. Mota, C., Puppi, D., Chiellini, F., and Chiellini, E. Additive Manufacturing Techniques for the Production of Tissue Engineering Constructs. J Tissue Eng Regen Med **9**, 174, 2012.

27. Bose, S., Darsell, J., Kintner, M., Hosick, H., and Bandyopadhyay, A. Pore size and pore volume effects on alumina and TCP ceramic scaffolds. Materials Science and Engineering: C **23**, 479, 2003.

28. Lam, C.X.F., Mo, X.M., Teoh, S.H., and Hutmacher, D.W. Scaffold development using 3D printing with a starch-based polymer. Materials Science and Engineering: C **20**, 49, 2002.

29. Suwanprateeb, J. Improvement in mechanical properties of three-dimensional printing parts made from natural polymers reinforced by acrylate resin for biomedical applications: a double infiltration approach. Polymer International **55**, 57, 2006.

30. Giordano, R.A., Wu, B.M., Borland, S.W., Cima, L.G., Sachs, E.M., and Cima, M.J. Mechanical properties of dense polylactic acid structures fabricated by three dimensional printing. Journal of Biomaterials Science, Polymer Edition **8**, 63, 1997.

31. Park, W., and Griffith, L. Integration of surface modification and 3D fabrication techniques to prepare patterned poly(L-lactide) substrates allowing regionally selective cell adhesion. J Biomater Sci Polm Ed **9**, 89, 1998.

32. Gbureck, U., Hölzel, T., Doillon, C.J., Müller, F.A., and Barralet, J.E. Direct Printing of Bioceramic Implants with Spatially Localized Angiogenic Factors. Advanced Materials **19**, 795, 2007.

33. Khalyfa, A., Vogt, S., Weisser, J., Grimm, G., Rechtenbach, A., Meyer, W., and Schnabelrauch, M. Development of a new calcium phosphate powder-binder system for the 3D printing of patient specific implants. J Mater Sci: Mater Med **18**, 909, 2007.

34. Gbureck, U., Vorndran, E., Müller, F.A., and Barralet, J.E. Low temperature direct 3D printed bioceramics and biocomposites as drug release matrices. Journal of Controlled Release **122**, 173, 2007.

35. Will, J., Melcher, R., Treul, C., Travitzky, N., Kneser, U., Polykandriotis, E., Horch, R., and Greil, P. Porous ceramic bone scaffolds for vascularized bone tissue regeneration. Journal of Materials Science: Materials in Medicine **19**, 2781, 2008.

36. Shanjani, Y., De Croos, J.N.A., Pilliar, R.M., Kandel, R.A., and Toyserkani, E. Solid freeform fabrication and characterization of porous calcium polyphosphate structures for tissue engineering purposes. Journal of Biomedical Materials Research Part B: Applied Biomaterials **93B**, 510, 2010.

37. Compton, B., and Lewis, J.A. 3D-Printing of Lightweight Cellular Composites. Advanced Materials **26**, 5930, 2014.

38. Lewis, J.A. Direct Ink Writing of 3D Functional Materials. Advanced Functional Materials **16**, 2193, 2006.

39. Tarafder, S., Balla, V.K., Davies, N.M., Bandyopadhyay, A., and Bose, S. Microwave-sintered 3D printed tricalcium phosphate scaffolds for bone tissue engineering. Journal of Tissue Engineering and Regenerative Medicine **7**, 631, 2013.

40. Zein, I., Hutmacher, D.W., Tan, K.C., and Teoh, S.H. Fused deposition modeling of novel scaffold architectures for tissue engineering applications. Biomaterials **23**, 1169, 2002.

41. Landers, R., Hübner, U., Schmelzeisen, R., and Mülhaupt, R. Rapid prototyping of scaffolds derived from thermoreversible hydrogels and tailored for applications in tissue engineering. Biomaterials **23**, 4437, 2002.

42. Landers, R., and Mülhaupt, R. Desktop manufacturing of complex objects, prototypes and biomedical scaffolds by means of computer-assisted design combined with computer-guided 3D plotting of polymers and reactive oligomers. Macromolecular Materials and Engineering **282**, 17, 2000.

43. Gibson, I., Rosen, D.W., and Stucker, B. Additive manufacturing technologies: Springer; 2010.

44. Mota, C., Puppi, D., Chiellini, F., and Chiellini, F. Additive manufacturing techniques for the production of tissue engineering constructs. Tissue Engineering and Regenerative Medicine 2012.

45. Melchels, F.P.W., Feijen, J., and Grijpma, D.W. A poly(d,l-lactide) resin for the preparation of tissue engineering scaffolds by stereolithography. Biomaterials **30**, 3801, 2009.

46. Yang, S., Leong, K.-F., Du, Z., and Chau, C.-K.C. The Design of Scaffolds for Use in Tissue Engineering. Part II. Rapid Prototyping Techniques. TISSUE ENGINEERING **8**, 1, 2002.

47. Cooke, M.N., Fisher, J.P., Dean, D., Rimnac, C., and Mikos, A.G. Use of stereolithography to manufacture critical-sized 3D biodegradable scaffolds for bone ingrowth. Journal of Biomedical Materials Research Part B: Applied Biomaterials **64B**, 65, 2003.

48. Moglia, R.S., Holm, J.L., Sears, N.A., Wilson, C.J., Harrison, D.M., and Cosgriff-Hernandez, E. Injectable PolyHIPEs as High-Porosity Bone Grafts. Biomacromolecules **12**, 3621, 2011.

49. Christenson, E.M., Soofi, W., Holm, J.L., Cameron, N.R., and Mikos, A.G. Biodegradable fumarate-based polyHIPEs as tissue engineering scaffolds. Biomacromolecules **8**, 3806, 2007.

50. Langton, C.M., Whitehead, M.A., Langton, D.K., and Langley, G. Development of a cancellous bone structural model by stereolithography for ultrasound characterisation of the calcaneus. Medical Engineering & Physics **19**, 599, 1997.

51. Leukers, B., Gülkan, H., Irsen, S., Milz, S., Tille, C., Schieker, M., and Seitz, H. Hydroxyapatite scaffolds for bone tissue engineering made by 3D printing. J Mater Sci: Mater Med **16**, 1121, 2005.

52. Yang, S., Leong, KF, Du, Z. Chua, C-K. The Design of Scaffolds for Use in Tissue Engineering. Part I. Traditional Factors. Tissue Engineering **7**, 679, 2001.

53. Yu, T., and Ober, C.K. Methods for the Topographical Patterning and Patterned Surface Modification of Hydrogels Based on Hydroxyethyl Methacrylate. Biomacromolecules **4**, 1126, 2003.

54. Matsuda, T., and Magoshi, T. Preparation of Vinylated Polysaccharides and Photofabrication of Tubular Scaffolds as Potential Use in Tissue Engineering. Biomacromolecules **3**, 942, 2002.

55. Chu, T.M.G., Hollister, S.J., Halloran, J.W., Feinberg, S.E., and Orton, D.G. Manufacturing and Characterization of 3-D Hydroxyapatite Bone Tissue Engineering Scaffolds. Annals of the New York Academy of Sciences **961**, 114, 2002.

56. Chu, T.M.G., Orton, D.G., Hollister, S.J., Feinberg, S.E., and Halloran, J.W. Mechanical and in vivo performance of hydroxyapatite implants with controlled architectures. Biomaterials **23**, 1283, 2002.

57. Bártolo, P. Stereolithographic Processes. In: Bártolo P.J., ed. Stereolithography: Springer US; 2011. pp. 1.

58. Zhou, C., Chen, Y., Yang, Z., and Khoshnevis, B. Digital material fabrication using mask-image-projection-based stereolithography. Rapid Prototyping Journal **19**, 153, 2013.

59. Yang, S., Leong, K.-f., Du, Z., and Chua, C.-k. The Design of Scaffolds for Use in Tissue Engineering. Part II. Rapid Prototyping Techniques. Tissue Engineering **8**, 1, 2002.

60. Shuai, C., Li, P., Liu, J., and Peng, S. Optimization of TCP/HAP ratio for better properties of calcium phosphate scaffold via selective laser sintering. Materials Characterization **77**, 23, 2013.

61. Leong, K.F., Cheah, C.M., and Chua, C.K. Solid freeform fabrication of three-dimensional scaffolds for engineering replacement tissues and organs. Biomaterials **24**, 2363, 2003.

62. Simpson, R.L., Wiria, F.E., Amis, A.A., Chua, C.K., Leong, K.F., Hansen, U.N., Chandrasekaran, M., and Lee, M.W. Development of a 95/5 poly(L-lactide-co-glycolide)/hydroxylapatite and beta-tricalcium phosphate scaffold as bone replacement material via selective laser sintering. Journal of biomedical materials research Part B, Applied biomaterials **84**, 17, 2008.

63. Zeltinger, J., Sherwood, J.K., Graham, D.A., Müeller, R., and Griffith, L.G. Effect of Pore Size and Void Fraction on Cellular Adhesion, Proliferation, and Matrix Deposition. Tissue engineering **5**2001.

64. Bose, S., Vahabzadeh, S., and Bandyopadhyay, A. Bone Tissue Engineering Using 3D Printing. Materials Today **16**, 496, 2013.

65. Duan, B., and Wang, M. Customized Ca-P/PHBV nanocomposite scaffolds for bone tissue engineering: design, fabrication, surface modification and sustained release of growth factor. Journal of the Royal Society, Interface / the Royal Society **7 Suppl 5**, S615, 2010.

66. Kundu, J., Shim, J.H., Jang, J., Kim, S.W., and Cho, D.W. An additive manufacturing-based PCL-alginate-chondrocyte bioprinted scaffold for cartilage tissue engineering. J Tissue Eng Regen Med 2013.

67. Hong, S., Sycks, D., Chan, H.F., Lin, S., Lopez, G.P., Guilak, F., Leong, K.W., and Zhao, X. 3D Printing of Highly Stretchable and Tough Hydrogels into Complex, Cellularized Structures. Advanced Materials **27**, 4035, 2015.

68. Ozbolat, I., and Yu, Y. Bioprinting Towards Organ Fabrication: Challenged and Future Trends. Transactions on Biomedical Engineering, 1, 2012.

69. Kolesky, D., Truby, R., Gladman, S., Busbee, T., Homan, K., and Lewis, J.A. 3D Bioprinting of Vascularized, Heterogeneous Cell-Laden Tissue Constructs. Advanced Materials **26**, 3124, 2014.

70. Wu, W., DeConinck, A., and Lewis, J.A. Omnidirectional Printing of 3D Microvascular Networks. Advanced Materials2011. pp. H178.

71. Jakab, K., Norotte, C., Marga, F., Murphy, K., Vunjak-Novakovic, G., and Forgacs, G. Tissue engineering by self-assembly and bio-printing of living cells. Biofabrication **2**, 022001, 2010.

72. Khalil, S., Nam, J., and Sun, W. Multi-nozzle deposition for construction of 3D biopolymer tissue scaffolds. Rapid Prototyping **11**, 9, 2005.

73. Fedorovich, N.E., De Wijn, J.R., Verbout, A.J., Alblas, J., and Dhert, W.J.A. Three-Dimensional Fiber Deposition of Cell-Laden, Viable, Patterned Constructs for Bone Tissue Printing. Tissue Engineering Part A **14**, 127, 2008.

74. Billiet, T., Gevaert, E., De Schryver, T., Cornelissen, M., and Dubruel, P. The 3D printing of gelatin methacrylamide cell-laden tissue-engineered constructs with high cell viability. Biomaterials **35**, 49, 2014.

75. Smith, C.M., Christian, J.J., Warren, W.L., and Williams, S.K. Characterizing environmental factors that impact the viability of tissue-engineered constructs fabricated by a direct-write bioassembly tool. Tissue Eng **13**, 373, 2007.

76. Smith, C.M., Stone, A.L., Parkhill, R.L., Stewart, R.L., Simpkins, M.W., Kachurin, A.M., Warren, W.L., and Williams, S.K. Three-Dimensional BioAssembly Tool for Generating Viable Tissue-Engineered Constructs. Tissue Engineering **10**, 1566, 2004.

77. Pati, F., Jang, J., Ha, D.-H., Won Kim, S., Rhie, J.-W., Shim, J.-H., Kim, D.-H., and Cho, D.-W. Printing three-dimensional tissue analogues with decellularized extracellular matrix bioink. Nat Commun **5**2014.

78. Campos, D.F.D., Drescher, W., Rath, B., Tingart, M., and Fischer, H. Supporting Biomaterials for Articular Cartilage Repair. Cartilage **3**2012.

79. Miller, J.S. The Billion Cell Construct: Will Three-Dimensional Printing Get Us There? PLOS Biology **12**2014.

80. Guillotin, B., and Guillemot, F. Cell patterning technologies for organotypic tissue fabrication. Trends in Biotechnology **29**, 183, 2011.

81. Irvine, S.A., Agrawal, A., Lee, B.H., Chua, H.Y., Low, K.Y., Lau, B.C., Machluf, M., and Venkatraman, S. Printing cell-laden gelatin constructs by free-form fabrication and enzymatic protein crosslinking. Biomedical Microdevices **17**, 16, 2015.

82. Boland, T., Xu, T., Damon, B., and Cui, X. Application of Inket Printing to Tissue Engineering. **Biotechnology**, 910, 2006.

83. Wüst, S., Müller, R., and Hofmann, S. Controlled Positioning of Cells in Biomaterials—Approaches Towards 3D Tissue Printing. Journal of Functional Biomaterials **2**, 119, 2011.

84. Fedorovich, N.E., Alblas, J., de Wijn, J.R., Hennink, W.E., Verbout, A.J., and Dhert, W.J.A. Hydrogels as Extracellular Matrices for Skeletal Tissue Engineering: State-of-the-Art and Novel Application in Organ Printing. Tissue engineering **13**, 1905, 2007.

85. O'Brien, C.M., Holmes, B., Faucett, S., and Zhang, L.G. Three-dimensional printing of nanomaterial scaffolds for complex tissue regeneration. Tissue engineering Part B, Reviews **21**, 103, 2015.

86. Devillard, R., Pages, E., Correa, M.M., Keriquel, V., Remy, M., Kalisky, J., Ali, M., Guillotin, B., and Guillemot, F. Cell Patterning by Laser-Assisted Bioprinting. Methods in Cell Biology **119**, 159, 2014.

87. Wang, X., Tuomi, J., Mäkitie, A., Paloheimo, K.-S., Partanen, J., and Yliperttula, M. The Integrations of Biomaterials and Rapid Prototyping Techniques for Intelligent Manufacturing of Complex Organs. Advances in Biomaterials Science and Biomedical Applications2013.

88. Guillemot, F., Souquet, A., Catros, S., Guillotin, B., Lopez, J., Faucon, M., Pippenger, B., Bareille, R., Rémy, M., Bellance, S., Chabassier, P., Fricain, J.C.,

and Amédée, J. High-throughput laser printing of cells and biomaterials for tissue engineering. Acta Biomaterialia **6**, 2494, 2010.

89. Guillotin, B., Souquet, A., Catros, S., Duocastella, M., Pippenger, B., Bellance, S., Bareille, R., Rémy, M., Bordenave, L., Amédée, J., and Guillemot, F. Laser assisted bioprinting of engineered tissue with high cell density and microscale organization. Biomaterials **31**, 7250, 2010.

90. Odde, D.J., and Renn, M.J. Laser-guided direct writing for applications in biotechnology. Nanotechnology **17**, 385, 1999.

91. Wang, W., Li, G., and Huang, Y. Modeling of Bubble Expansion-Induced Cell Mechanical Profile in Laser-Assisted Cell Direct Writing. Journal of Manufacturing Science and Engineering **131**2009.

92. Gaebel, R., Ma, N., Liu, J., Guan, J., Koch, L., Klopsch, C., Gruene, M., Toelk, A., Wang, W., Mark, P., Wang, F., Chichkov, B., Li, W., andS teinhoff, G. Patterning human stem cells and endothelial cells with laser printing for cardiac regeneration. Biomaterials **32**, 9218, 2011.

93. Koch, L., Deiwick, A., Schlie, S., Michael, S., Gruene, M., Coger, V., Zychlinski, D., Schambach, A., Reimers, K., Vogt, P.M., and Chichkov, B. Skin tissue generation by laser cell printing. Biotechnology and Bioengineering **109**, 1855, 2012.

94. Koch, L., Kuhn, S., Sorg, H., Gruene, M., Schlie, S., Gaebel, R., Polchow, B., Reimers, K., Stoelting, S., Ma, N., Vogt, P.M., Steinhoff, G., and Chichkov, B. Laser Printing of Skin Cells and Human Stem Cells. Tissue Engineering Part C **16**, 847, 2010.

95. Michael, S., Sorg, H., Peck, C.-T., Koch, L., Deiwick, A., Chichkov, B., Vogt, P.M., and Reimers, K. Tissue Engineered Skin Substitutes Created by Laser-Assisted Bioprinting Form Skin-Like Structures in the Dorsal Skin Fold Chamber in Mice. PLoS ONE **8**, e57741, 2013.

96. Schiele, N., Koppes, R.A., Corr, D.T., Ellison, K.S., Thompson, D.M., Ligon, L.A., Lippert, T.K.M., and Chrisey, D.B. Laser direct writing of combinatorial libraries of idealized cellular constructs: Biomedical applications. Applied Surface Science **255**, 5444, 2009.

97. Gudapati, H., Yan, J., Huang, Y., and Chrisey, D.B. Alginate gelation-induced cell death during laser-assisted cell printing. Biofabrication **6**, 1, 2014.

98. Murphy, S.V., Skardal, A., and Atala, A. Evaluation of hydrogels for bio-printing applications. Journal of Biomedical Materials Research Part A **101A**, 272, 2013.

99. Bae, H., Chu, H., Edalat, F., Cha, J.M., Sant, S., Kashyap, A., Ahari, A.F., Kwon, C.H., Nichol, J.W., Manoucheri, S., Zamanian, B., Wang, Y., and Khademhosseini, A. Development of functional biomaterials with micro- and nanoscale technologies for tissue engineering and drug delivery applications. Journal of Tissue Engineering and Regenerative Medicine **8**, 1, 2014.

100. Bertassoni, L.E., Cardoso, J.C., Manoharan, V., Cristino, A.L., Bhise, N.S., Araujo, W.A., Zorlutuna, P., Vrana, N.E., Ghaemmaghami, A.M., Dokmeci, M.R., and Khademhosseini, A. Direct-write Bioprinting of Cell-laden Methacrylated Gelatin Hydrogels. Biofabrication **6**, 024105, 2014.

101. Nichol, J.W., Koshy, S.T., Bae, H., Hwang, C.M., Yamanlar, S., and Khademhosseini, A. Cell-laden microengineered gelatin methacrylate hydrogels. Biomaterials **31**, 5536, 2010.

102. Trachtenberg, J.E., Mountziaris, P.M., Miller, J.S., Wettergreen, M., Kasper, F.K., and Mikos, A.G. Open-source three-dimensional printing of biodegradable polymer scaffolds for tissue engineering. Journal of Biomedical Materials Research Part A **102**, 4326, 2014.

103. Boland, T., Mironov, V., Gutowska, A., Roth, E., and Markwald, R. Cell and Organ Printing 2: Fusion of Cell Aggregates in Three-Dimensional Gels. The Anotomical Record Part A **272A**, 497, 2003.

104. Chang, C.C., Boland, E.D., Williams, S.K., and Hoying, J.B. Direct-write bioprinting three-dimensional biohybrid systems for future regenerative therapies. Journal of Biomedical Materials Research Part B: Applied Biomaterials **98B**, 160, 2011.

105. Mironov, V., Boland, T., Trusk, T., Forgacs, G., and Markwal, R.R. Organ printing: compu.ter-aided jet-based 3D tissue engineering. TRENDS in Biotechnology **21**, 157, 2003.

106. Xu, T., Gregory, C.A., Molnar, P., Cui, X., Jalota, S., Bhaduri, S.B., and Boland, T. Viability and electrophysiology of neural cell structures generated by the inkjet printing method. Biomaterials **27**, 3580, 2006.

107. Xu, T., Jin, J., Gregory, C., Hickman, J.J., and Boland, T. Inkjet printing of viable mammalian cells. Biomaterials **26**, 93, 2005.

108. Fedorovich, N., Dewijn, J., Verbout, A., Alblas, J., and Dhert, W.J.A. Three-Dimensional Fiber Deposition of Cell-Laden, Viable, Patterned Constructs for Bone Tissue Printing. Tissue engineering: Part A **14**, 127, 2008.

109. Lorber, B., W.K., H., Hutchings, I.M., and Martin, K.R. Adult rat retinal ganglion cells and glia can be printed by piezoelectric inkjet printing. Biofabrication **6**, 9, 2014.

110. Visconti, R.P., Ebihara, Y., LaRue, A.C., Fleming, P.A., McQuinn, T.C., Masuya, M., Minamiguchi, H., Markwald, R.R., Ogawa, M., and Drake, C.J. An in vivo analysis of hematopoietic stem cell potential: hematopoietic origin of cardiac valve interstitial cells. Circulation Research **98**, 690, 2006.

111. Kim, S.S., Utsunomiya, H., Koski, J.A., Wu, B.M., Cima, M.J., Sohn, J., Mukai, K., Griffith, L.G., and Vacanti, J.P. Survival and function of hepatocytes on a novel three-dimensional synthetic biodegradable polymer scaffold with an intrinsic network of channels. Annals of Surgery **228**, 8, 1998.

112. Muth, J., Vogt, D., Truby, R., Mengüç, Y., Kolesky, D., Wood, R., and Lewis, J.A. Embedded 3D Printing of Strain Sensors within Highly Stretchable Elastomers. Advanced Materials **26**, 6307, 2014.

113. Osterbur, L.W. 3d Printing of Hyaluronic Acid Scaffolds for Tissue Engineering Applications Masters of Science]. Materials Science and Engineering, University of Illinois at Urbana-Champaign2013.

114. Schuurman, W., Khristov, V., Pot, M.W., van Weeren, P.R., Dhert, W.J., and Malda, J. Bioprinting of hybrid tissue constructs with tailorable mechanical properties. Biofabrication **3**, 021001, 2011.

115. Schuurman, W., Levett, P., Pot, M., van Weeren, P., Dhert, W., Hutmacher, D., Melchels, F., Klein, T., and Malda, J. Gelatin-Methacrylamide Hydrogels as Potential Biomaterials for Fabrication of Tissue-Engineered Cartilage Constructs. Macromolecular Biosciences **13**, 561, 2013.

116. Skardal, A. Hyaluronan and Gelatin Biomaterials For Bioprinting Engineered Tissues [Doctor of Philosophy Bioengineering, The University of Utah2010.

117. Skardal, A., Zhang, J., McCoard, L., Xu, X., Oottamasathien, S., and Prestwich, G.D. Photocrosslinkable Hyaluronan-Gelatin Hydrogels for Two-Step Bioprinting. Tissue engineering **16**, 2675, 2010.

118. Chen, A.A., Tsang, V.L., Albrecht, D.R., and Bhatia, S.N. Ch. 2: 3-D Fabrication Technology for Tissue Engineering. BioMEMS and Biomedical Nanotechnology: springer; 2007. pp. 23.

119. Chen, C.S., Mrksich, M., Huang, S., Whitesides, G.M., and Ingber, D.E. Geometric Control of Cell Life and Death. Science **276**, 1425, 1997.

120. Chen, H., and Ozbolat, I.T. A Multi-Material Bioprinting Platform towards Stratified Articular Cartilage Tissue Fabrication. presented at the" Industrial and Systems Engineering Research Conference, Puerto Rico, Year.

121. Wang, X., Yan, Y., Pan, Y., Xiong, Z., Liu, H., Cheng, J., Liu, F., Lin, F., Wu, R., Zhang, R., and Lu, Q. Generation of Three-Dimensional Hepatocyte/Gelatin Structures with Rapid Prototyping System. Tissue engineering **12**, 83, 2006.

122. Hopp, B., Smausz, T., Szabó, G., Kolozsvári, L., Kafetzopoulos, D., Fotakis, C., and Nógrádi, A. Femtosecond laser printing of living cells using absorbing film-assisted laser-induced forward transfer. OPTICE **51**, 014302, 2012.

123. Riggs, B.C., Dias, A.D., Schiele, N.R., Cristescu, R., Huang, Y., Corr, D.T., and Chrisey, D.B. Matrix-assisted pulsed laser methods for biofabrication. MRS Bulletin **36**, 1043, 2011.

124. Billiet, T., Gevaert, E., De Schryvwer, T., and Cornerlson, M. The 3D printing of gelatin methacrylamide cell-laden tissue-engineered constructs with high cell viability. Biomaterials **35**, 49, 2014.

125. Kesti, M., Muller, M., Becher, J., Schnabelrauch, M., D'Este, M., Eglin, D., and Zenobi-Wong, M. A versatile bioink for three-dimensional printing of cellular scaffolds based on thermally and photo-triggered tandem gelation. Acta Biomater **11**, 162, 2015.

126. Phillippi, J.A., Miller, E., Weiss, L., Huard, J., Waggoner, A., and Campbell, P. Microenvironments Engineered by Inkjet Bioprinting Spatially Direct Adult Stem Cells Toward Muscle- and Bone-Like Subpopulations. STEM CELLS **26**, 127, 2008.

127. Ker, D.F.E., Chu, B., Phillippi, J.A., Gharaibeh, B., Huard, J., Weiss, L.E., and Campbell, P.G. Engineering Spatial Control of Multiple Differentiation Fates within a Stem Cell Population. Biomaterials **32**, 3413, 2011.

128. Cooper, G.M., Miller, E.D., Decesare, G.E., Usas, A., Lensie, E.L., Bykowski, M.R., Huard, J., Weiss, L.E., Losee, J.E., and Campbell, P.G. Inkjet-based biopatterning of bone morphogenetic protein-2 to spatially control calvarial bone formation. Tissue Eng Part A **16**, 1749, 2010.

129. Hennink, W.E., and van Nostrum, C.F. Novel crosslinking methods to design hydrogels. Advanced Drug Delivery Reviews **54**, 13, 2002.

130. Choi, R.S., and Vacanti, J.P. Preliminary studies of tissue-engineered intestine using isolated epithelial organoid units on tubular synthetic biodegradable scaffolds. Transplantation proceedings **29**, 848, 1997.

131. Christman, K.L., Vardanian, A.J., Fang, Q., Sievers, R.E., Fok, H.H., and Lee, R.J. Injectable Fibrin Scaffold Improves Cell Transplant Survival, Reduces Infarct Expansion, and Induces Neovasculature Formation in Ischemic Myocardium. Journal of the American College of Cardiology **44**, 654, 2004.

132. Atala, A., Bauer, S.B., Soker, S., Yoo, J.J., and Retik, A.B. Tissue-engineered autologous bladders for patients needing cystoplasty. The Lancet **367**, 1241, 2006.

133. Low, K.H., Leong, K.F., Chua, C.K., Du, Z.H., and Cheah, C.M. Characterization of SLS parts for drug delivery devicesnull. Rapid Prototyping Journal **7**, 262, 2001.

134. Figallo, E., Cannizzaro, C., Gerecht, S., Burdick, J.A., Langer, R., Elvassore, N., and Vunjak-Novakovic, G. Micro-bioreactor array for controlling cellular microenvironments. Lab Chip **7**, 710, 2007.

135. Vunjak-Novakovic, G., Bhatia, S., Chen, C., and Hirschi, K. HeLiVa platform: integrated heart-liver-vascular systems for drug testing in human health and disease. Stem Cell Research & Therapy **4**, S8, 2013.

136. Nair, K., Gandhi, M., Khalil, S., Yan, K.C., Marcolongo, M., Barbee, K., and Sun, W. Characterization of cell viability during bioprinting processes. Biotechnology Journal **4**, 1168, 2009.

137. Cunningham, L.P., Veilleux, M.P., and Campagnola, P.J. Freeform multiphoton excited microfabrication for biological applications using a rapid prototyping CAD-based approach. Optics express **14**, 8613, 2006.

138. Kabouraki, E., Giakoumaki, A.N., Danilevicius, P., Gray, D., Vamvakaki, M., and Farsari, M. Redox multiphoton polymerization for 3D nanofabrication. Nano letters **13**, 3831, 2013.

139. Maria, F., Maria, V., and Boris, N.C. Multiphoton polymerization of hybrid materials. Journal of Optics **12**, 124001, 2010.

140. Li, L., and Fourkas, J.T. Multiphoton polymerization. Materials Today **10**, 30, 2007.

141. Cameron, N.R., Krajnc, P., and Silverstein, M.S. Colloidal Templating. Porous Polymers: John Wiley & Sons, Inc.; 2011. pp. 119.

142. Kimmins, S.D., and Cameron, N.R. Functional porous polymers by emulsion templating: recent advances. Advanced Functional Materials **21**, 211, 2011.

143. Pulko, I., and Krajnc, P. High Internal Phase Emulsion Templating – A Path To Hierarchically Porous Functional Polymers. Macromolecular Rapid Communications **33**, 1731, 2012.

144. Wong, L.L.C., Ikem, V.O., Menner, A., and Bismarck, A. Macroporous Polymers with Hierarchical Pore Structure from Emulsion Templates Stabilised by Both Particles and Surfactants. Macromolecular Rapid Communications **32**, 1563, 2011.

145. Carn, F., Colin, A., Achard, M.-F., Deleuze, H., Sellier, E., Birot, M., and Backov, R. Inorganic monoliths hierarchically textured via concentrated direct emulsion and micellar templates. Journal of Materials Chemistry **14**, 1370, 2004.

146. Li, Z., Xiao, M., Wang, J., and Ngai, T. Pure protein scaffolds from pickering high internal phase emulsion template. Macromol Rapid Commun **34**, 169, 2013.

147. Zhang, H., and Cooper, A.I. Emulsion-Templated Hierarchically Porous Silica Beads Using Silica Nanoparticles as Building Blocks. Industrial & Engineering Chemistry Research **44**, 8707, 2005.

148. Moglia, R., Whitely, M., Brooks, M., Robinson, J., Pishko, M., and Cosgriff-Hernandez, E. Solvent-Free Fabrication of polyHIPE Microspheres for Controlled Release of Growth Factors. Macromolecular Rapid Communications **35**, 1301, 2014.

149. Kovačič, S., Kren, H., Krajnc, P., Koller, S., and Slugovc, C. The Use of an Emulsion Templated Microcellular Poly(dicyclopentadiene-co-norbornene) Membrane as a Separator in Lithium-Ion Batteries. Macromolecular Rapid Communications **34**, 581, 2013.

150. Shirshova, N., Johansson, P., Marczewski, M.J., Kot, E., Ensling, D., Bismarck, A., and Steinke, J.H.G. Polymerised high internal phase ionic liquid-in-oil emulsions as potential separators for lithium ion batteries. Journal of Materials Chemistry A **1**, 9612, 2013.

151. Pulko, I., Wall, J., Krajnc, P., and Cameron, N.R. Ultra-High Surface Area Functional Porous Polymers by Emulsion Templating and Hypercrosslinking: Efficient Nucleophilic Catalyst Supports. Chemistry – A European Journal **16**, 2350, 2010.

152. Carty, W.M., and Lednor, P.W. Monolithic ceramics and heterogeneous catalysts: honeycombs and foams. Current Opinion in Solid State and Materials Science **1**, 88, 1996.

153. Silverstein, M.S. PolyHIPEs: Recent advances in emulsion-templated porous polymers. Progress in Polymer Science **39**, 199, 2014.

154. Susec, M., Ligon, S.C., Stampfl, J., Liska, R., and Krajnc, P. Hierarchically Porous Materials from Layer-by-Layer Photopolymerization of High Internal Phase Emulsions. Macromolecular Rapid Communications **34**, 938, 2013.

155. Zhang, H., Hardy, G.C., Khimyak, Y.Z., Rosseinsky, M.J., and Cooper, A.I. Synthesis of Hierarchically Porous Silica and Metal Oxide Beads Using Emulsion-Templated Polymer Scaffolds. Chemistry of Materials **16**, 4245, 2004.

156. Martins, A., Chung, S., Pedro, A.J., Sousa, R.A., Marques, A.P., Reis, R.L., and Neves, N.M. Hierarchical starch-based fibrous scaffold for bone tissue engineering applications. Journal of Tissue Engineering and Regenerative Medicine **3**, 37, 2009.

157. Hollister, S.J. Porous scaffold design for tissue engineering. Nat Mater **4**, 518, 2005.

158. Johnson, D.W., Sherborne, C., Didsbury, M.P., Pateman, C., Cameron, N.R., and Claeyssens, F. Macrostructuring of Emulsion-templated Porous Polymers by 3D Laser Patterning. Advanced Materials **25**, 3178, 2013.

159. Owen, R., Sherborne, C., Paterson, T., Green, N.H., Reilly, G.C., and Claeyssens, F. Emulsion templated scaffolds with tunable mechanical properties for bone tissue engineering. Journal of the mechanical behavior of biomedical materials **54**, 159, 2015.

160. Welch, C.F., Rose, G.D., Malotky, D., andE ckersley, S.T. Rheology of High Internal Phase Emulsions. Langmuir **22**, 1544, 2006.

161. Kim, G.D., and Oh, Y.T. A benchmark study on rapid prototyping processes and machines: Quantitative comparisons of mechanical properties, accuracy, roughness, speed, and material cost. Proceedings of the Institution of Mechanical Engineers, Part B: Journal of Engineering Manufacture **222**, 201, 2008.

162. Markstedt, K., Mantas, A., Tournier, I., Martinez Avila, H., Hagg, D., and Gatenholm, P. 3D Bioprinting Human Chondrocytes with Nanocellulose-Alginate Bioink for Cartilage Tissue Engineering Applications. Biomacromolecules **16**, 1489, 2015.

163. Atala, A., and Murphy, S. 3D bioprinting of tissues and organs. Nature Biotechnology **32**, 773, 2014.

164. Melchels, F.P.W., Domingos, M.A.N., Klein, T.J., Malda, J., Bartolo, P.J., and Hutmacher, D.W. Additive manufacturing of tissues and organs. Progress in Polymer Science **37**, 1079, 2012.

165. Karoly, J., Cyrille, N., Francoise, M., Keith, M., Gordana, V.-N., and Gabor, F. Tissue engineering by self-assembly and bio-printing of living cells. Biofabrication **2**, 022001, 2010.

166. Wang, A.-j., Paterson, T., Owen, R., Sherborne, C., Dugan, J., Li, J.-m., and Claeyssens, F. Photocurable high internal phase emulsions (HIPEs) containing hydroxyapatite for additive manufacture of tissue engineering scaffolds with multi-scale porosity. Materials Science and Engineering: C **67**, 51, 2016.

167. Seyed Farid Seyed, S., Samira, G., Mehdi, M., Hooman, Y., Hendrik Simon Cornelis, M., Nahrizul Adib, K., and Noor Azuan Abu, O. A review on powder-based additive manufacturing for tissue engineering: selective laser sintering and inkjet 3D printing. Science and Technology of Advanced Materials **16**, 033502, 2015.

168. Ozbolat, I.T., and Hospodiuk, M. Current advances and future perspectives in extrusion-based bioprinting. Biomaterials **76**, 321, 2016.

169. Sears, N.A., Dhavalikar, P.S., and Cosgriff-Hernandez, E.M. Emulsion Inks for 3D Printing of High Porosity Materials. Macromolecular Rapid Communications, n/a, 2016.

170. Chia, H.N., and Wu, B.M. Recent advances in 3D printing of biomaterials. Journal of Biological Engineering **9**, 4, 2015.

171. Mistry, A.S., Pham, Q.P., Schouten, C., Yeh, T., Christenson, E.M., Mikos, A.G., and Jansen, J.A. In vivo bone biocompatibility and degradation of porous fumarate-based polymer/alumoxane nanocomposites for bone tissue engineering. J Biomed Mater Res A **92**, 451, 2010.

172. Peter, S.J., Lu, L., Kim, D.J., and Mikos, A.G. Marrow stromal osteoblast function on a poly(propylene fumarate)/β-tricalcium phosphate biodegradable orthopaedic composite. Biomaterials **21**, 1207, 2000.

173. Peter, S.J., Miller, S.T., Zhu, G., Yasko, A.W., and Mikos, A.G. In vivo degradation of a poly(propylene fumarate)/β-tricalcium phosphate injectable composite scaffold. Journal of Biomedical Materials Research **41**, 1, 1998.

174. Robinson, J., Moglia, R., Stuebben, M., McEnery, M.A.P., and Cosgriff-Hernandez, E. Achieving Interconnected Pore Architecture in Injectable PolyHIPEs for Bone Tissue Engineering. Tissue engineering Part A **20**, 1103, 2014.

175. Moglia, R.S., Whitely, M., Dhavalikar, P., Robinson, J., Pearce, H., Brooks, M., Stuebben, M., Cordner, N., and Cosgriff-Hernandez, E. Injectable Polymerized High Internal Phase Emulsions with Rapid in Situ Curing. Biomacromolecules **15**, 2870, 2014.

176. Sears, N.A., Dhavalikar, P.S., and Cosgriff-Hernandez, E.M. Emulsion Inks for 3D Printing of High Porosity Materials. Macromol Rapid Commun **37**, 1369, 2016.

177. Sears, N.A., Dhavalikar, P.S., and Cosgriff-Hernandez, E.M. Emulsion Inks for 3D Printing of High Porosity Materials. Macromolecular Rapid Communications **37**, 1369, 2016.

178. Muschenborn, A.D., Ortega, J.M., Szafron, J.M., Szafron, D.J., and Maitland, D.J. Porous media properties of reticulated shape memory polymer foams and mock embolic coils for aneurysm treatment. Biomed Eng Online **12**, 103, 2013.

179. Gregory, T.R. Nucleotypic effects without nuclei: genome size and erythrocyte size in mammals. Genome **43**, 895, 2000.

180. Mistry, A.S., Cheng, S.H., Yeh, T., Christenson, E., Jansen, J.A., and Mikos, A.G. Fabrication and in vitro degradation of porous fumarate-based polymer/alumoxane nanocomposite scaffolds for bone tissue engineering. Journal of biomedical materials research Part A **89A**, 68, 2009.

181. Shi, X.e.a. Fabrication of porous ultra-short single-walled carbon nanotube nanocomposite scaffolds for bone tissue engineering. Biomaterials **28**, 4078, 2007.

182. Mistry, A., Pham, Q., Schouten, C., Yeh, T., Christensen, E., Mikos, A., and Jansen, J. *In vivo* bone biocompatibility and degradation of porous fumarate-based polymer/alumoxane nanocomposites for bone tissue engineering. Journal of biomedical materials research Part A **92A**, 451, 2010.

183. Moglia, R.S.e.a. Injectable polyHIPEs with rapid in situ curing. Biomacromolecules **In press** 2014.

184. Polak, S.J., Rustom, L.E., Genin, G.M., Talcott, M., and Wagoner Johnson, A.J. A mechanism for effective cell-seeding in rigid, microporous substrates. Acta Biomater **9**, 7977, 2013.

185. Lewandrowski, K.U., Gresser, J.D., Bondre, S., Silva, A.E., Wise, D.L., and Trantolo, D.J. Developing porosity of poly(propylene glycol-co-fumaric acid) bone graft substitutes and the effect on osteointegration: a preliminary histology study in rats. Journal Of Biomaterials Science Polymer Edition **11**, 879, 2000.

186. Takahashi, Y., and Tabata, Y. Effect of the fiber diameter and porosity of non-woven PET fabrics on the osteogenic differentiation of mesenchymal stem cells. J Biomater Sci-Polym Ed **15**, 41, 2004.

187. Kuboki, Y., Jin, Q., Kikuchi, M., Mamood, J., and Takita, H. Geometry of Artificial ECM: Sizes of Pores Controlling Phenotype Expression in BMP-Induced Osteogenesis and Chondrogenesis. Connective Tissue Research **43**, 529, 2002.

188. Jin, Q.M., Takita, H., Kohgo, T., Atsumi, K., Itoh, H., and Kuboki, Y. Effects of geometry of hydroxyapatite as a cell substratum in BMP-induced ectopic bone formation. Journal of Biomedical Materials Research **52**, 841, 2000.

189. Liu, L.-S., Thompson, A.Y., Heidaran, M.A., Poser, J.W., and Spiro, R.C. An osteoconductive collagen/hyaluronate matrix for bone regeneration. Biomaterials **20**, 1097, 1999.

190. Tsuruga, E., Takita, H., Itoh, H., Wakisaka, Y., and Kuboki, Y. Pore size of porous hydroxyapatite as the cell-substratum controls BMP-induced osteogenesis. Journal of biochemistry **121**, 317, 1997.

191. Kuboki, Y., Jin, Q., and Takita, H. Geometry of carriers controlling phenotypic expression in BMP-induced osteogenesis and chondrogenesis. The Journal Of Bone And Joint Surgery American Volume **83-A Suppl 1**, S105, 2001.

192. Hulbert, S.F., Young, F.A., Mathews, R.S., Klawitter, J.J., Talbert, C.D., and Stelling, F.H. Potential of ceramic materials as permanently implantable skeletal prostheses. Journal of Biomedical Materials Research **4**, 433, 1970.

193. Fisher, J.P., Vehof, J.W.M., Dean, D., van der Waerden, J.P.C.M., Holland, T.A., Mikos, A.G., and Jansen, J.A. Soft and hard tissue response to photocrosslinked poly(propylene fumarate) scaffolds in a rabbit model. Journal of Biomedical Materials Research **59**, 547, 2002.

194. Kujala, S., Ryhänen, J., Danilov, A., and Tuukkanen, J. Effect of porosity on the osteointegration and bone ingrowth of a weight-bearing nickel–titanium bone graft substitute. Biomaterials **24**, 4691, 2003.

195. Kruyt, M.C., de Bruijn, J.D., Wilson, C.E., Oner, F.C., van Blitterswijk, C.A., Verbout, A.J., and Dhert, W.J.A. Viable Osteogenic Cells Are Obligatory for Tissue-Engineered Ectopic Bone Formation in Goats. Tissue Engineering **9**, 327, 2003.

196. Itoh, M., Shimazu, A., Hirata, I., Yoshida, Y., Shintani, H., and Okazaki, M. Characterization of CO3Ap-collagen sponges using X-ray high-resolution microtomography. Biomaterials **25**, 2577, 2004.

197. Marshall, A.J., and Ratner, B.D. Quantitative characterization of sphere-templated porous biomaterials. AIChE Journal **51**, 1221, 2005.

198. Malachanne, E., Dureisseix, D., Cañadas, P., and Jourdan, F. Experimental and numerical identification of cortical bone permeability. Journal of Biomechanics **41**, 721, 2008.

199. Baroud, G., Falk, R., Crookshank, M., Sponagel, S., and Steffen, T. Experimental and theoretical investigation of directional permeability of human vertebral cancellous bone for cement infiltration. Journal of Biomechanics **37**, 189, 2004.

200. Dias, M., Fernandes, P., Guedes, J., and Hollister, S. Permeability analysis of scaffolds for bone tissue engineering. Journal of biomechanics **45**, 938, 2012.

201. Menner, A., Powell, R., and Bismarck, A. A new route to carbon black filled polyHIPEs. Soft Matter **2**, 337, 2006.

202. Wu, R., Menner, A., and Bismarck, A. Tough Interconnected Polymerized Medium and High Internal Phase Emulsions Reinforced by Silica Particles. Journal of Polymer Science Part A: Polymer Chemistry **48**, 1979, 2010.

203. Kolambkar, Y.M., Dupont, K.M., Boerckel, J.D., Huebsch, N., Mooney, D.J., Hutmacher, D.W., and Guldberg, R.E. An alginate-based hybrid system for growth factor delivery in the functional repair of large bone defects. Biomaterials **32**, 65, 2011.

204. Lee, S., Porter, M., Wasko, S., Lau, G., Chen, P.-Y., Novitskaya, E.E., Tomsia, A.P., Almutairi, A., Meyers, M.A., and McKittrick, J. Potential Bone Replacement Materials Prepared by Two Methods. MRS Proceedings **1418**2012.

205. Lam, C.X.F., Hutmacher, D.W., Schantz, J.-T., Woodruff, M.A., and Teoh, S.H. Evaluation of polycaprolactone scaffold degradation for 6 months in vitro and in vivo. Journal of Biomedical Materials Research Part A **90A**, 906, 2009.

206. Hinton, T.J., Jallerat, Q., Palchesko, R.N., Park, J.H., Grodzicki, M.S., Shue, H.-J., Ramadan, M.H., Hudson, A.R., and Feinberg, A.W. Three-dimensional printing of complex biological structures by freeform reversible embedding of suspended hydrogels. Science Advances **1**2015.

110

207. Hoffman, A.S. Hydrogels for biomedical applications. Advanced Drug Delivery Reviews **43**, 3, 2002.

208. Hockaday, L.A., Kang, K.H., Colangelo, N.W., Cheung, P.Y., Duan, B., Malone, E., Wu, J., Girardi, L.N., Bonassar, L.J., Lipson, H., Chu, C.C., and Butcher, J.T. Rapid 3D printing of anatomically accurate and mechanically heterogeneous aortic valve hydrogel scaffolds. Biofabrication **4**, 035005, 2012.

209. Billiet, T., Vandenhaute, M., Schelfhout, J., Van Vlierberghe, S., and Dubruel, P. A review of trends and limitations in hydrogel-rapid prototyping for tissue engineering. Biomaterials **33**, 6020, 2012.

210. Malda, J., Visser, J., Melchels, F.P., Jungst, T., Hennink, W.E., Dhert, W.J., Groll, J., and Hutmacher, D.W. 25th anniversary article: Engineering hydrogels for biofabrication. Advanced materials (Deerfield Beach, Fla) **25**, 5011, 2013.

211. Jungst, T., Smolan, W., Schacht, K., Scheibel, T., and Groll, J. Strategies and Molecular Design Criteria for 3D Printable Hydrogels. Chemical Reviews **116**, 1496, 2016.

212. Eiselt, P., Yeh, J., Latvala, R.K., Shea, L.D., and Mooney, D.J. Porous carriers for biomedical applications based on alginate hydrogels. Biomaterials **21**, 1921, 2000.

213. Schütz, K., Placht, A.-M., Paul, B., Brüggemeier, S., Gelinsky, M., and Lode, A. Three-dimensional plotting of a cell-laden alginate/methylcellulose blend: towards biofabrication of tissue engineering constructs with clinically relevant dimensions. Journal of Tissue Engineering and Regenerative Medicine, n/a, 2015.

214. Xavier, J.R., Thakur, T., Desai, P., Jaiswal, M.K., Sears, N., Cosgriff-Hernandez, E., Kaunas, R., and Gaharwar, A.K. Bioactive Nanoengineered Hydrogels for Bone Tissue Engineering: A Growth-Factor-Free Approach. ACS Nano **9**, 3109, 2015.

215. Majima, T., Schnabel, W., and Weber, W. Phenyl-2,4,6-trimethylbenzoylphosphinates as water-soluble photoinitiators. Generation and reactivity of O□Ṗ(C6H5)(O−) radical anions. Die Makromolekulare Chemie **192**, 2307, 1991.

216. Hahn, M.S., Taite, L.J., Moon, J.J., Rowland, M.C., Ruffino, K.A., and West, J.L. Photolithographic patterning of polyethylene glycol hydrogels. Biomaterials **27**, 2519, 2006.

217. Gombotz, W.R., Guanghui, W., Horbett, T.A., and Hoffman, A.S. Protein adsorption to poly(ethylene oxide) surfaces. Journal of Biomedical Materials Research **25**, 1547, 1991.

218. Deible, C.R., Petrosko, P., Johnson, P.C., Beckman, E.J., Russell, A.J., and Wagner, W.R. Molecular barriers to biomaterial thrombosis by modification of surface proteins with polyethylene glycol. Biomaterials **19**, 1885, 1998.

219. Bryant, S.J., and Anseth, K.S. Controlling the spatial distribution of ECM components in degradable PEG hydrogels for tissue engineering cartilage. Journal of Biomedical Materials Research Part A **64A**, 70, 2003.

220. Burdick, J.A., and Anseth, K.S. Photoencapsulation of osteoblasts in injectable RGD-modified PEG hydrogels for bone tissue engineering. Biomaterials **23**, 4315, 2002.

221. Lee, K.Y., and Mooney, D.J. Hydrogels for Tissue Engineering. Chemical Reviews **101**, 1869, 2001.

222. Nguyen, K.T., and West, J.L. Photopolymerizable hydrogels for tissue engineering applications. Biomaterials **23**, 4307, 2002.

223. Anseth, K.S., Bowman, C.N., and Brannon-Peppas, L. Mechanical properties of hydrogels and their experimental determination. Biomaterials **17**, 1647, 1996.

224. Browning, M.B., Wilems, T., Hahn, M., and Cosgriff-Hernandez, E. Compositional control of poly(ethylene glycol) hydrogel modulus independent of mesh size. Journal of Biomedical Materials Research Part A **98A**, 268, 2011.

225. Lin, C.-C., and Anseth, K.S. PEG Hydrogels for the Controlled Release of Biomolecules in Regenerative Medicine. Pharmaceutical Research **26**, 631, 2009.

226. Mann, B.K., Schmedlen, R.H., and West, J.L. Tethered-TGF-β increases extracellular matrix production of vascular smooth muscle cells. Biomaterials **22**, 439, 2001.

227. Nuttelman, C.R., Rice, M.A., Rydholm, A.E., Salinas, C.N., Shah, D.N., and Anseth, K.S. Macromolecular monomers for the synthesis of hydrogel niches and their application in cell encapsulation and tissue engineering. Progress in Polymer Science **33**, 167, 2008.

228. Kim, S.W., Bae, Y.H., and Okano, T. Hydrogels: Swelling, drug loading, and release. Pharmaceutical Research **9**, 283, 1992.

229. Panwar, A., and Tan, L. Current Status of Bioinks for Micro-Extrusion-Based 3D Bioprinting. Molecules **21**, 685, 2016.

230. Novotna, K., Havelka, P., Sopuch, T., Kolarova, K., Vosmanska, V., Lisa, V., Svorcik, V., and Bacakova, L. Cellulose-based materials as scaffolds for tissue engineering. Cellulose **20**, 2263, 2013.

231. Baier Leach, J., Bivens, K.A., Patrick Jr, C.W., and Schmidt, C.E. Photocrosslinked hyaluronic acid hydrogels: Natural, biodegradable tissue engineering scaffolds. Biotechnology and Bioengineering **82**, 578, 2003.

232. Karageorgiou, V., and Kaplan, D. Porosity of 3D biomaterial scaffolds and osteogenesis. Biomaterials **26**, 5474, 2005.

233. Sušec, M., Liska, R., Russmüller, G., Kotek, J., and Krajnc, P. Microcellular Open Porous Monoliths for Cell Growth by Thiol-Ene Polymerization of Low-Toxicity Monomers in High Internal Phase Emulsions. Macromolecular Bioscience **15**, 253, 2015.

234. Zhu, Y., Hua, Y., Zhang, S.M., Chen, J.D., and Hu, C.P. Vinyl ester oligomer crosslinked porous polymers prepared via surfactant-free high internal phase emulsions. Journal of Nanomaterials 2012.

235. Kimmins, S.D., Wyman, P., and Cameron, N.R. Amine-functionalization of glycidyl methacrylate-containing emulsion-templated porous polymers and immobilization of proteinase K for biocatalysis. Polymer **55**, 416, 2014.

236. Bakarich, S.E., Panhuis, M.i.h., Beirne, S., Wallace, G.G., and Spinks, G.M. Extrusion printing of ionic-covalent entanglement hydrogels with high toughness. Journal of Materials Chemistry B **1**, 4939, 2013.

237. Bigi, A., Cojazzi, G., Panzavolta, S., Roveri, N., and Rubini, K. Stabilization of gelatin films by crosslinking with genipin. Biomaterials **23**, 4827, 2002.

238. Farris, S., Song, J., and Huang, Q. Alternative reaction mechanism for the cross-linking of gelatin with glutaraldehyde. Journal of Agricultural and Food Chemistry **58**, 998, 2010.